

**PHASE CHANGE AND ABLATION STUDY OF METALS BY
FEMTOSECOND LASER IRRADIATION USING HYBRID
TTM/MD SIMULATIONS**

by

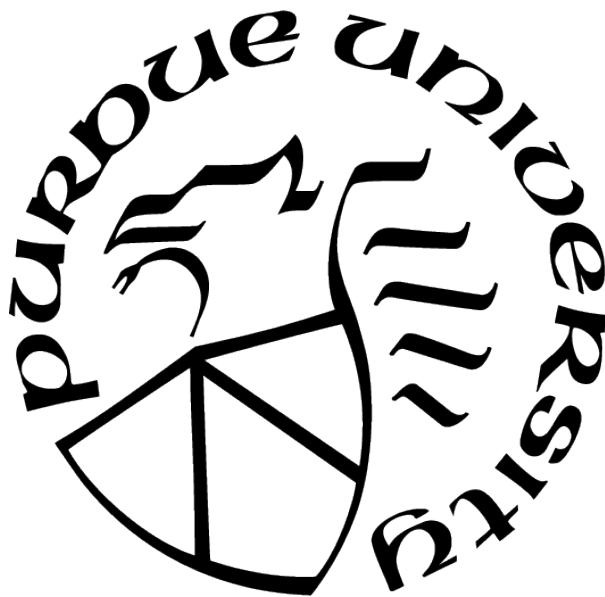
Weirong Yuan

A Dissertation

Submitted to the Faculty of Purdue University

In Partial Fulfillment of the Requirements for the degree of

Doctor of Philosophy



School of Nuclear Engineering

West Lafayette, Indiana

May 2021

**THE PURDUE UNIVERSITY GRADUATE SCHOOL
STATEMENT OF COMMITTEE APPROVAL**

Dr. Tatyana Sizyuk, Chair

School of Nuclear Engineering

Dr. Janelle Wharry

School of Materials Engineering

Dr. Zinetula Insepov

School of Nuclear Engineering, Professor and Founding Faculty Fellow of Skolkovo/MIT
Initiative

Dr. Allen Garner

School of Nuclear Engineering

Dr. Valeryi Sizyuk

School of Nuclear Engineering

Approved by:

Dr. Seungjin Kim

I would like to dedicate this Dissertation to the LORD, my Savior. This work is also dedicated to all aspiring students and future researchers.

ACKNOWLEDGMENTS

I would like to express my greatest gratitude to my advisor, Dr. Tatyana Sizyuk for providing an opportunity to work with our diverse group of graduate students and scientists at Center for Materials Under eXtreme Environments (CMUXE) and guiding me in doing scientific research. Her mentorship, not limited to academic advice and words of encouragement, throughout my PhD has been invaluable to me.

I would further extend my appreciation to the Committee members, Dr. Janelle Wharry, Dr. Zinetula Z. Insepov, Dr. Allen Garner, and Dr. Valeryi Sizyuk for helpful comments and advice. I also thank Dr. Ahmed Hassanein, Dr. Atsushi Sunahara, and Dr. Gennady Miloshevsky for their valuable feedback and advice on my research. I would like to thank Dr. Anastassiya Suslova for helping me in the early work. I also would like to give special thanks to Dr. Tatyana Sizyuk and Dr. Allen Garner for helping me editing the defense presentation slides and this dissertation.

Lastly, I would like to acknowledge the College of Engineering for bestowing the Ross Fellowship for supporting my first year of PhD and Dr. Tatyana Sizyuk for funding my PhD research in the second through the sixth year.

TABLE OF CONTENTS

LIST OF TABLES	9
LIST OF FIGURES	10
LIST OF SYMBOLS	14
ABSTRACT	16
1 INTRODUCTION	18
1.1 Femtosecond lasers	18
1.2 Gold advantages	20
1.3 Two temperature model and molecular dynamics	20
1.4 Four ablation features in experiments	21
1.5 Previous simulation works	22
1.6 Motivation	23
1.7 Scope of dissertation	23
2 MATHEMATICAL MODEL	25
2.1 Atomistic-continuum MD-TTM model	25
2.2 Pressure-transmitting boundary condition	27
2.3 Langevin thermostat	29
2.4 Electron blast force	29
2.5 Flux-limited diffusion model	31
2.6 Other effects	31
2.7 Femto3D	32
3 COLLISION THEORY	33
3.1 Previous works	33
3.2 Average/free charge	33
3.2.1 Fermi distribution	33
3.2.2 HULLAC and NLTE	34

3.2.3	Interpolation method	34
3.2.4	Total average charge	34
3.3	Electron participation factor	35
3.4	Collision frequencies	37
3.4.1	Electron-atom collision frequency	37
3.4.2	Electron-electron collision frequency	40
3.4.3	Electron effective collision frequency	41
4	IMPORTANT PARAMETERS	44
4.1	Introduction	44
4.2	Electron heat capacity	44
4.3	Lattice heat capacity	46
4.4	Electron thermal conductivity	48
4.5	Lattice thermal conductivity	52
4.6	Electron-phonon coupling factor	53
4.7	Effects of electron thermal conductivity and electron-phonon coupling factor	56
4.8	Adjustments	56
4.9	Optical parameters	57
4.10	Interatomic potential	58
5	ANALYSIS	59
5.1	Temperature	59
5.2	Density and Voronoi tessellation	59
5.3	Pressure	59
5.4	Entropy	60
5.5	Melting depth	60
5.6	Ablation depth	61
5.7	Nanocluster production	62
6	PHASE CHANGE STUDY	65
6.1	Introduction	65

6.2	Simulation setup	65
6.3	Surface movement benchmarking	66
6.4	Phase change simple study	66
6.5	The effects of target thickness on temperature and phase change	68
6.6	The effects of the electron blast force	75
6.7	Summary	81
7	SINGLE PULSE ABLATION STUDY	84
7.1	Introduction	84
7.2	Simulation setup	84
7.3	Melting study with ETD interatomic potential	85
7.4	Energy conservation with the 5T potential	86
7.5	Comparison of the 5T and the 1T potentials	87
7.6	Ablation mechanisms	88
7.7	Summary	92
8	DUAL PULSE ABLATION STUDY	95
8.1	Introduction	95
8.2	Simulation setup	95
8.3	Low overall absorbed fluence	96
8.4	High overall absorbed fluence	98
8.5	Summary	99
9	SUMMARY AND FUTURE WORK	102
9.1	Summary	102
9.2	Future work	103
	REFERENCES	105
A	PHYSICS	116
A.1	Theory of electromagnetic wave-material interaction	116
A.2	Drude Model for relative permittivity	118

B	CODES	120
B.1	Femto3D LAMMPS function	120
B.2	Preheating LAMMPS codes	120
B.3	Running LAMMPS codes	120
B.4	Analysis codes	120

LIST OF TABLES

4.1	Different approaches to calculate the electron heat capacity (C_e), electron thermal conductivity (K_e), and electron-phonon coupling factor (G)	56
-----	--	----

LIST OF FIGURES

1.1	Three stages of interactions between femtosecond laser and metallic materials [16]	19
2.1	Schematic representation of the atomistic-continuum model. The upper part shows the electron subsystem, and the lower part is the lattice subsystem. MD is molecular dynamics and TTM is the two-temperature model.	26
2.2	Stress colormaps for gold at laser absorbed fluence of 50 mJ/cm ² . Left graph shows the results without the use of the boundary constant f_b (or $f_b = 1$); right graph shows the results when $f_b = 0.4$	28
3.1	The average charge of gold from combining and interpolating Lin's data and HULLAC calculation. The results from ABINIT code is from Fourment's work [62]	35
3.2	Chemical potential of gold for electron temperatures up to 100 eV.	36
3.3	Participation factor of gold for electron temperatures up to 100 eV.	37
3.4	Lattice transition weight changes with lattice temperature. The dotted red line indicates the transition temperature.	40
3.5	Electron-ion collision frequency and electron-atom collision frequency when the lattice is at room temperature for electron temperatures up to 100 eV for gold. .	41
3.6	Electron-electron collision frequency of gold for electron temperatures up to 100 eV.	42
3.7	Electron effective collision frequencies of gold at 300 K and 880 K lattice temperature. The scatter points are results deduced from experimental data [62] . .	43
4.1	Phase diagram for warm dense matter. Figure is adopted from Los Alamos National Lab dense plasma theory website [67].	45
4.2	Electron heat capacity of gold calculated by three different methods.	47
4.3	Electron thermal conductivity of gold calculated by smooth interpolation method at different lattice temperatures.	49
4.4	Electron thermal conductivity of gold calculated by modified interpolation method at different lattice temperatures.	50
4.5	Electron thermal conductivity of gold calculated by equation 4.11 from Anisimov and Rethfeld [24] at different lattice temperatures.	51
4.6	Electron thermal conductivity of solid gold calculated by expression from Petrov <i>et al.</i> [23] at different lattice temperatures. The material density is 19.3 g/cm ³	53
4.7	Electron thermal conductivity of liquid gold calculated by expression from Petrov <i>et al.</i> [23] at different lattice temperatures. The material density is 17.0 g/cm ³	54
4.8	Electron-phonon coupling factor of gold by Lin <i>et al.</i> [22] and Ashitkov <i>et al.</i> [25].	55

4.9	Lattice temperature profiles at 1 ps (left) and 10 ps (right) for different values of electron thermal conductivity and electron-phonon coupling factor.	57
5.1	Entropy gradients in laser incident direction of gold at 10 ps, 30 ps and 50 ps. .	61
5.2	Phase change locations (S-L interfaces) predicted by entropy gradients at 10 ps (top), 30 ps (middle) and 50 ps (bottom), corresponding to Figure 5.1. The left and right latches correspond to the location of 40 nm and 80 nm in the target, and the middle latch shows the location of corresponding entropy gradient peak.	62
5.3	Number of clusters with different sizes at times of 10 ps, 20 ps, 30 ps, 40 ps, and 50 ps.	64
5.4	Spatial distribution of nanocluster with size 1 (left) and size 2 (right). Position 0 nm means the initial location of the target surface.	64
6.1	Displacement of gold surface obtained in the simulation for absorbed fluence 100 mJ/cm ² and experimental data [25] with laser fluences 1.56 and 1.30 J/cm ² . . .	67
6.2	Solid-liquid interface position (left) and melted thickness (right) profiles for 500 nm gold target with absorbed laser fluence 100 mJ/cm ² . Melted thickness is calculated from number of atoms in the melted layer with lattice density correspondent to room temperature.	68
6.3	Lattice temperatures at 100 ps, 200 ps and 300 ps with absorbed fluence 100 mJ/cm ² . The peaks in the middle indicate the solid-liquid interface.	69
6.4	Electron temperatures at 10 ps after laser irradiation for two different absorbed laser fluences (100 mJ/cm ² and 150 mJ/cm ²) and three different target thicknesses (200 nm, 500 nm, bulk)	70
6.5	Lattice temperatures at 10 ps after laser irradiation for two different absorbed laser fluences (100 mJ/cm ² and 150 mJ/cm ²) and three different target thicknesses (200 nm, 500 nm, bulk)	71
6.6	Lattice temperatures at 300 ps after laser irradiation for two different absorbed laser fluences (100 mJ/cm ² and 150 mJ/cm ²) and three different target thicknesses (200 nm, 500 nm, bulk)	72
6.7	Melted thicknesses during the first 300 ps after laser irradiation for two different absorbed laser fluences (100 mJ/cm ² and 150 mJ/cm ²) and two different target thicknesses (500 nm, bulk)	73
6.8	Melted thicknesses of gold bulk material for absorbed fluences from 100 mJ/cm ² to 200 mJ/cm ²	74
6.9	Melting profile for 200 nm gold during the first 80 ps with absorbed fluence 100 mJ/cm ²	76
6.10	Lattice temperatures at 80 ps with 100 mJ/cm ² absorbed laser fluence for three different target thicknesses (200 nm, 500 nm, bulk).	77

6.11	Surface movement profiles of gold during the first 300 ps after laser irradiation for two different absorbed laser fluences (100 mJ/cm ² and 150 mJ/cm ²) and two different target thicknesses (500 nm and bulk)	78
6.12	Surface movement profiles of 200 nm gold during the first 300 ps after laser irradiation for two different absorbed laser fluences (100 mJ/cm ² and 150 mJ/cm ²).	79
6.13	Lattice temperatures of 200 nm gold thin film at 200 ps and 300 ps after laser irradiation for two different absorbed laser fluences (100 mJ/cm ² and 150 mJ/cm ²).	80
6.14	Snapshots of the surfaces of 500 nm gold film at 40 ps (top) and 70 ps (bottom). The red regions indicate the 30 nm surface layers. Note that these snapshots are taken at different locations in the simulation box.	81
6.15	Snapshots of the ablated atoms in the cases of 200 nm (top), 500 nm (middle) and bulk (bottom) at their own ablation thresholds (170 mJ/cm ² , 160 mJ/cm ² , and 160 mJ/cm ² , respectively) at 70 ps. Note that these snapshots are taken at different locations in the simulation box.	82
6.16	Electron temperatures on the surface at 1 ps in the cases of 200 nm, 500 nm and bulk at their own ablation thresholds (170 mJ/cm ² , 160 mJ/cm ² , and 160 mJ/cm ² respectively). The profiles of 500 nm and bulk overlap in the graph.	83
7.1	Melting thicknesses and maximum electron temperature for different absorbed fluences in gold: (*) is the data from Starikov and Pisarev's results [57]. The 1T potential was used in these simulations. The lines are drawn to guide the eye.	86
7.2	Colormaps of target normalized density in gold at the absorbed fluence 45 mJ/cm ² . Left – the 5T potential; right – the 1T potential.	87
7.3	Colormaps of target surface properties within 20 ps after 45 mJ/cm ² laser irradiation with the 5T potential (Left) and the 1T potential (Right). These properties are lattice temperature (a), compressive stress (b), and tensile stress (c). The black dashed lines in (b) indicate the electron temperature in eV.	89
7.4	Ablation depth for different absorbed fluences in gold: (*) is the data measured by Hermann et al. [29] with absorptance from work by Vorobyev and Guo [28]. The circled point indicates the transition of the two ablation regimes. The lines are drawn to guide the eye.	91
7.5	Colormaps of target density in gold at absorbed fluences from 40 mJ/cm ² to 150 mJ/cm ² with the 5T potential. The black lines indicate the solid-liquid interface.	92
7.6	Colormaps of target tensile stress in gold within 20 ps after laser irradiation at absorbed fluences from 40 mJ/cm ² to 150 mJ/cm ² with the 5T potential.	93
8.1	Colormaps of target density in gold irradiated by two identical pulses each of absorbed fluences 25 mJ/cm ² with different delay times. The black lines indicate the solid-liquid interface.	97

8.2	Colormaps of target compressive stress in gold irradiated by two identical pulses each of absorbed fluences 25 mJ/cm^2 with different delay times. The black dashed lines indicate the electron temperature in eV.	97
8.3	Colormaps of target lattice temperature in gold irradiated by two identical pulses each of absorbed fluences 25 mJ/cm^2 with different delay times. The black lines indicate the solid-liquid interface.	98
8.4	Colormaps of target tensile stress in gold irradiated by two identical pulses each of absorbed fluences 25 mJ/cm^2 with different delay times. The black lines indicate the solid-liquid interface.	99
8.5	Colormaps of target density in gold irradiated by double identical pulses each of absorbed fluences 50 mJ/cm^2 with different delay times. The black lines indicate the solid-liquid interface.	100
8.6	Colormaps of target lattice temperature in gold irradiated by two identical pulses each of absorbed fluences 50 mJ/cm^2 with different delay times.	101

LIST OF SYMBOLS

C_e	electron heat capacity
T_e	electron temperature
C_l	lattice heat capacity
T_l	lattice temperature
K_e	electron thermal conductivity
K_l	lattice thermal conductivity
G	electron-phonon coupling factor
m	mass
\vec{v}	velocity
P_e	electron pressure
n_i	lattice number density
U	interatomic potential
k_b	Boltzmann constant
c_s	speed of sound
q_{fs}	free-stream flux
T_F	Fermi temperature
E_F	Fermi energy
Z	average/free charge
\hbar	reduced Planck constant
μ	chemical potential
$D(\epsilon)$	density of state
f_p	participation factor
ν	collision frequency
b_{min}	minimum impact parameter
λ_D	Debye length
$\ln \Lambda$	Coulomb logarithm
W_l	lattice transitional weight
W_e	electron transitional weight

ϵ_r	relative permittivity
R	reflectivity
l_p	penetration depth
S_{ab}	element in stress tensor
s_S	entropy
ω_p	plasma frequency
ω	laser angular frequency
c_0	speed of light
λ	laser wavelength

ABSTRACT

The interactions of femtosecond lasers with gold targets were investigated with a numerical method combining molecular dynamics (MD) and the two-temperature model (TTM). Previous works using MD-TTM method did not consider all the thermodynamic parameters and the interatomic potential dependent of the electron temperature simultaneously. Therefore, we developed a LAMMPS function to achieve this. To accurately capture the physics behind the interactions, we also included the electron blast force from free electron pressure and the modified Fourier law with steep electron temperature gradient in our model. For bulk materials, a stress non-reflecting and heat conducting boundary is added between the atomistic and the continuum parts. The modified boundary force in our study greatly reduces the reflectivity of the atomistic-continuum boundary compared with its original form. Our model is the first to consider all these factors simultaneously and manage to predict four femtosecond laser ablation phenomena observed in the experiments.

In this dissertation, the thermodynamic parameters in the two-temperature model were extensively explored. We considered three different approaches to calculate these parameters: namely interpolation, *ab initio* calculation, and analytical expression. We found that simple interpolation between solid state and plasma state could lead to high level of inaccuracy, especially for electron thermal conductivity. Therefore, *ab initio* calculation and analytical expression were used for the calculation of the thermodynamic parameters in more advanced studies. The effects of electron thermal conductivity and electron-phonon coupling factor on electron and lattice temperatures were analyzed.

Our studies considered electron temperature dependent (ETD) and electron temperature independent (ETI) interatomic potentials. The ETI interatomic potential is easier to implement and therefore it is used in our phase change study to investigate the effects of target thickness on melting. Homogeneous melting occurred for thin films, while melting can be observed through the movement of the solid-liquid interface in thick or bulk materials. However, the ETI potential overestimated the bond strength at high temperatures. Therefore, ablation process was studied with the ETD potential. Three ablation mechanisms were found in our simulations at different laser fluences. Short nonthermal ablation was only observed

at the ablation threshold. With increasing laser fluence, spallation was then seen. In high laser fluence regime, phase explosion occurred on the surface and coexisted with spallation.

Lastly, we researched on the effects of the delay time between two femtosecond laser pulses. Various delay times did not have much influence on melting depth. In low laser fluence regime, with increasing delay time, the target went through nonthermal ablation, to spallation and to no ablation. In high laser fluence regime, longer delay time encouraged phase explosion while suppressed spallation.

1. INTRODUCTION

1.1 Femtosecond lasers

In the past three decades, since the development of ultrashort pulse lasers (USPL), many fundamental, theoretical, and experimental studies have examined the physical processes in ultrashort pulse laser and material interactions [1]–[5]. With pulse durations on the order of femtoseconds to picoseconds, ultrashort pulse lasers can deliver high pulsed power up to the hundreds of TW. Due to the short pulse duration and high pulse power of femtosecond laser, laser photon interactions with metals can be considered as the interactions only with the electrons occurring during laser irradiation because the response time of atoms is much longer than the pulse duration. Therefore, during femtosecond laser irradiation, despite the high energy fluence, the lattice will remain undamaged while the electrons will be heated to very high temperatures. As a result, the atoms will gain the energy from the electrons after the laser pulse. Without direct thermal energy transferring to the lattice during the intense laser pulse, the characteristics of femtosecond laser interactions include smooth damage feature, low thermal damage, low micro crack formation, no plume-laser interactions and small size ablated particles. These advantages make femtosecond lasers a great tool for applications at small spatial and temporal scales with related areas include femtochemistry [6], telecommunications [7], laser-induced breakdown spectroscopy [8], [9], micromachining [10], [11], and nanoparticle production [11], [12].

As mentioned above, the pulse of femtosecond laser is much shorter than that in more traditional lasers, such as nanosecond lasers. Therefore, the behavior of such interactions with metallic materials can be quite different. For a femtosecond laser, during the laser-material interactions, only electrons are excited by laser irradiation, while the lattice heating can be negligible at this time scale. Electron-lattice energy transfer, heat diffusion and other relaxation processes happen in picosecond time domain. Therefore, as shown in Figure 1.1, the laser energy absorption and redistribution in metallic materials can be described as three partially overlapping stages [13]–[15].

The first stage is during the laser pulse. In this stage, the energy of incident photons will be absorbed by electrons. This process could take place via three mechanisms, namely

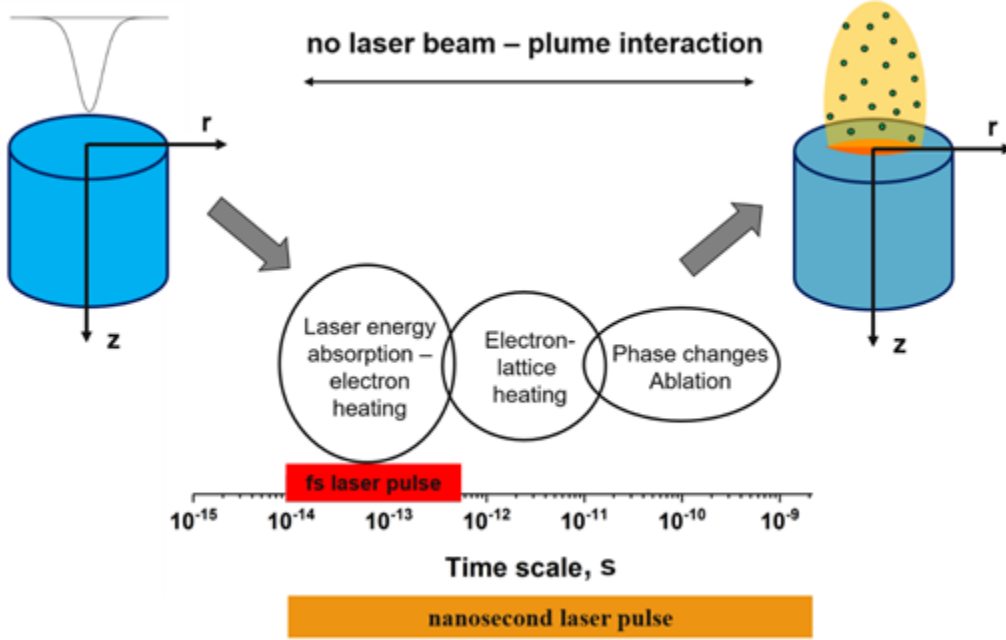


Figure 1.1. Three stages of interactions between femtosecond laser and metallic materials [16]

inverse Bremsstrahlung absorption, multiphoton absorption and collisionless absorption. For metals, inverse Bremsstrahlung absorption is the dominant absorption mechanism. In our model, this term is simplified as a Gaussian source term.

The next stage is related to the energy transfers from the electrons to the lattice and thermal conduction within atoms and electrons. In femtosecond laser-metal interactions, the relaxation time for electrons or lattice to get to local thermal equilibrium is about several femtoseconds, and the relaxation time between electrons and lattice to reach thermal equilibrium is in the order of picosecond. Therefore, it is reasonable to use temperatures to describe the status of the system in the two-temperature model.

The final stage states the macro effects due to the femtosecond laser irradiation on metallic materials. This stage includes the process of phase changes, ablation, and nanocluster or nanoparticle production. The time scale for these processes could be very different and depends on the laser parameters. Normally, they take place after tens of picoseconds.

1.2 Gold advantages

Gold nanoparticles have shown great promise for various applications among noble metals, such as nanolithography [17], catalysts [18], nanobioelectronic devices [19], and ion detection [20]. Gold films are often used as mirrors and parts of compressor gratings in the path of femtosecond laser beams. Moreover, the relaxation time of electron subsystem relaxing to lattice temperature is longer than in other metals [21], [22]. Therefore, TTM is a very suitable tool to study gold. Also, there are already thermodynamic parameters of electrons for gold calculated by many other great studies. [22]–[25]

1.3 Two temperature model and molecular dynamics

Numerous simulation methods have been developed to study the interaction between femtosecond lasers and different materials. The two-temperature model (TTM) is one of the most often used methods for the analysis of materials irradiated by relatively low laser intensities [26]. The TTM divides the whole system into two subsystems, namely electron and lattice subsystems. Each subsystem has its own temperatures, thermal conductivity, and heat capacity. The energy transfer between the two subsystems is described using the electron-phonon coupling factor G in term $\Delta E = G(T_e - T_i)$, where the electron subsystem temperature T_e should be greater than the lattice subsystem temperature T_i . The interaction time between the laser and the target is so short that the laser pulse will only heat up the electron subsystem and create non-equilibrium electron distribution, while the lattice temperature will remain almost unchanged during the laser pulse due to the large difference between the heat capacities of two subsystems ($C_i \gg C_e$). It is assumed that the equilibrium time of each subsystem should be much shorter than the equilibrium time between the two subsystems in the small space around any observing point. That is to say, the two subsystems should maintain their local equilibrium distributions much faster than the equilibrium state between the two subsystems.

However, the TTM is not capable of getting the information on the atomic level and does not allow one to consider various effects, such as stresses in material triggered by the laser. Molecular dynamics (MD), on the other hand, can handle these situations very well. MD

considers every single atom in the system. Based on the preset interatomic potential and thermodynamic ensemble, the force on each atom can be calculated. After obtaining the forces, the positions and velocities of all the atoms in the system can be updated to the next timestep. Therefore, an atomic level information can be stored for all lattice properties. However, the weakness of this method is also obvious – the simulation itself can be time consuming and impossible to run simulations for large time or space scales.

To simultaneously overcome the weaknesses and harness the advantages of these models motivates the utilization of a hybrid model combining molecular dynamics and TTM (TTM-MD). To reduce the computational cost and extend the simulation scale, this dissertation reports the development of a new method called combined atomistic-continuum model which utilizes the classical TTM and TTM-MD [27]. The combined atomistic-continuum model uses TTM-MD approach to model a few hundreds of nanometers of the target surface and classical TTM to model the thermal evolution in the bulk of material. In most current studies, parameters such as electronic thermal conductivity, heat capacity and laser reflection and penetration depth are taken as constants. To simulate and study the ultrafast effects more realistically, these parameters should be electron temperature dependent.

1.4 Four ablation features in experiments

There are four ablation features for metals observed in experiments. The first feature is small ablation depth at the ablation threshold. For gold targets, this ablation depth at the ablation threshold is lower than 20 nm. This feature was observed by Furusawa *et al.* [2]; Vorobyev and Guo [28]; and Hermann *et al.* [29]. Even though the ablation thresholds measured by their experiments differ from each other, the ablation depths at threshold were similar. According to Furusawa *et al.*, the ablation depth is 20 nm at the ablation threshold of 950 mJ/cm². While in the experiments performed by Vorobyev and Guo, the ablation depth is 10 nm at the ablation threshold of 67 mJ/cm². Hermann *et al.* showed 5 nm ablation depth at 150 mJ/cm² ablation threshold. The huge difference in the measurement of ablation threshold mainly results from the surface conditions of the target.

The second ablation feature is two ablation regimes seen in the ablation depth versus laser fluence graph for metals [2], [29]–[31]. This feature suggests that there is a change of ablation mechanisms at the interface of the two ablation regimes. We will explain in Chapter 7 that this change is due to the occurrence of spallation.

The third ablation feature is observed at the high fluence regime. At the high fluence regime, two ablation plumes can be observed due to two groups of ablated matters with different velocities and masses [12], [32].

The last feature which shows a U shape of atomization degree and a reverse U shape of ablation efficiency is observed by Hermann *et al.* [29]. The U shape or reverse U shape suggests that there are at least two changes in ablation mechanisms with increasing laser fluence from the ablation threshold. This phenomenon will be explained by three ablation mechanisms in Chapter 7.

1.5 Previous simulation works

The two-temperature model (TTM) was first proposed by Anisimov *et al.* [33] in 1974 and it was used by many studies [2], [26], [34], [35]. This model divides the irradiated target into two subsystems, namely lattice subsystem and electron subsystem. In femtosecond laser and metal interactions, the local relaxation time of lattice and electrons is much shorter than the laser pulse duration and the relaxation time between lattice and electrons. Therefore, the local thermal equilibrium allows the description of the system as two thermal subsystems. However, in ablation studies which we will show in Chapter 7, nonthermal ablation and spallation cannot be explained only by the temperature of the two subsystems. Therefore, in order to study the ablation process, we need to use other methods to include the stress effects in the materials.

Molecular dynamics (MD) considers the position and velocity of each atom in the system, so it can be used to describe the lattice subsystem to include the effects of stress and material phase. However, most of the early studies on femtosecond laser using MD did not consider the effects of electrons and the laser energy was directly deposited to the lattice. Moreover, some of the studies used simple interatomic potentials. Nedyalkov *et al.* [36] used a Morse potential

and Lewis and Perez [37] used the Stillinger-Weber (SW) potential. These potentials are incapable of accurately describing phase change and stress response in the metal targets and both of the studies underestimated the stability of metals in liquid phase.

To consider both the electronic effects and stress effects, a hybrid two-temperature and molecular dynamics (TTM-MD) model was developed [38]–[40]. In addition, the embedded atom model (EAM) was used to more accurately describe the interatomic potential in metals. Zhigilei *et al.* [41] and Wu and Zhigilei [42] found spallation and phase explosion with an electron temperature dependent electron-phonon coupling factor G . Norman *et al.* [43] used a novel electron temperature dependent (ETD) EAM interatomic potential for gold and found nonthermal/short ablation in their simulation. However, they did not observe spallation due to a small constant electron-phonon coupling factor G .

1.6 Motivation

The goal of this work is to analyze phase change and ablation process in metals irradiated by femtosecond lasers. This is important for target preconditioning for the efficient EUV sources, nanoparticles formation and precise micromachining. To achieve this goal, we developed an advanced simulation model based on TTM-MD which considers all the thermodynamic parameters and interatomic potential dependent of the electron temperature simultaneously. This model also includes the nonequilibrium effects of free electrons in the lattice subsystem and electron subsystem using the electron blast force and the flux-limited model respectively.

1.7 Scope of dissertation

In Chapter 2, details of atomistic-continuum TTM-MD model are discussed, including the equations used in the model where the pressure-transmitting boundary condition used to connect the atomistic and continuum parts. The general Langevin thermostat will also be introduced and how it is modified to fit in our model. Also, to take into account the non-equilibrium effects of free electrons on lattice, an electron blast force was introduced into the equations. Lastly, to avoid overestimating the electron thermal conduction and

limit heat flux produced by free electrons, the model of flux-limited diffusion is also implemented in our model. In Chapter 3, collision theory is introduced. The collision frequencies for electrons are calculated for both solid state and plasma state. Interpolation method is used to obtain the frequencies in the state of warm dense matter. These frequencies are later used to calculate the electron thermal conductivity and other parameters. Chapter 4 concludes various methods calculating the thermodynamic and optical parameters used in TTM. These methods include interpolation methods, *ab initio* calculations, and analytical expressions. In Chapter 5, parameters used to analyze the changes in the irradiated material are listed and described. They include temperature, pressure, melting depth, and ablation depth. Chapter 6 shows the effects of target thickness on melting. Homogeneous melting were found in thin films. In Chapter 7, ablation of gold was studied with the use of electron temperature dependent (ETD) interatomic potential and electron temperature dependent thermodynamic parameters. Three ablation mechanisms, namely nonthermal ablation, spallation, and phase explosion, are found. Our results showed all four ablation features observed in the experiments as described earlier in this chapter for the first time. Chapter 8 explores the effects of the delay time between two consequent pulses in both low and high fluence regimes. An optimal nanoparticle production condition was found. Concluding remarks are made in Chapter 9.

2. MATHEMATICAL MODEL

2.1 Atomistic-continuum MD-TTM model

In the study of ultrafast laser and metal interactions, traditional molecular dynamics (MD) neglects electron thermal conduction and electron-lattice coupling. In addition, these simulations require significant computational resources and are usually time-consuming. Although the two-temperature model (TTM) takes into account the electronic effects, it is unable to describe thermoelastic stress and lattice density on the atomic level. Therefore, a hybrid model combining these two methods is preferred. Coupling of the atomistic lattice subsystem and the continuum electron subsystem was earlier introduced in many previous works [38]–[40] and a further modified atomistic-continuum model was described by Ivanov and Zhigilei [27]. The modeling of target response to femtosecond laser irradiation can be divided into two parts – the atomistic part which describes the lattice subsystem by MD, and the continuum part which accounts for the processes in the electron subsystem based on the classical TTM.

The general equations employed for the MD-TTM model are shown as follows:

$$C_e(T_e) \frac{\partial T_e}{\partial t} = \nabla \cdot (K_e(T_e, T_l) \nabla T_e) - G(T_e)(T_e - T_l) + Q_{laser} \quad (2.1)$$

$$m_j \frac{d\vec{v}_j}{dt} = -\nabla_j U(\vec{r}_1, \dots, \vec{r}_n) + \vec{F}_j^{lang}(T_e - T_l) - \frac{\nabla P_e}{n_i} \quad (2.2)$$

In these equations, T_e and T_l are the electron and lattice temperatures, K_e and C_e are the thermal conductivity and thermal capacity of the electron subsystem, G is the electron-phonon coupling factor, Q_{laser} is the laser source term. For the atom j in MD, m_j is the mass of the atom, \vec{v}_j is its velocity. The Langevin force reflecting the energy transfer from the electronic subsystem is \vec{F}_j^{lang} and the last term on the right-hand side of equation 2.2 denotes the electron blast force where P_e is the electronic pressure by free electrons and n_i is the local lattice number density. The internal force, $-\nabla_j U$, is the force acting on atom j due to the interatomic potential U .

In simulations of bulk targets, it is practical to use TTM to describe the non-melting part of the lattice subsystem because MD is computationally costly and TTM is sufficient to describe the lattice subsystem without phase change. Therefore, in this study the lattice in the deeper part of the bulk target is described by the equation from the classical TTM:

$$C_l(T_l) \frac{\partial T_l}{\partial t} = \nabla \cdot (K_l(T_l) \nabla T_l) - G(T_e)(T_e - T_l) \quad (2.3)$$

where C_l and K_l are the lattice heat capacity and thermal conductivity. In this work, we use $C_l = 3n_i k_b$ and $K_l = 0$ since thermal conduction in lattice is much smaller than that in electrons.

Figure 2.1 shows the schematic representation of the atomistic-continuum model used in this study.

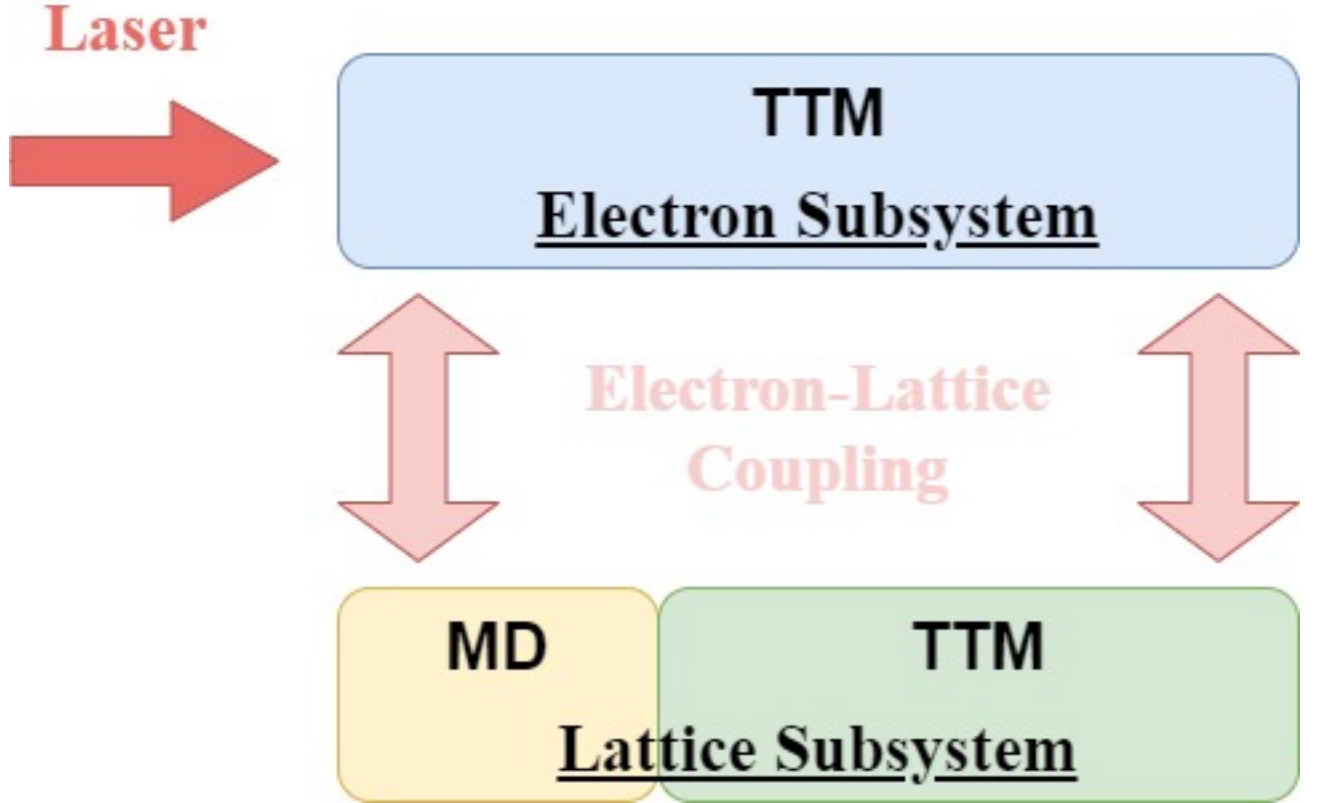


Figure 2.1. Schematic representation of the atomistic-continuum model. The upper part shows the electron subsystem, and the lower part is the lattice subsystem. MD is molecular dynamics and TTM is the two-temperature model.

2.2 Pressure-transmitting boundary condition

A non-reflecting boundary condition is applied between the MD and TTM parts in the lattice subsystem to produce more realistic stress change when thermoelastic waves approach the interface. Pressure waves will be reflected at free and fixed boundaries, which should not occur in realistic pressure transmission. Preventing this reflection requires mimicking the action of the surrounding medium on the atoms close to the boundary. Therefore, a zone at the part of the MD simulation volume adjacent to the boundary is defined with width slightly larger than cutoff radius (depending on interatomic potential). As described by Schäfer *et al.* [44], the atoms in the MD part neighboring the TTM part should experience an extra boundary force, F_{bc} , to avoid reflection. Here, we only consider the force along the laser irradiation direction which is perpendicular to the TTM-MD interface.

$$F_{bc} = F_0 - f_b \alpha u \quad (2.4)$$

$$\alpha = m_i n_i c_s A$$

In the two equations, F_0 is a static force due to atom interactions from the lower continuum part, u is the average velocity of the atoms in the boundary zone (note, artificial cooling occurs when individual velocity is used), c_s is the speed of sound in the material, and A is the impact area, which is $d^2/2$ for fcc materials and d^2 for bcc materials (d is the lattice parameter). The boundary constant f_b depends on the interatomic potential and boundary lattice temperature (0.4-0.5 for gold in our work) to further reduce the reflectivity. It is predetermined by testing many different values in simple MD simulations and choosing the one with minimum reflection of the pressure wave.

Another MD simulation was performed at room temperature (300 K) under the Nose-Hoover thermostat to calculate the lattice boundary stress. After the system equilibrated, we calculated the stress component normal to the interface of the atoms in the boundary zone. F_0 is used to cancel out the stress component from the boundary effect. The initial thickness of the boundary (6.0 Å) is slightly larger than the cutoff radius of the potential (5.6

Å). This thickness will increase dynamically with the simulation to make sure the number of the atoms in the boundary zone will not be less than its original value. Note that the boundary zone should not experience phase transition.

Figure 2.2 shows the stress profile for gold at laser absorbed fluence of 50 mJ/cm^2 before 150 ps with and without the use of the boundary constant f_b . Introducing the boundary constant f_b greatly reduces the strength of both compressive and tensile reflective waves and this allows us to perform accurate melting and ablation studies.

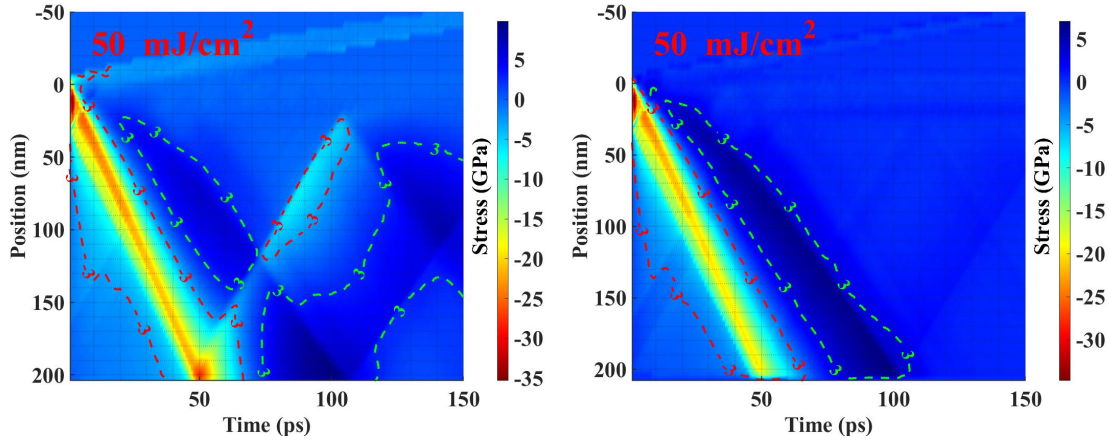


Figure 2.2. Stress colormaps for gold at laser absorbed fluence of 50 mJ/cm^2 . Left graph shows the results without the use of the boundary constant f_b (or $f_b = 1$); right graph shows the results when $f_b = 0.4$.

In this simulation, the absorbed laser fluence is 50 mJ/cm^2 , pulse duration is 100 fs, electron heat capacity (C_e) is from Lin's data [22], electron thermal conductivity (K_e) is from Anisimov and Rethfeld [24], electron-phonon coupling factor (G) is from Lin's data [22], penetration depth is 10 nm, bulk material with 200 nm in MD simulation, the 5T interatomic potential [43], [45] is used and the electron blast force vanishes at the surface.

The heat transfer at the boundary is only considered in the electron subsystem but not in the lattice subsystem because the heat conductivity of electrons is much higher than that of phonons.

2.3 Langevin thermostat

In the atomistic part, the electron subsystem is still considered as a continuum body, so for all the atoms in the MD simulation, this continuum body can be considered as a heat bath. As a result, canonical ensemble is suitable in this case. Because in our model the temperature of the electron subsystem (heat bath) is changing every timestep and the energy transfer to the lattice subsystem is predefined by the coupling factor and the temperatures of both subsystems, Langevin thermostat is well-suited for this situation. In this work, the Langevin force is used to describe electron-phonon coupling in a stochastic way, modified based on Duffy and Rutherford's works [46], [47], given by

$$\begin{aligned}
\vec{F}_{lang} &= -\gamma_g \vec{v}_T + \vec{F}_{stochastic} \\
\gamma_g &= \frac{m_i G(T_e)}{3n_i k_b} \\
\vec{F}_{stochastic} &= \sqrt{2k_b T_e \gamma_g \delta t} \vec{\beta} \\
\vec{v}_T &= \vec{v} - \vec{v}_c
\end{aligned} \tag{2.5}$$

In these equations, \vec{v} is the velocity of the atom, \vec{v}_c is the center of mass velocity in the corresponding cell, k_b is the Boltzmann constant, δt is the timestep used in MD and $\vec{\beta}$ is a vector in three dimensions whose components are independent random variables, each with an average 0 and a standard deviation 1. Even though uniform distribution can be used to describe the effects of electrons as white noise, we used Gaussian distribution in the study. The choice of different distributions has no effects on our simulation results. The first term in equation 2.5 describes the friction force on the atom due to its thermal velocity, and the second term is the white noise force from the electron heat bath.

2.4 Electron blast force

The electron drift velocity caused by the electric field and the pressure from hot electrons will exert forces on the atoms and cause lattice deformation. This force was originally

mentioned by Falkovsky and Mishchenko [48], and a modified expression is derived by Chen *et al.* [49], [50] for the nonlinearity of electron heat capacity with respect to electron temperature. Further studies [43], [51] explained that the electron blast force was caused by delocalized/free electrons.

Falkovsky and Mishchenko [48] used the Boltzmann equation for the nonequilibrium electronic partition function and dynamical theory of elasticity to study lattice deformation due to nonequilibrium electron state. They concluded that the force is proportional to ∇T_e^2 for low electron temperature.

Chen, Tzou and Beraun [50] proposed a semiclassical two-temperature model. They used three equations from the first three moments of the Boltzmann transport equation to govern the conservation of number density, momentum, and energy of the electron subsystem. A force called the hot-electron blast force coming from the nonequilibrium electrons can also be derived as $2/3\nabla C_e T_e$. This can also explain the results by Falkovsky and Mishchenko because C_e is proportional to T_e at low temperatures ($T_e < 0.1T_F$):

$$\frac{\partial P_e}{\partial k} = \gamma \frac{C_e T_e(k + \delta k) - C_e T_e(k)}{\delta k} \quad (2.6)$$

where k represents the directions x , y , or z , and γ is set to 0.667 for gold.

Starikov and Norman *et al.* mentioned that using equation 2.6 on the surface where $T_e(x) = 0$ will cause large electron pressure gradients at the surface will occur in numerical simulations. Therefore, they suggested a modified equation for the component along the laser direction to avoid this, given by

$$\frac{\partial P_e}{\partial x} = \gamma \left[\frac{C_e T_e(x) \lambda_e}{(x + \lambda_e)^2} + \frac{x}{x + \lambda_e} \frac{C_e T_e(x + \delta x) - C_e T_e(x)}{\delta x} \right] \quad (2.7)$$

where λ_e represents the effective electron mean free path and x is the laser incident direction. They also refer to the first term in equation 2.7 as the surface blast force.

From our analysis, the blast force is only responsible for the deformation inside the lattice, so the pressure should vanish at the target surface as hypothesized by Falkovsky and Chen [48], [50]. Therefore, we manually set this force to zero at the target surface when still using equation 2.6 to study the ablation process.

2.5 Flux-limited diffusion model

When dealing with steep electron temperature gradient, we will normally overestimate the electron heat flux calculated with classical Fourier's law as in equation 2.1. Malone *et al.* [52] proposed a flux-limited diffusion phenomenological model. By comparing experimental results with their model, the authors found that the energy transferred to atoms in the fast part of the distribution was much larger than expected, indicating that the electron temperature in the same part should be larger and therefore the electron thermal conductivity was overestimated. They introduced a scale called electron temperature gradient length, $L_T = |T_e/(\nabla T_e)|$, to determine whether to correct the heat transfer calculated from Fourier's law.

In this work, we assigned when $L_T \leq 10\lambda_e$ (the electron mean free path λ_e is taken as 4 nm in our study), the following correction should be applied for the electronic heat transfer:

$$q = -\frac{K_e \nabla T_e}{1 + \left| \frac{K_e \nabla T_e}{f_L q_{fs}} \right|} \quad (2.8)$$

$$q_{fs} = Zn_i T_e \sqrt{\frac{k_b T_e}{m_e}}$$

where q_{fs} is the free-stream flux indicating the maximum value of the electronic heat flux and the flux-limiter f_L is an empirical parameter which is normally set to 0.03 to 0.1.

2.6 Other effects

The ballistic electron effect is not considered because ballistic transport can be included in electron heat conduction when the collision time of the nonequilibrium electrons is comparable to the timescales of nonequilibrium electron heat transport [4], [53]. According to Suslova and Hassanein [53], in the fluence regimes we considered in the studies, the ballistic electron range decreases down to around 30 nm which is close to the prediction in our simulation results obtained by utilizing the same idea to compute the ballistic range, around 20 nm.

Our model does not consider the effects of Coulomb explosion caused by strong electric field from electron emission. According to Schmidt *et al.* [54], no Coulomb explosion should occur in metals due to effective screening by metal electrons. Bulgakova *et al.* [55] utilized a drift-diffusion approach and showed that efficient neutralization prohibits Coulomb explosion in semiconductors and metals. However, emission of electrons would remove the excess stored energy in the form of plasma [56] and it should be considered at the high fluence regime (higher than the scope of our studies).

We did not consider redeposition in our studies, which is an important factor to consider in micromachining. The main reason for redeposition of the ablated matters back on the target surface is gravity. However, our studies only considered the target response earlier than 1 ns when gravitational force is negligible compared with other forces acting on the atoms.

2.7 Femto3D

The Femto3D is a LAMMPS fix function based on the ‘Fix ttm/mod’ function [57]. An example line used in the LAMMPS input file is “fix fttm all femto3D 123456 1000 Au_parameters_test.txt Au_tablelist.txt Outlist.txt”. ‘fttm’ is the fix ID, ‘all’ means all atoms in MD is affected by this fix function, ‘femto3D’ is the Femto3D fix function name, ‘123456’ is a seed for random numbers, ‘1000’ means output temperature files every 1000 timesteps, file ‘Au_parameters_test.txt’ contains the input parameters for the fix, ‘Au_tablelist.txt’ contains the list of files for the input parameters, and ‘Outlist.txt’ contains the list of output files. More details are in Appendix B.

3. COLLISION THEORY

3.1 Previous works

This chapter extends the work done by Polek [58] and Suslova [16] and the results are further used in calculating the thermodynamic and optical parameters in the next chapter.

3.2 Average/free charge

This parameter determines the free electron density and the abilities to store and transfer energy in the electronic subsystem. Free electrons are electrons in conduction band.

3.2.1 Fermi distribution

At the temperature range below 50,000 K, Lin *et al.* performed *ab initio* electronic structure calculations by considering d band electrons in Au to obtain the electron density of state and chemical potential [22], [59] with the Vienna Ab-initio Simulation Package (VASP). We considered that the electrons follow Fermi distribution $f(\epsilon, \mu, T_e) = (e^{(\epsilon-\mu)/k_b T_e} + 1)^{-1}$ and we defined the average/free charge as the number of electrons per atom which can pass energies by colliding with other particles (electrons/atoms). The average/free charge Z calculated by summing all the electrons with energy higher than the chemical potential at given temperature is given by

$$\int_{\epsilon_l}^{\infty} \frac{D(\epsilon)}{\exp(\frac{\epsilon-\mu(T_e)}{k_b T_e}) + 1} d\epsilon = Z(T_e) \quad (3.1)$$

where ϵ_l is the lowest value of conduction band (3.54 eV for gold), \hbar is the reduced Planck constant, μ is the temperature-dependent chemical potential, and $D(\epsilon)$ is the density of state in units of states/eV/atom.

One important parameter while using Lin's data to calculate Z is the Fermi energy (E_F) which is also related to Fermi temperature $E_F = k_b T_F$, which can be calculated by the following equation:

$$E_F = \frac{\hbar^2}{2m_e} (3\pi^2 n_e)^{\frac{2}{3}} \quad (3.2)$$

Since this energy is only defined at absolute zero temperature, the electron density in conduction band (n_e) is equal to the lattice number density ($n_i = 5.90 \times 10^{28} \text{ m}^{-3}$) for gold. The calculated Fermi temperature is 64,064 K which is very close to 64,200 K from other sources [60].

However, Z calculation using Lin's data is valid only up to 50,000 K. Obtaining the average charge for a broader range of electron temperatures requires data from other sources.

3.2.2 HULLAC and NLTE

At higher temperatures (up to 100 eV), the average charge is calculated by using the HULLAC code [61]. The code is designed to calculate the atomic and optical characteristics of plasma in non-local thermodynamic equilibrium (NLTE) state and uses collisional radiative model. Therefore, these calculations are not suitable for the regimes when the material is still in solid state. Therefore, the HULLAC code was used for the range of electron temperature from 40 eV to 100 eV.

3.2.3 Interpolation method

For electron temperature between 4.3 eV (50,000 K) and 40 eV, the average/free charge was calculated using linear interpolation of the charges at those two end points.

3.2.4 Total average charge

To obtain the average charge in the whole range from room temperature to 100 eV, we combined and interpolated the results from the above two methods. The ABINIT results

by Fourment *et al.* [62] were used for benchmarking of our calculations. The comparison results are shown in Figure 3.1.

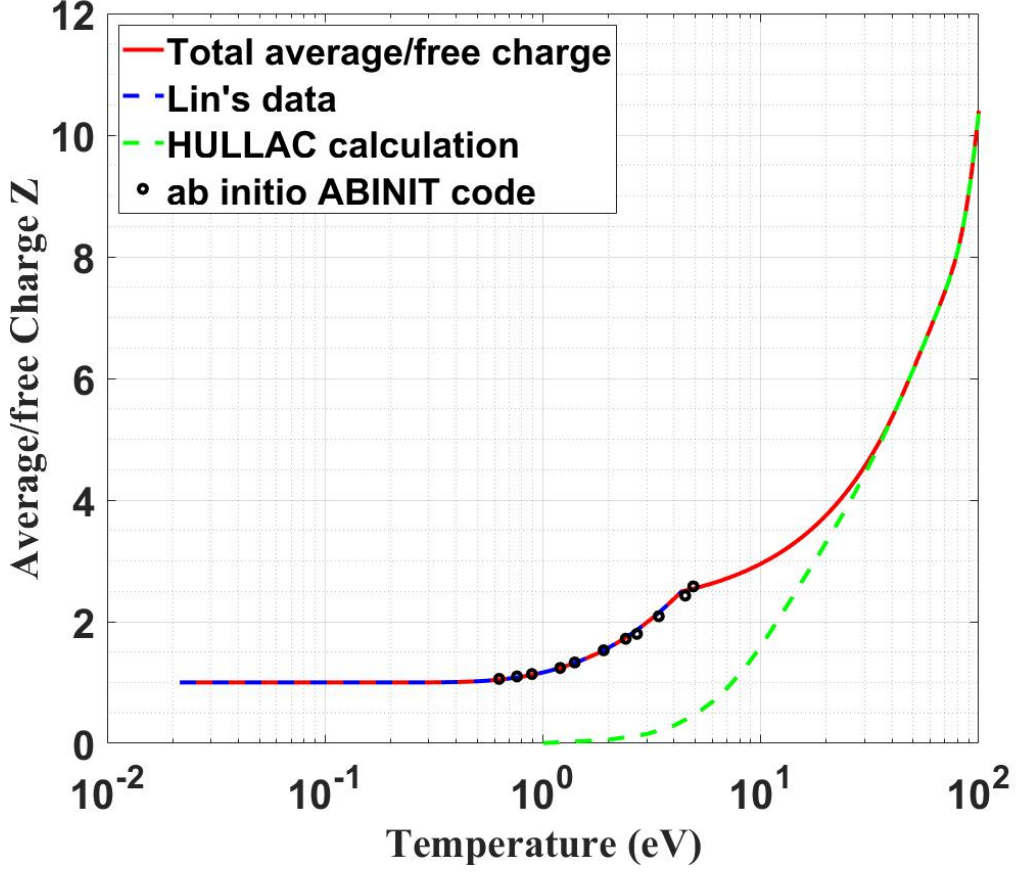


Figure 3.1. The average charge of gold from combining and interpolating Lin's data and HULLAC calculation. The results from ABINIT code is from Fourment's work [62]

3.3 Electron participation factor

To take the degeneracy effect into consideration, Polek [58] introduced the electron participation factor f_p to modify the Spitzer's formula for temperature below 40 eV, given by

$$f_p = \frac{1}{Z(T_e)} \int_{\mu(T_e)}^{\infty} \frac{D(\epsilon)}{\exp(\frac{\epsilon - \mu(T_e)}{k_b T_e}) + 1} d\epsilon \quad (3.3)$$

For electron temperatures higher than 40 eV, $f_p = 1$.

Since we only have data for the chemical potential up to 4.3 eV (50,000 K) electron temperature, we need to determine the chemical potential above 4.3 eV (50,000 K). For temperature range, we assume the free gas model for electron distribution, where the interactions between electrons are neglected.

The following equation is used to calculate the chemical potential:

$$\frac{\sqrt{2m_e^3}}{\pi^2 \hbar^3} \int_0^\infty \frac{\sqrt{\epsilon}}{\exp(\frac{\epsilon - \mu(T_e)}{k_b T_e}) + 1} d\epsilon = Z(T_e) n_i \quad (3.4)$$

Figure 3.2 shows the chemical potential, consisting of Lin's data for temperatures below 50,000 K and the calculated results by our model when temperature above 50,000 K. After around 10 eV, the calculated chemical potential is below 0, so we fix it to 0 to avoid non-physical results.

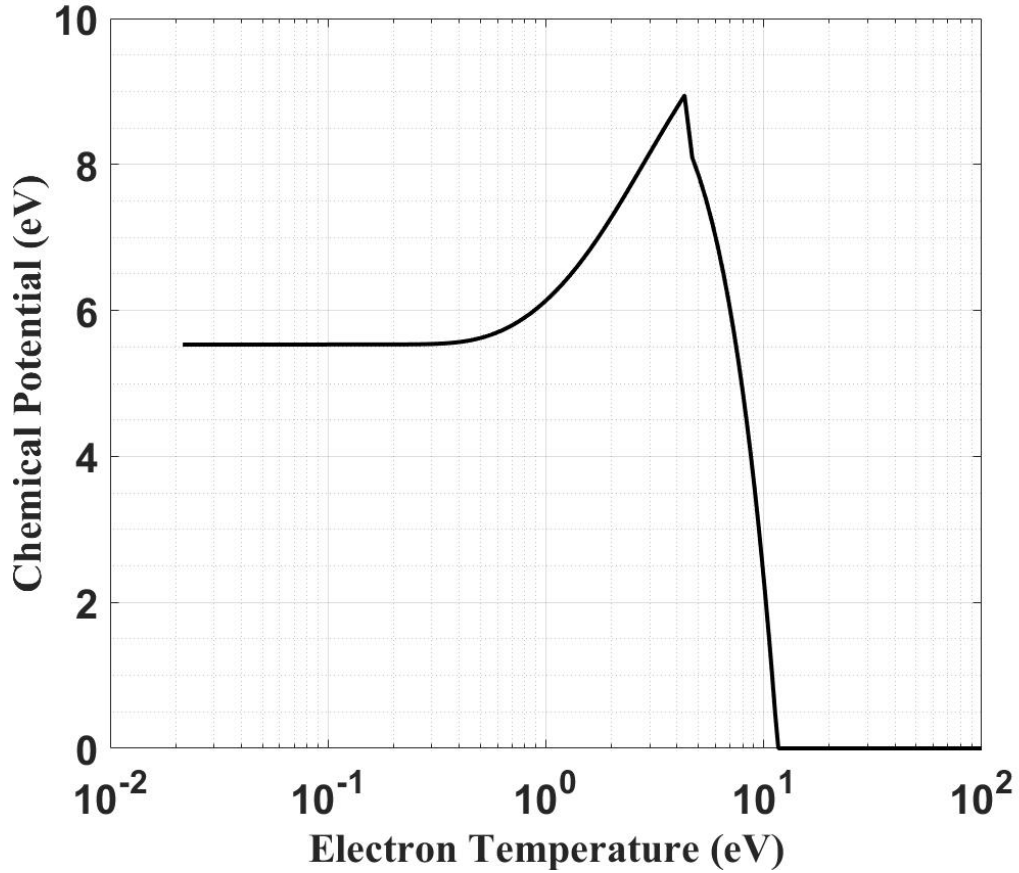


Figure 3.2. Chemical potential of gold for electron temperatures up to 100 eV.

Figure 3.3 shows the participation factor in the whole temperature range. The electron participation factor varies between 0 and 1, so we use 1 to cap any higher values.

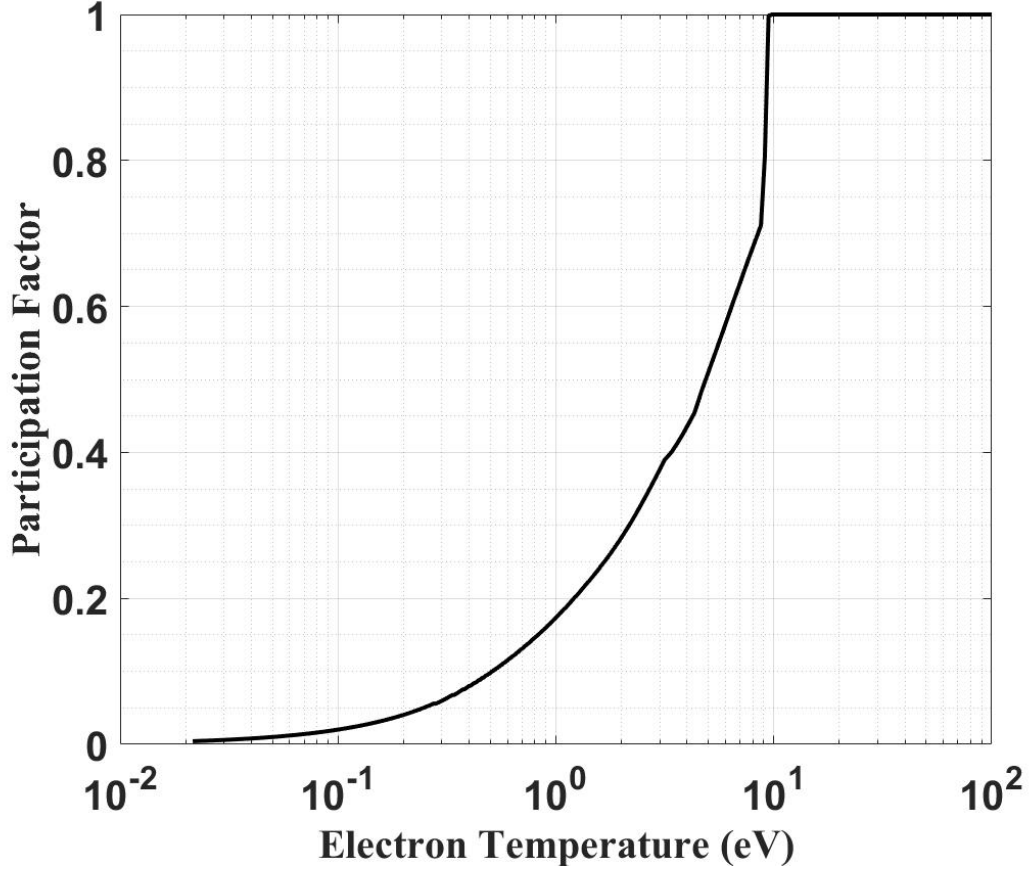


Figure 3.3. Participation factor of gold for electron temperatures up to 100 eV.

3.4 Collision frequencies

3.4.1 Electron-atom collision frequency

In cold solid state, the interactions between the two subsystems are mainly the scattering of electrons by phonons. For this type of collision mechanism, the collision frequency can be estimated by

$$\nu_{e-ph} = \nu_{e-ph}^0 \frac{T_l}{300} \quad (3.5)$$

where ν_{e-ph}^0 is the electron-phonon collision frequency at room temperature. This value is usually calculated by fitting the permittivity formula from Drude model to the experimental values. According to Rakić *et al.* [63], the permittivity for gold at room temperature is $\epsilon_1 + i\epsilon_2 = -22.104 + 1.78i$. Using Drude's dielectric function 4.19 and laser frequency ω , we can obtain

$$\nu_{e-ph}^0 = \omega * \frac{\epsilon_2}{1 - \epsilon_1} \quad (3.6)$$

In hot plasma state, the collisional interactions in the two subsystems are through long-range Coulomb forces between charged particles, ions and electrons. However, the range of this force is short due to electric-field screening caused by mobile charged particles. The maximum length of such an interaction is called Debye length, beyond which the interaction or “collision” may be neglected. Debye length can be calculated as $\lambda_D = \sqrt{\epsilon_0 k_b T_e / (Z n_i e^2)}$. However, when temperature gets higher, there are physical limits for the distance of interactions. In the view of classical physics, the minimum distance is a classical minimum impact parameter, b_{min}^{cl} . In quantum mechanics, the minimum impact parameter denotes as b_{min}^{qm} .

$$b_{min} = \max(b_{min}^{cl} = \frac{2e^2}{4\pi\epsilon_0 m_e \theta^2}, b_{min}^{qm} = \frac{\hbar}{2m_e \theta}) \quad (3.7)$$

$$\theta = \sqrt{\frac{2}{m_e} (k_b T_e + \mu(T_e))}$$

The θ in equation 3.7 is also called impacting velocity. To sum up all the interactions ranging from b_{min} to λ_D , we use a parameter called the Coulomb logarithm, $\ln \Lambda$.

$$\ln \Lambda = \int_{b_{min}}^{\lambda_D} \frac{1}{b} db = \ln \frac{\lambda_D}{b_{min}} \quad (3.8)$$

Because we need to use the formula for the Coulomb logarithm for a wide temperature range, it is possible to have conditions when the calculated b_{min} is larger than λ_D . Therefore, when this happens, we must let $\ln \Lambda = 1$ to avoid nonphysical behavior [58].

Using Spitzer's formula [64], [65] modified by the participation factor [16], [58], we can obtain the electron-ion collision frequency considering the electron degeneracy effect.

$$\nu_{e-i} = \frac{4}{3\sqrt{\pi}} \frac{Z^2 e^4 n_i}{4\pi\epsilon_0^2} \frac{f_p}{\sqrt{m_e(2k_b T_e + 2\mu(T_e))^3}} \ln \Lambda \quad (3.9)$$

Here ϵ_0 is the vacuum permittivity, e is the electron charge and $\ln \Lambda$ is the coulomb logarithm. Its higher limit is calculated based on the hard sphere model $\nu_{vs} = \sqrt{2k_b T_e/m_e + v_F^2}/r_0$, where $v_F = \sqrt{2E_F/m_e}$ is the electron Fermi velocity and r_0 is the atomic radius. Note the atomic radius r_0 for gold taken in this study is 2.14 Å according to Suslova [35], but according to Robinson *et al.* [66], this value is 1.44 Å.

To account for the transition from solid state to plasma state, we need to evaluate the lattice temperature. It is well known that in the femtosecond laser-metal interactions, overheating happens, so we define a transition temperature T_{tran} which is slightly above or equal to the boiling point of the metallic material. For gold, we choose 3000 K as T_{tran} . Using this T_{tran} , we introduce a lattice weight factor in calculating total interactions between atoms and electrons, given by

$$W_l = \frac{2}{e^{T_l/T_{tran}} + 1} \quad (3.10)$$

Figure 3.4 shows the transition weight changes with lattice temperature.

Using the lattice weight factor to combine collision frequency in solid state and warm dense matter state, the total collision frequency between atoms and electrons (electron-atom collision frequency) is calculated by

$$\nu_{e-a} = (1 - W_l) \times \nu_{e-i} + W_l \times \nu_{e-ph} \quad (3.11)$$

Figure 3.5 compares the electron-ion collision frequency and the electron-atom frequency calculated for room temperature, 300 K.

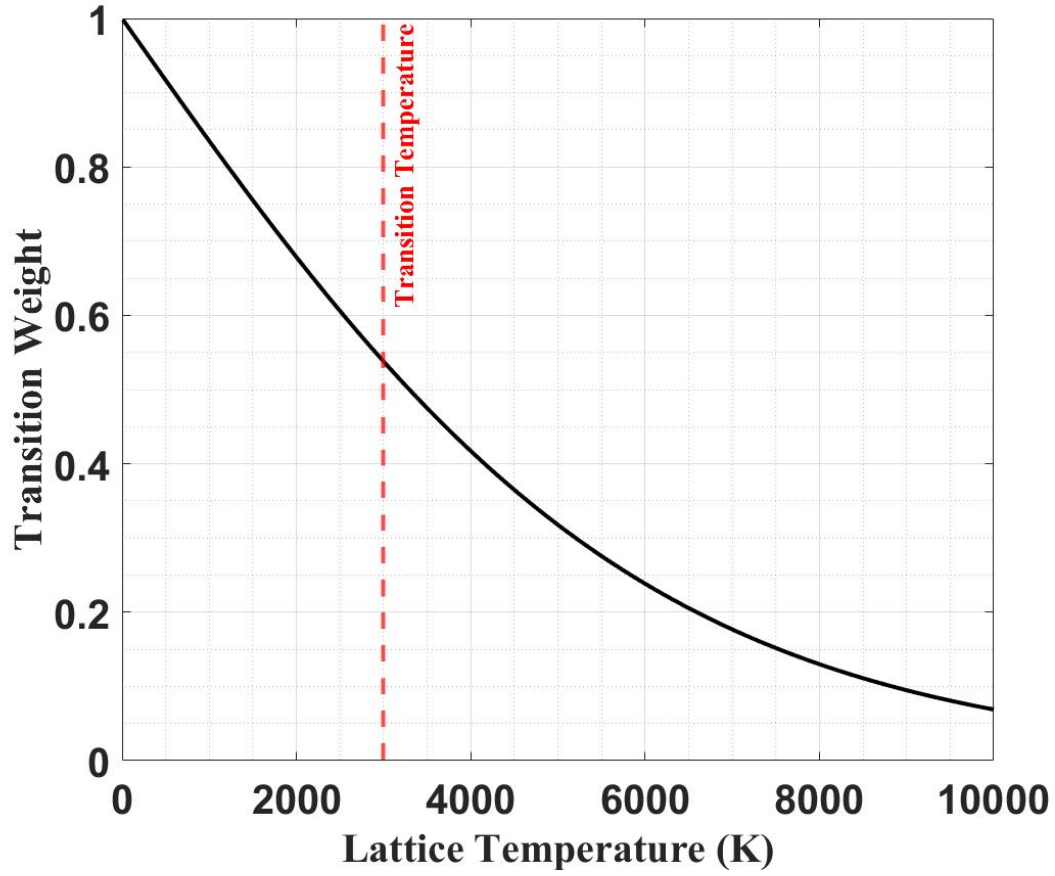


Figure 3.4. Lattice transition weight changes with lattice temperature. The dotted red line indicates the transition temperature.

3.4.2 Electron-electron collision frequency

The electron-electron collision frequency is calculated similarly as the electron-ion frequency, given by

$$\nu_{e-e} = \frac{4}{3\sqrt{\pi}} \frac{Ze^4 n_i}{4\pi\epsilon_0^2} \frac{f_p^2}{\sqrt{m_e(2k_b T_e + 2\mu(T_e))^3}} \ln \Lambda \quad (3.12)$$

Introducing the participation factor makes this frequency much lower than the electron-phonon collision frequency. Therefore, equation 3.12 can also be used in the low electron temperature regime.

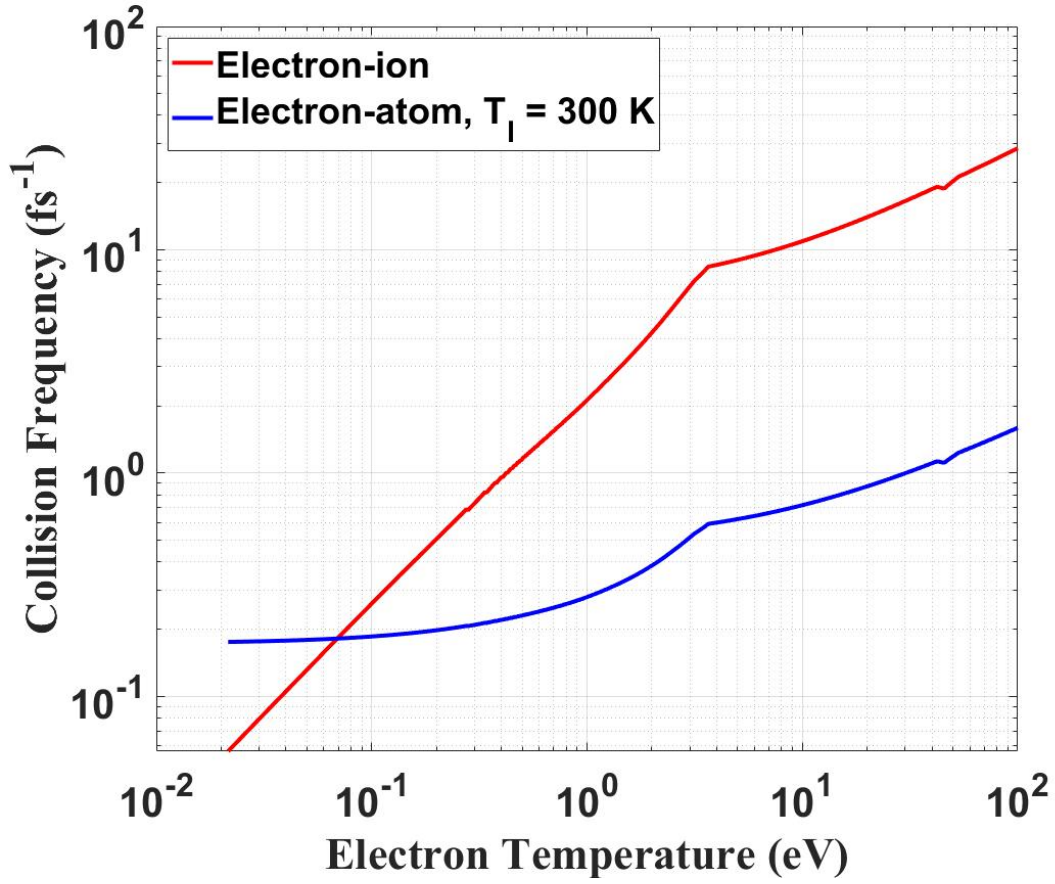


Figure 3.5. Electron-ion collision frequency and electron-atom collision frequency when the lattice is at room temperature for electron temperatures up to 100 eV for gold.

Figure 3.6 shows the electron-electron collision frequency of gold for electron temperatures up to 100 eV.

3.4.3 Electron effective collision frequency

The overall electron effective collision frequency is the combination of electron-atom frequency and electron-electron collision frequency, giving

$$\nu_{eff} = \nu_{e-a} + \nu_{e-e} \quad (3.13)$$

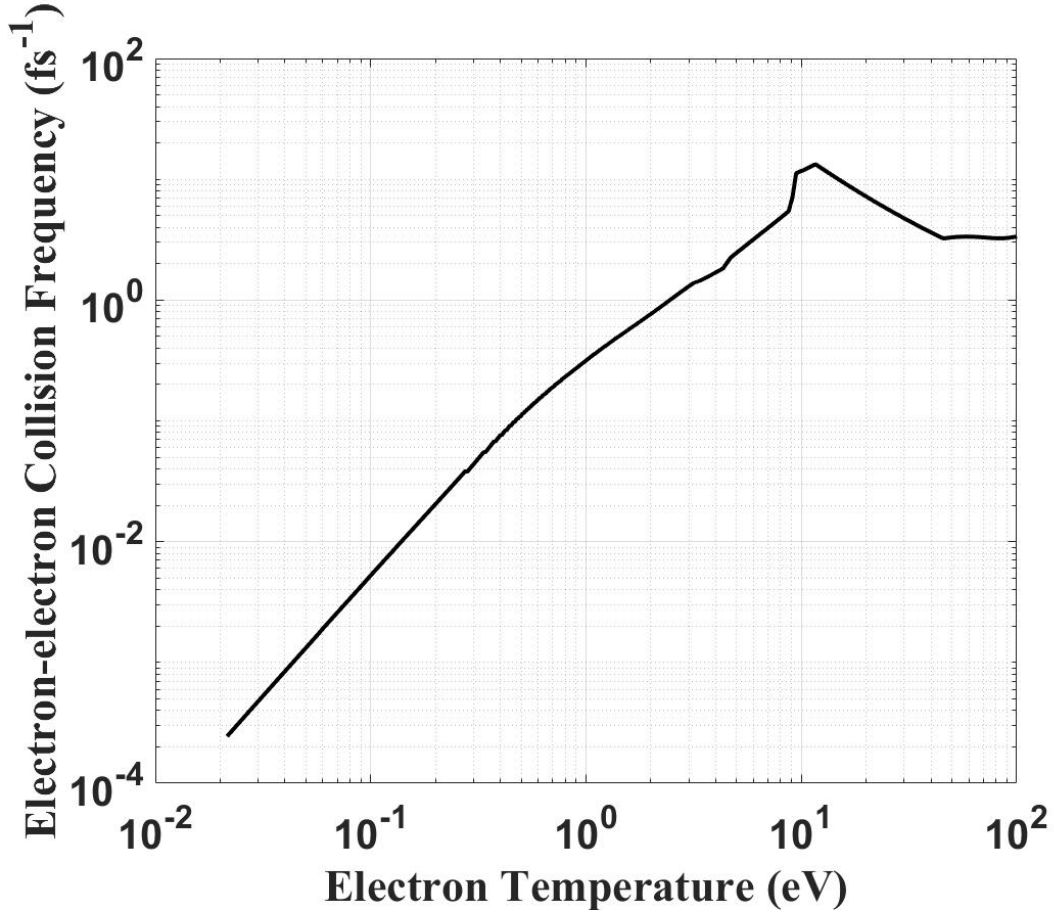


Figure 3.6. Electron-electron collision frequency of gold for electron temperatures up to 100 eV.

Fourment *et al.* [62] conducted a time and polarization resolved reflective interferometry measurement on femtosecond laser heated gold and deduced the effective electron collision frequency in the electron temperature range of 0.6-5 eV. In their experiments, the maximum lattice temperature reaches 880 K. The results are shown with our calculated effective collision frequencies in Figure 3.7.

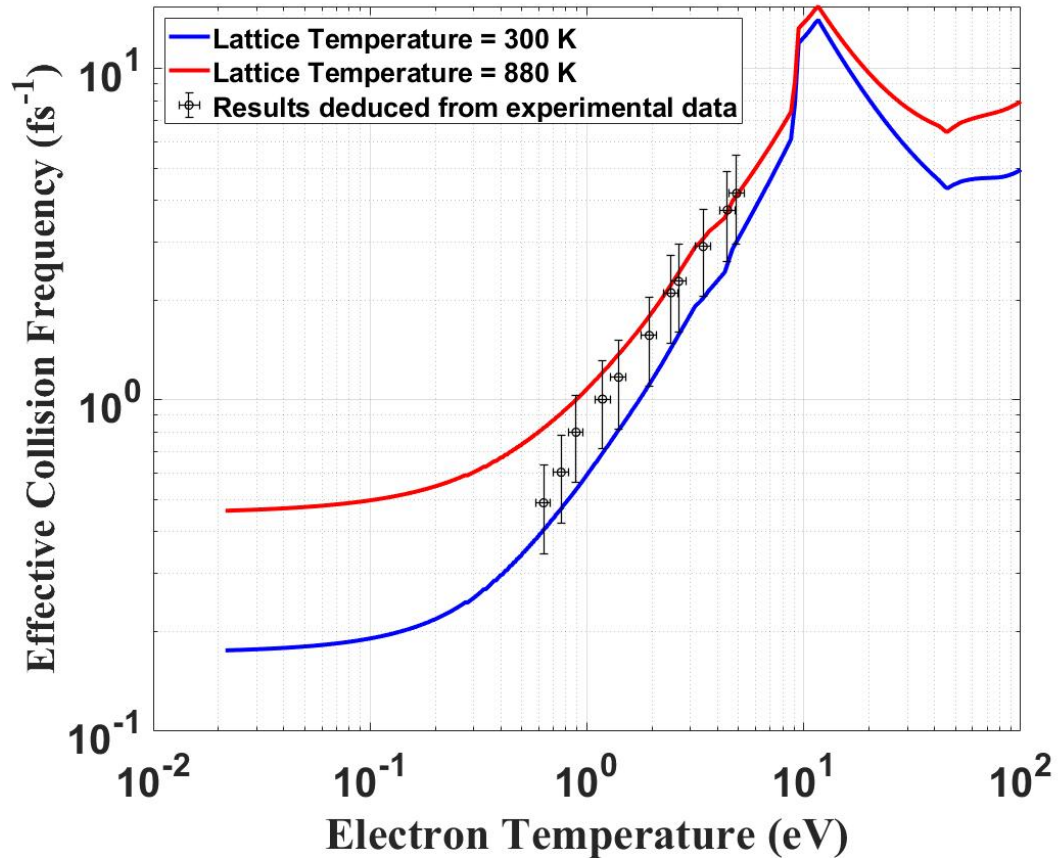


Figure 3.7. Electron effective collision frequencies of gold at 300 K and 880 K lattice temperature. The scatter points are results deduced from experimental data [62]

4. IMPORTANT PARAMETERS

4.1 Introduction

This Chapter discusses the parameters that are used in our simulations. After laser irradiation, the material will be in the state of warm dense matter. Warm dense matter is characterized as a condensed matter having electron temperatures between 1–100 eV. Since warm dense matter correlates with other well-defined states as shown in Figure 4.1, its thermodynamic properties are difficult to obtain compared to other states. There are three approaches to get these properties. One is interpolation method utilizing values from other states, but this method might oversimplify the complexity of warm dense matter. Another way is to calculate these properties from first principle using *ab initio* calculations which are commonly time-consuming. The last approach is to use analytical expressions. Also, constant value is sometimes used especially in early research. Note, the electron temperature regime that we are interested in for phase change and ablation study is below 50000 K.

Two interatomic potentials were used in our study, which are electron temperature independent and dependent interatomic potentials. Optical parameters, including reflectivity and laser penetration depth, are calculated based on Drude model and Fresnel equations.

4.2 Electron heat capacity

According to Kirkwood *et al.* [68], which later used by Suslova and Hassanein [35], [69], the electron heat capacity can be calculated by a smooth interpolation between the heat capacity in solid state (C_e^s) and hot plasma state (C_e^p). The derivations of these expressions are shown by Polek [58] and Suslova [16].

$$C_e^s = \frac{1}{2}\pi^2 \frac{T_e}{T_F} n_e k_b \quad (4.1)$$

$$C_e^p = \frac{3}{2} n_e k_b \quad (4.2)$$

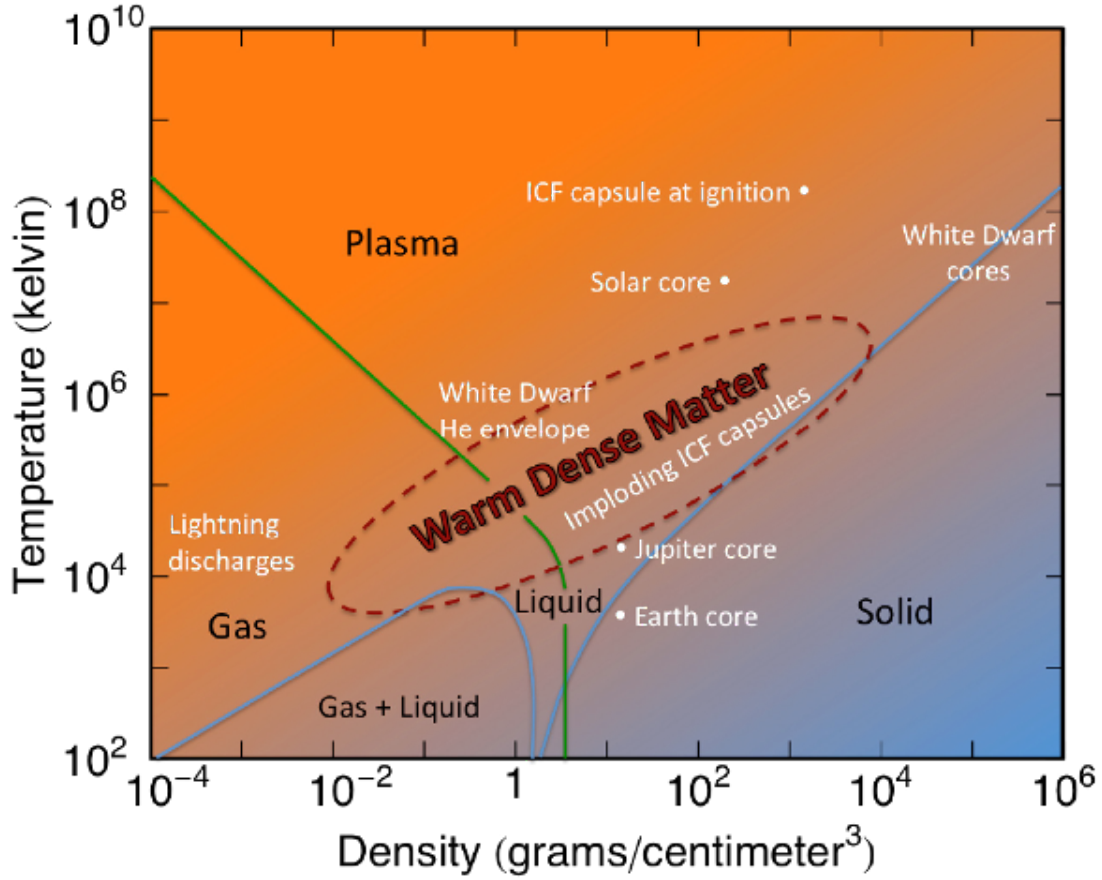


Figure 4.1. Phase diagram for warm dense matter. Figure is adopted from Los Alamos National Lab dense plasma theory website [67].

The overall electron heat capacity (C_e) by smooth interpolation is then given by

$$C_e = \frac{1}{\sqrt{(\frac{1}{C_e^s})^2 + (\frac{1}{C_e^p})^2}} = Zn_i k_b \frac{3\pi^2 T_e}{\sqrt{36T_F^2 + 4\pi^4 T_e^2}} \quad (4.3)$$

where $n_e = Zn_i$ and T_F is Fermi temperature.

To improve the accuracy of interpolation method for the transition between solid state and plasma, we introduced an electron transition factor (W_e) for the interpolation. This electron transition factor is very similar to the lattice transition fraction as in equation 3.10. The electron heat capacity C_e calculated by our modified interpolation method is given by

$$\begin{aligned}
W_e &= \frac{2}{e^{T_e/T_F} + 1} \\
C_e &= (1 - W_e) \times C_e^p + W_e \times C_e^s
\end{aligned} \tag{4.4}$$

From the definition, the electron heat capacity can be calculated by taking the derivative of the total electron energy density with respect to the electron temperature [60]:

$$C_e = \int_{-\infty}^{\infty} \frac{\partial f(\epsilon, \mu, T_e)}{\partial T_e} D(\epsilon) \epsilon d\epsilon \tag{4.5}$$

where $D(\epsilon)$ is the electron density of states at the energy level ϵ , and the Fermi distribution $f(\epsilon, \mu, T_e) = (e^{(\epsilon - \mu)/k_b T_e} + 1)^{-1}$. This value is obtained from Lin's *ab initio* calculations [22]. Apparently, Lin's calculation results are more accurate than the other two interpolation methods.

The electron heat capacity calculated by these three different methods are shown in Figure 4.2. Our modified interpolation method performs better than the smooth interpolation method in both low and high electron temperature regimes by comparing with Lin's calculation. Note that the ordinate is in log scale. However, the phase change and ablation results could be very sensitive to the electron heat capacity; therefore, we choose the more accurate calculation by Lin *et al.* for further study.

4.3 Lattice heat capacity

Lattice heat capacity will only be used in the continuum part since this parameter is implicitly described by interatomic potential in the atomistic part. In the continuum part, the lattice should normally stay in solid state for bulk materials and the temperatures in this part are much lower than the temperatures in the atomistic part. Therefore, we can assume the metal here stays in solid state and have 6 degrees of freedom in statistical mechanics.

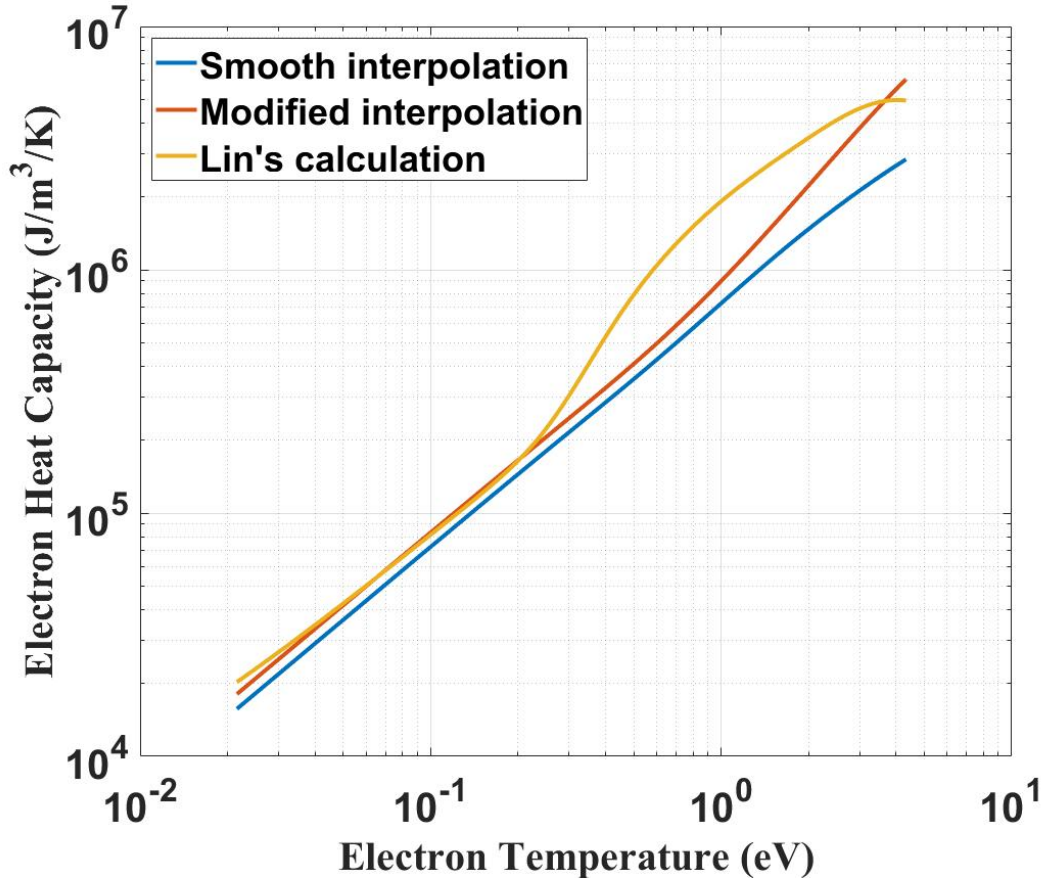


Figure 4.2. Electron heat capacity of gold calculated by three different methods.

Therefore, the heat capacity can be estimated by the equation below. For gold, the lattice heat capacity is 2.44 J/cm³/K.

$$C_l = 3n_l k_b \quad (4.6)$$

Also, we can use the experimental data at room temperature from the CRC Handbook [70], the lattice heat capacity is 2.49 J/cm³/K for gold. This parameter weakly depends on the lattice temperature, therefore it is reasonable to treat it as a constant [16].

4.4 Electron thermal conductivity

Similar to heat capacity, the overall electron thermal conductivity of metals can also be calculated by interpolating the thermal conductivities in cold solid state (K_e^s) [71] and in hot plasma state (K_e^p) from the plasma Spitzer heat conductivity expression [68].

$$K_e^s = \frac{C_e^s v_F^2}{3\nu_{e-ph}} = \frac{C_e^s \hbar^2 (3\pi^2 n_e)^{2/3}}{3m_e^2} \frac{1}{\nu_{e-ph}} \quad (4.7)$$

$$K_e^p = \frac{128(0.24 + Z)Zn_i T_e k_b^2}{3\pi(4.2 + Z)m_e} \frac{1}{\nu_{e-i} + \nu_{e-e}} \quad (4.8)$$

where $n_e = n_i$ for the calculation of gold in solid state.

The smooth interpolation method (equation 4.9) was proposed by Kirkwood *et al.* [68], and was later used by Suslova and Hassanein [35], [69]. The calculated conductivity is shown in Figure 4.3.

$$K_e = \sqrt{K_e^{p2} + K_e^{s2}} \quad (4.9)$$

We suggest that the lattice state should be considered when interpolating the electron thermal conductivity at the two extremes, similar to the calculation of electron-atom collision frequency as in equation 3.11. Our modified interpolation method is expressed by equation 4.10 and the corresponding electron thermal conductivity is shown in Figure 4.4.

$$K_e = \left(\frac{1 - W_l}{K_e^p} + \frac{W_l}{K_e^s} \right)^{-1} \quad (4.10)$$

The weight factor (W_l) here is the same as the transition weight shown in equation 3.10.

Anisimov and Rethfeld showed a widely used expression for electron thermal conductivity [24] based on similar calculations from previous works [72], [73], as shown in Figure 4.5.

$$K_e = C \frac{(\theta^2 + 0.16)^{5/4} (\theta^2 + 0.44) \theta}{(\theta^2 + 0.092)^{1/2} (\theta^2 + b\theta_i)} \quad (4.11)$$

where $\theta = k_b T_e / E_F$, $\theta_i = k_b T_i / E_F$ and for gold, $C = 353 \text{ W/K/m}$ and $b = 0.16$.

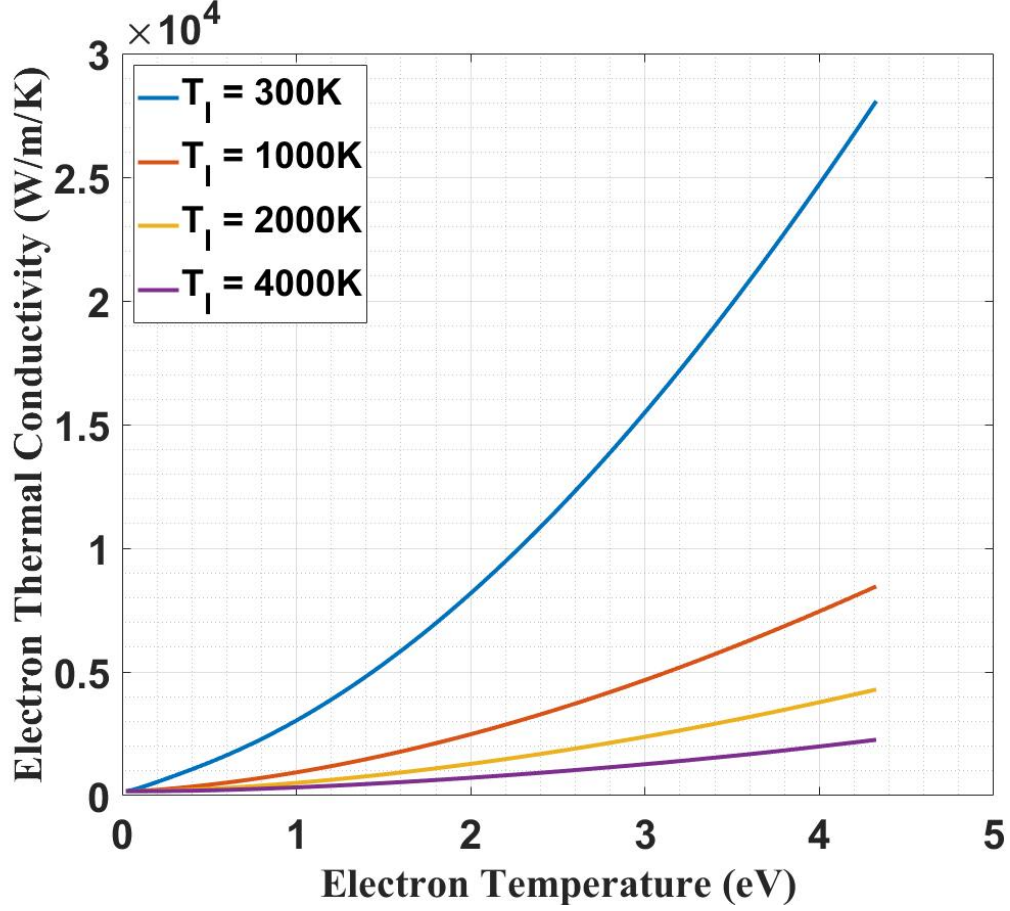


Figure 4.3. Electron thermal conductivity of gold calculated by smooth interpolation method at different lattice temperatures.

A more recent work in calculating the electron thermal conductivity was done by Petrov *et al.* [23]. The electron-electron collision contribution is calculated by kinetic equations [74] with the use of the electron energy spectrum [75] calculated by the density functional theory in the package VASP [76]. Petrov *et al.* considered both solid and liquid phases in calculating the electron thermal conductivity. In our simulations, we use the expression of the liquid phase if number density is lower than 88% of its original value.

The analytic approximation for the electron-electron collision contribution in the electron thermal conductivity for gold is given by

$$K_e^e = 10^4 \times \frac{1 + 0.03\sqrt{t} - 0.2688t + 0.9722t^2}{9.294x^{-4/3}t} \quad (4.12)$$

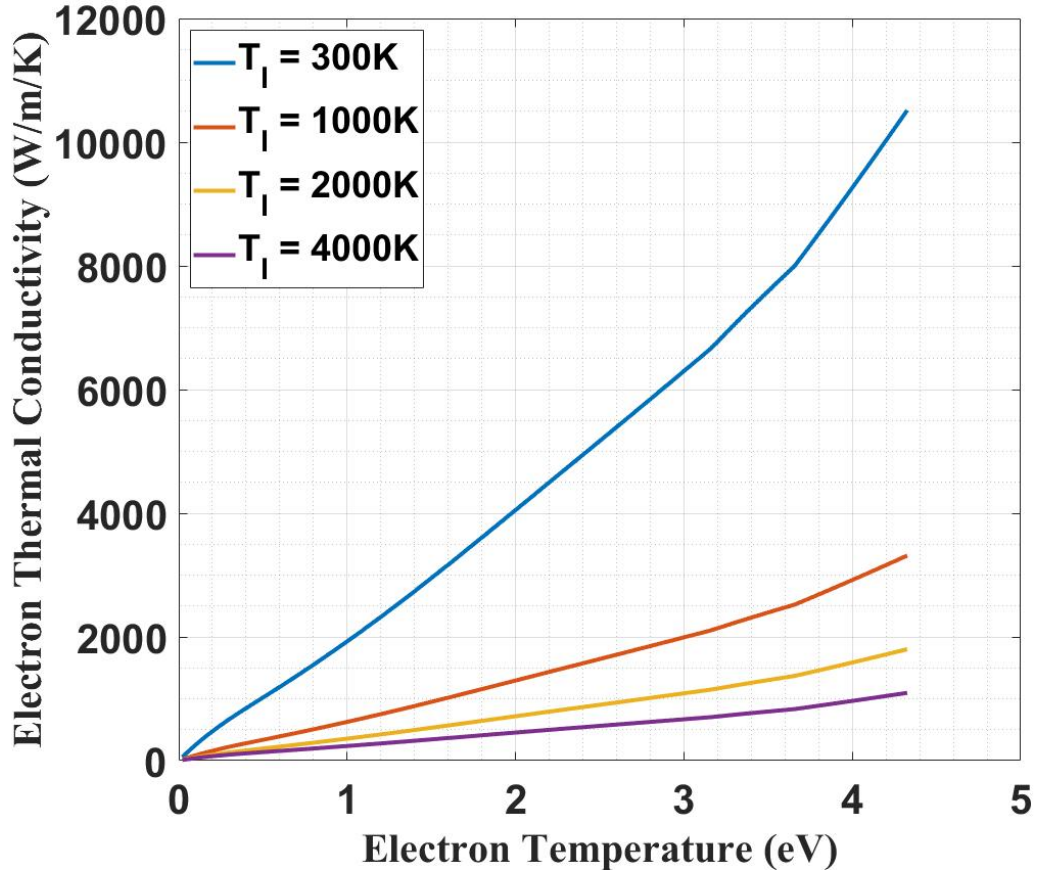


Figure 4.4. Electron thermal conductivity of gold calculated by modified interpolation method at different lattice temperatures.

where the normalized density $x = \rho/\rho_0$, the normalized temperature $t = 6k_bT_e/(xE_F)$ and ρ_0 is 19.5 g/cm^3 . We fixed a typo in the equation from the original paper [23]. Note the Fermi energy here and below is taken as 9.2 eV according to Petrov *et al.*.

The electron-lattice collision contribution to the electron thermal conductivity is considered based on the phase of the material. Therefore, K_e^s is the thermal conductivity in solid state and K_e^l is the thermal conductivity in liquid state. The following expressions for thermal conductivity of gold are in the units of W/m/K and the temperatures are in the units of K .

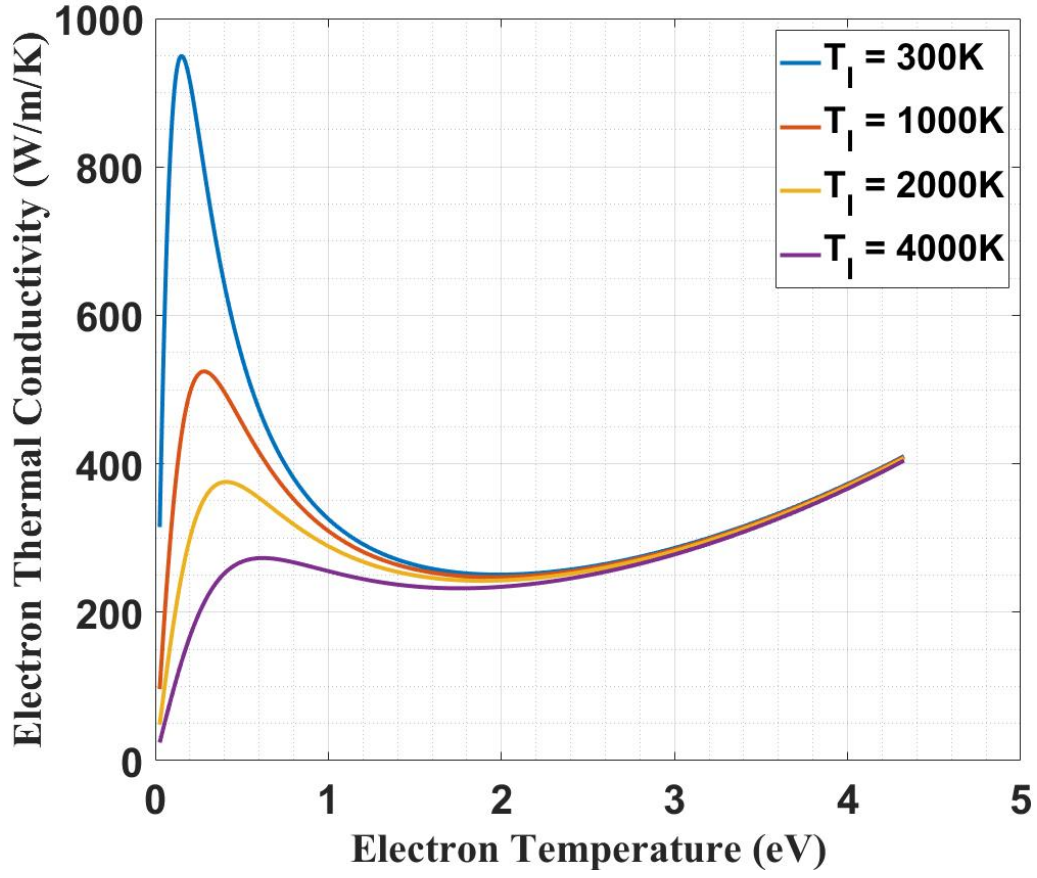


Figure 4.5. Electron thermal conductivity of gold calculated by equation 4.11 from Anisimov and Rethfeld [24] at different lattice temperatures.

$$\begin{aligned}
 K_e^s &= 318 \left(\frac{x}{x_{rt}} \right)^{4/3} \frac{y(x)}{y(x_{rt})} \frac{300}{T_i} \frac{\kappa(t)}{\kappa(t_{rt})} \\
 y(x) &= \frac{1.6678x^{8.84}}{1 + 0.6678x^{4.92}} \\
 \kappa(t) &= \frac{131t(1 + 3.07t^2)}{1 + 1.08t^{2.07}}
 \end{aligned} \tag{4.13}$$

$$\begin{aligned}
K_e^l &= \kappa(t) \frac{3254}{r_l(T_i)} x \left(\frac{x}{\chi_l(T_i)} \right)^2 \\
r_l(T) &= 148.5 + 0.1193T \frac{15337}{14000 + T} \\
\kappa(t) &= \frac{131t(1 + 3.07t^2)}{1 + 1.08t^{2.07}} \\
\chi_l(T) &= 0.887179 - 3.28 \times 10^{-5}(T - 1337) \\
&\quad - 3.0982 \times 10^{-9}(T - 1337)^2 - 1.64884 \times 10^{-13}(T - 1337)^3
\end{aligned} \tag{4.14}$$

In the above two expressions, the normalized density $x = \rho/\rho_0$, the normalized temperature $t = 6k_bT_e/(xE_F)$, ρ_0 is 19.5 g/cm³ and the subscript rt means room temperature. Therefore, the overall electron thermal conductivity can be expressed as follows:

$$K_e = \left(\frac{1}{K_e^e} + \frac{1}{K_e^{sl}} \right)^{-1} \tag{4.15}$$

where K_e^{sl} is either K_e^s or K_e^l depending on the current state of the material.

Figure 4.6 and Figure 4.7 show the electron thermal conductivity of solid and liquid state based on Petrov *et al.* [23].

Comparing with the results above, we can easily notice the overestimation in the high electron temperature regime and the inability to predict a peak at low lattice temperature by the two interpolation methods. Therefore, for more advanced simulations, we used the two analytical expressions from Petrov *et al.* [23] and Anisimov and Rethfeld [24].

4.5 Lattice thermal conductivity

The lattice thermal conductivity can be derived from kinetic theory [77], given by

$$k_l = \frac{C_l \sqrt{2k_b T_l / m_i + c_s^2}}{12n_i \pi r_0^2} \tag{4.16}$$

where r_0 is the atomic radius.

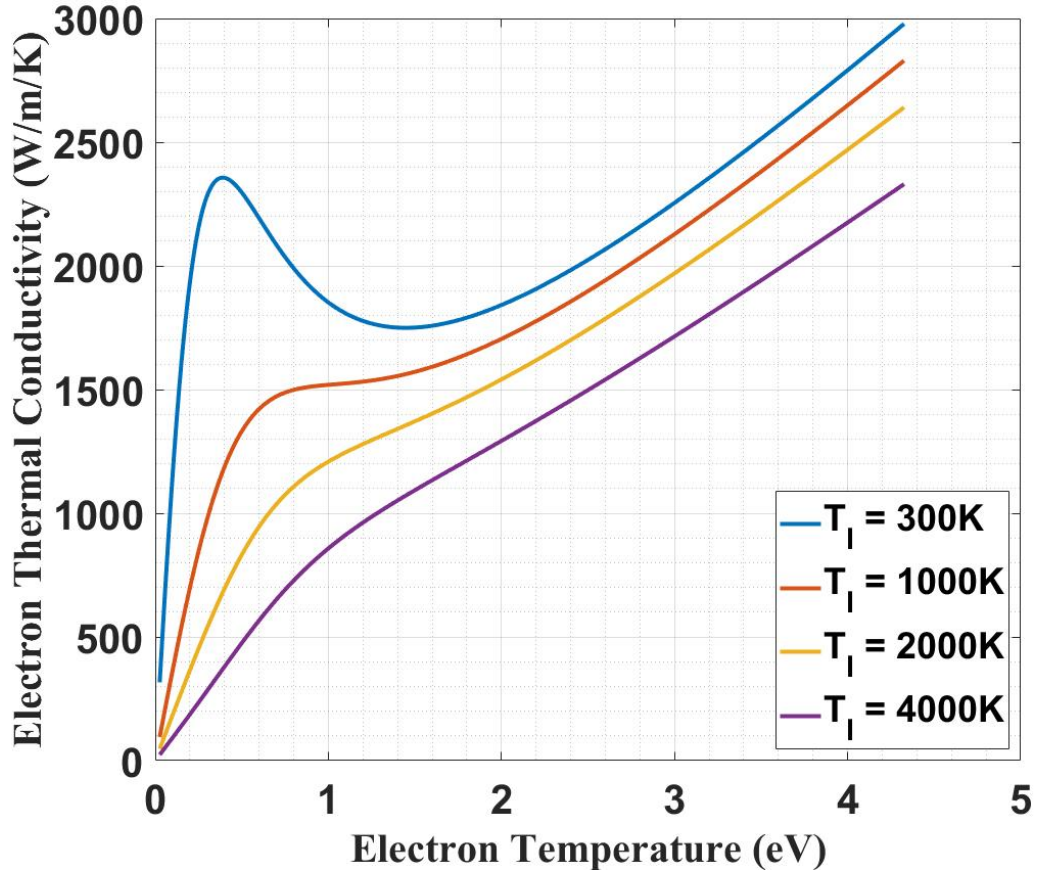


Figure 4.6. Electron thermal conductivity of solid gold calculated by expression from Petrov *et al.* [23] at different lattice temperatures. The material density is 19.3 g/cm^3 .

However, we only need to use the lattice thermal conductivity in the continuum part where the lattice temperature is usually smaller than the melting temperature. Taking into account that the electron thermal conductivity is much higher than the lattice thermal conductivity for metals, we can assume this value to be zero in the simulations, as in many other studies [27], [41], [42].

4.6 Electron-phonon coupling factor

Excluding constant values, we used two expressions for electron-phonon coupling factor in our simulations. One is calculated by Lin *et al.* [22] and the other one is an approximate

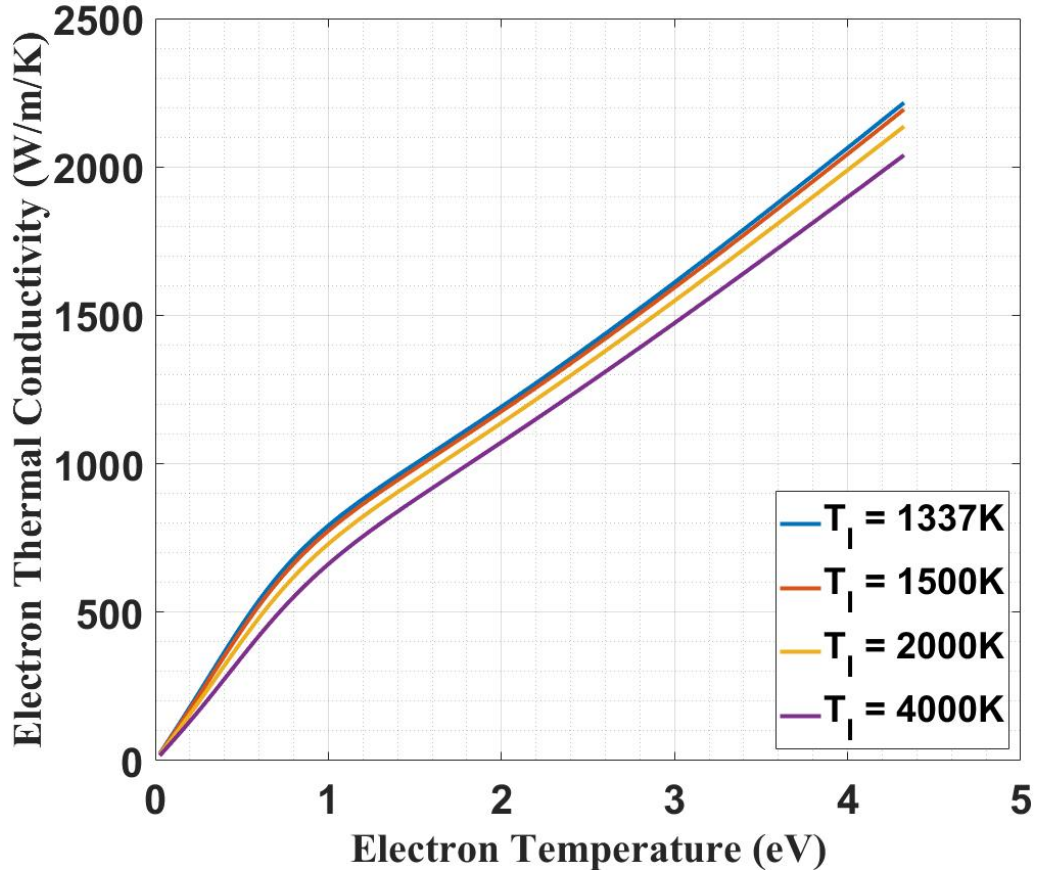


Figure 4.7. Electron thermal conductivity of liquid gold calculated by expression from Petrov *et al.* [23] at different lattice temperatures. The material density is 17.0 g/cm³.

expression proposed by Ashitkov *et al.* [25]. Lin's data are adopted from a table of values calculated using *ab initio* simulations. The approximation function of the coupling factor by Ashitkov is in the unit of W/K/m³ and is shown as follows:

$$G = \left(0.2 + \frac{4.3(k_b T_e)^{3.6}}{4(1 + (k_b T_e)^{3.5} + 0.9(k_b T_e)^{4.1})}\right) \left(\frac{\rho}{\rho_0}\right)^{5/3} \times 10^{17} \quad (4.17)$$

where temperature is in the unit of K and ρ_0 is 19.3 g/cm³.

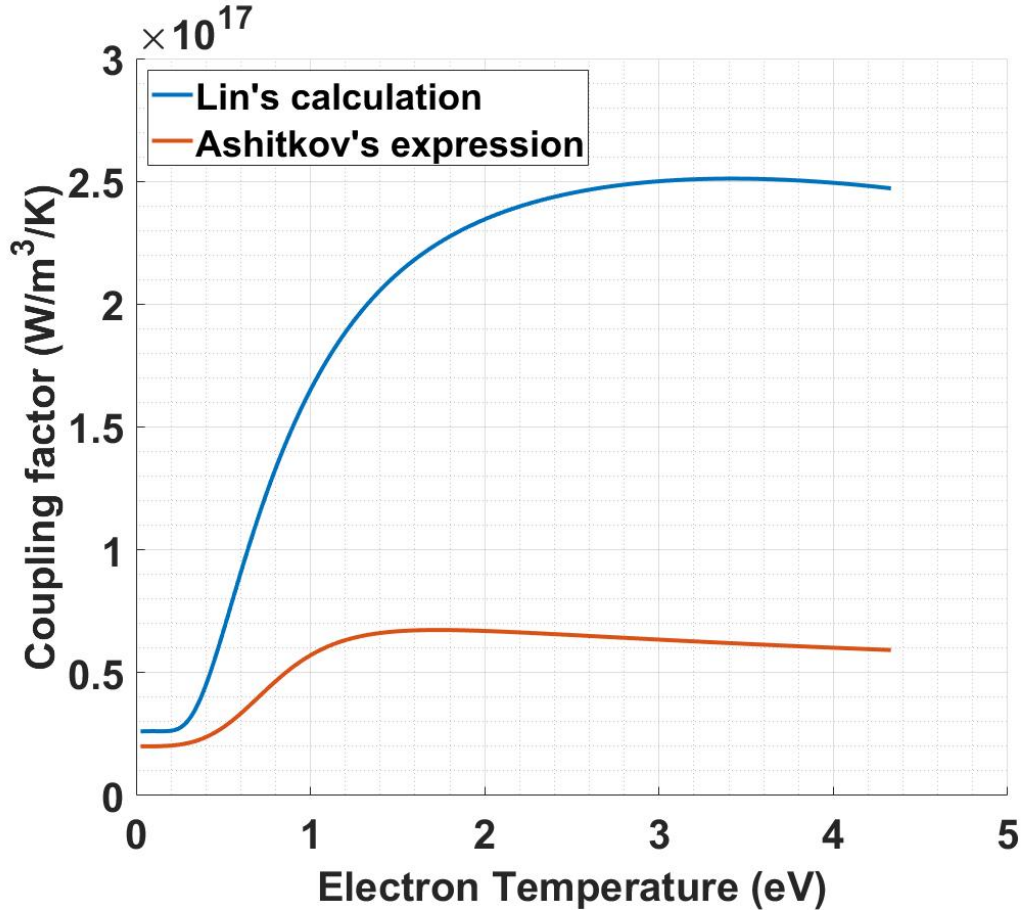


Figure 4.8. Electron-phonon coupling factor of gold by Lin *et al.* [22] and Ashitkov *et al.* [25].

For electron temperatures higher than 50000 K, the value of coupling factor can be calculated by

$$G = 3 \frac{m_e}{m_i} \nu_{e-a} Z n_i k_b \quad (4.18)$$

which Polek [58] showed may overestimate the coupling factor.

Table 4.1 summaries the different approaches for obtaining the electron heat capacity (C_e), electron thermal conductivity (K_e), and electron-phonon coupling factor (G) as mentioned above.

Table 4.1. Different approaches to calculate the electron heat capacity (C_e), electron thermal conductivity (K_e), and electron-phonon coupling factor (G)

C_e	K_e	G
Smooth Interpolation (Eq. 4.3)	Smooth Interpolation (Eq. 4.9)	Lin’s data [22]
Modified Interpolation (Eq. 4.4)	Modified Interpolation (Eq. 4.10)	Eq. 4.17 [25]
Lin’s data [22]	Eq. 4.11 [24]	
	Eq. 4.15 [23]	

4.7 Effects of electron thermal conductivity and electron-phonon coupling factor

To study the effects of electron thermal conductivity and electron-phonon coupling factor, we used two sets of electron thermal conductivity and two sets of electron-phonon coupling factor. The higher electron thermal conductivity (“large” in the figures) is from Petrov’s study [23] and the lower one (“small” in the figures) is from Anisimov and Rethfeld’s work [24]. Similarly, the larger electron-phonon coupling factor (“large” in the figures) is from Lin’s data [22] and the smaller one (“small” in the figures) is from Ashitkov’s approximation equation [25], as shown in equation 4.17.

In this simulation, we used 500 nm gold with 100 mJ/cm² absorbed fluence to show the level of deviations when using different approaches in the calculation of the two major parameters. The lattice temperature profiles at 1 ps and 10 ps obtained with different values of electron thermal conductivity and electron-phonon coupling factor are shown in Figure 4.9.

As shown in Figure 4.9, at 10 ps, both large value of electron-phonon coupling factor G and small value of electron thermal conductivity K_e lead to high temperatures in the region close to the surface. However, at earlier times, large value of G has a broader impact area, but a less severe effect on the surface compared with small K_e .

4.8 Adjustments

The electron thermal conductivity and the electron-lattice coupling factor are adjusted in the simulation of material evolution when electron and lattice temperatures reach equilibrium

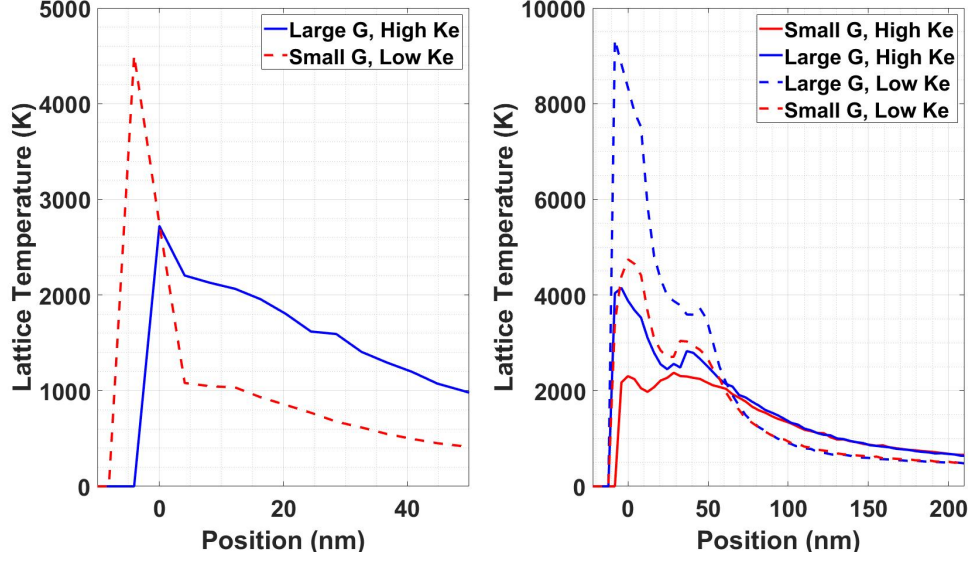


Figure 4.9. Lattice temperature profiles at 1 ps (left) and 10 ps (right) for different values of electron thermal conductivity and electron-phonon coupling factor.

to avoid numerical oscillations in the hybrid model. The electron thermal conductivity will be set to 20% of its calculated value and the electron-lattice coupling factor will be set to 500% of its calculated value after equilibrium.

4.9 Optical parameters

More details of this part are in Appendix A.

Relative permittivity is calculated by Drude dielectric function, given by

$$\epsilon_r = 1 - \frac{\omega_p^2}{i\omega\nu_{eff} + \omega^2} \quad (4.19)$$

where the plasma frequency $\omega_p = \sqrt{Zn_i e^2 / (\epsilon_0 m_e)}$ and laser angular frequency $\omega = 2\pi c_0 / \lambda$, where c_0 is speed of light and λ is laser wavelength. We now introduce two parameters from the relative permittivity, $n_1 = \text{Re}(\sqrt{\epsilon_r})$ and $n_2 = \text{Im}(\sqrt{\epsilon_r})$.

The reflectivity R is calculated by Fresnel formula.

$$R = \left\| \frac{1 - n_1 - in_2}{1 + n_1 + in_2} \right\|_2^2 \quad (4.20)$$

The penetration depth is defined as the length when laser intensity being attenuated by $1/e$ as the laser travels through the materials.

$$l_p = \frac{\lambda}{4\pi n_2} \quad (4.21)$$

4.10 Interatomic potential

There are several interatomic potentials for gold used throughout our work. One is by G.P. Purja Pun which is available on the NIST Interatomic Potentials Repository website. The potential is easy and sufficient to study the melting of gold. However, it might overestimate the bond strength for high temperature according to our study, therefore it is not suitable for studying the ablation mechanisms.

The other one is the so-called electron temperature dependent (ETD) interatomic potential. The ETD interatomic potential for gold is adopted from Norman’s work [43] and verified by Daraszewicz *et al.* [78] and Stegailov and Zhilyaev [79], which is also accessible through the NIST Interatomic Potentials Repository. In the interatomic potential file, there are five interatomic potentials for gold calculated with 0.1 eV, 1.5 eV, 3.0 eV, 4.5 eV, and 6.0 eV electron temperatures. In our work, we used two sets of interatomic potential data based on the above values. One set is the “cold part” of the interatomic potentials calculated with 0.1 eV electron temperature, called the 1T potential, which was also used in previous work [57]; the other set is the potential combining the five potentials, called the 5T potential. In the case of the 5T potential, the interatomic potential is updated dynamically during the MD simulations according to the local electron temperature.

5. ANALYSIS

5.1 Temperature

The temperatures of the two subsystems in the continuum part and the temperature of the electron subsystem in the atomistic part are obtained from the results of TTM calculations. The temperature of the lattice subsystem is defined as the average kinetic energy due to thermal vibration, therefore we have

$$T_l = \frac{\sum_{cell} m_i \vec{v}_T^2}{3k_b N_{cell}} \quad (5.1)$$

where the sum is the sum for all atoms in a cell and N_{cell} is the total number of atoms in that particular cell. Thermal velocity \vec{v}_T as in equation 2.5 is introduced to avoid the effect of the collective movement of atoms on temperature calculation.

5.2 Density and Voronoi tessellation

The volume of each atom was calculated by LAMMPS ‘voronoi/atom’ function which calculates the volume of the Voronoi cell around each atom. The density therefore is calculated by inverting the average volume.

5.3 Pressure

Since we use the EAM inter-atomic potential, there are not any pairwise or bond contributions to the stress. The only contribution will be from the kinetic energy and the internal constraint forces of the atom. The calculation of the stress of an atom is calculated by

$$S_{ab} = -[mv_a v_b + W_{ab}] \quad (5.2)$$
$$W_{ab} = \sum_{n=1}^{N_f} r_{i_a} F_{i_b}$$

where the first term shows the kinetic contribution, and the second term is coming from the forces by other atoms and the electron subsystem. The total pressure can therefore be

calculated by summing up the stress/atom value along laser coming direction for each cell. The virial contribution W_{ab} is calculated and recorded by running LAMMPS simulations. The kinetic energy term will then be calculated from lattice temperature and atomic volume and added to obtain the overall stress.

5.4 Entropy

The entropy for an atom i is computed by

$$s_S^i = -2\pi\rho k_b \int_0^{r_m} [g(r) \ln g(r) - g(r) + 1] r^2 dr \quad (5.3)$$

$$g_m^i(r) = \frac{1}{4\pi\rho r^2} \sum_j \frac{1}{\sqrt{2\pi\sigma^2}} e^{-(r-r_{ij})^2/(2\sigma^2)}$$

where r is the distance, $g(r)$ is the radial distribution function of atom i , ρ is the density of the system. The sum in j goes through the neighbors of atom i and σ is the smoothing parameter.

5.5 Melting depth

Since the targets in our simulations are symmetric in the directions normal to laser incident direction, we identify the melting depth by locating the solid-liquid interface. The S-L interface is calculated from the entropy gradients. As shown in Figure 5.1, the entropy gradient will have a very narrow peak at the S-L interface. Therefore, we can easily use this to find the S-L interface and use it to get the melting depth. This method is much easier than calculating the local order parameter [27] to determine the material phase.

In this simulation, the laser intensity is 6.0×10^{12} W/cm², the laser fluence is 600 mJ/cm², pulse duration is 100 fs, electron heat capacity (C_e), electron thermal conductivity (K_e) are from interpolation methods, electron-phonon coupling factor (G) is from Lin's data, reflectivity and penetration depth are calculated by collision theory, bulk material with 200 nm in MD simulation, Purja Pun's interatomic potential [80] is used and the electron blast force vanishes at the surface.

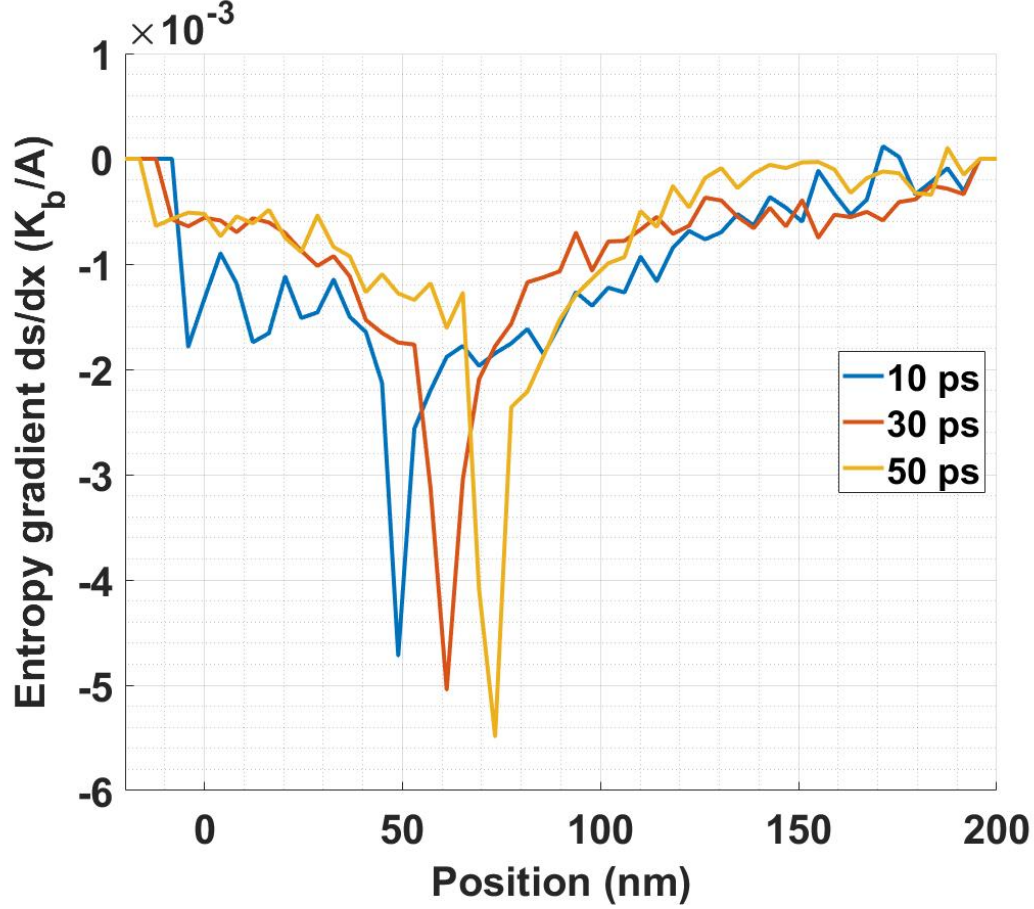


Figure 5.1. Entropy gradients in laser incident direction of gold at 10 ps, 30 ps and 50 ps.

Figure 5.2 shows the S-L locations predicted by entropy gradients from Figure 5.1. This shows that the method using entropy gradients to find the S-L interface has high level of accuracy.

5.6 Ablation depth

The ablation depth is defined by the number of ablated atoms divided by the areal density at room temperature. Atoms are considered ablated if they are separated by at least one void layer from the bulk. A void layer is a layer with number density less than 10% of its room temperature value in the target.

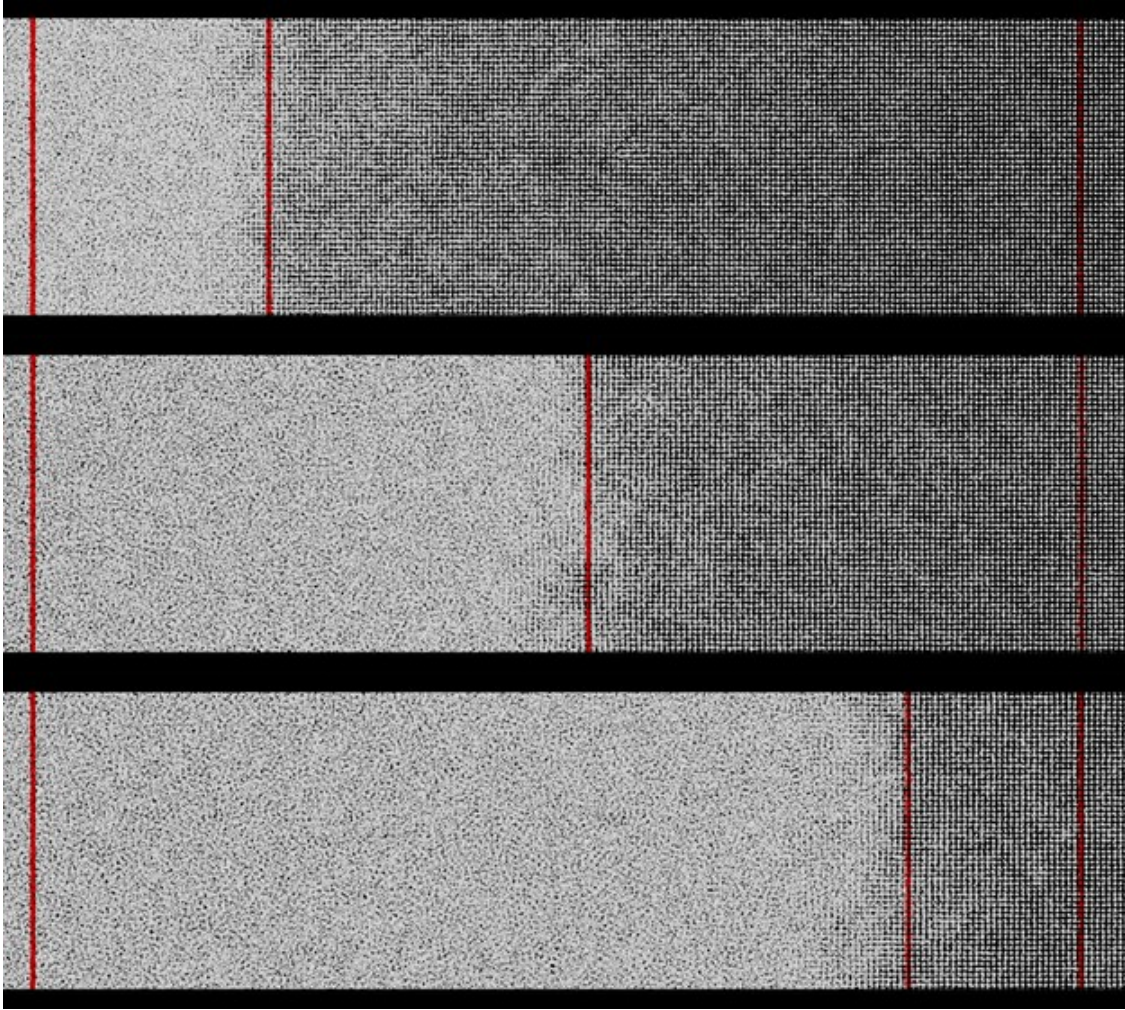


Figure 5.2. Phase change locations (S-L interfaces) predicted by entropy gradients at 10 ps (top), 30 ps (middle) and 50 ps (bottom), corresponding to Figure 5.1. The left and right latches correspond to the location of 40 nm and 80 nm in the target, and the middle latch shows the location of corresponding entropy gradient peak.

5.7 Nanocluster production

LAMMPS ‘compute cluster/atom’ function assigns for each atom a cluster ID. A cluster here is defined as a group of atoms, within which the atoms are located at the distance smaller than the specified cutoff distance; and any atom in one cluster has a distance greater than the cutoff distance between the atoms in any other cluster. By applying this function,

we can easily obtain the nanocluster size and spatial distribution from the LAMMPS output files.

In the following simple simulation, we studied the spatial and size distribution of nanocluster distribution for gold. Cluster size means the number of atoms consisting of the cluster. In this simulation, the laser intensity is $1.75 \times 10^{13} \text{ W/cm}^2$, the laser fluence is 1.75 J/cm^2 , pulse duration is 100 fs, electron heat capacity (C_e), electron thermal conductivity (K_e) are from the interpolation methods, electron-phonon coupling factor (G) is from Lin's data, reflectivity and penetration depth are calculated by collision theory, bulk material with 122.4 nm in MD simulation, Purja Pun's interatomic potential is used and the electron blast force vanishes at the surface.

Figure 5.3 shows the creation of more smaller clusters than larger clusters, because the ablation mechanism for these clusters is vaporization and smaller clusters are easier to form under vaporization.

Figure 5.4 shows the spatial distribution of nanocluster with 1 and 2 atoms. Size 2 clusters are more spatially confined than size 1 clusters because the average velocity away from the surface of larger cluster is smaller.

However, these simple results cannot accurately reflect the nanoparticle production due to several reasons. First, the used interatomic potential overestimates the bond strength at the ablation temperature regime as mentioned before. Therefore, only vaporization can be observed even with such high laser fluence. To obtain more accurate results, one need to use a suitable interatomic potential, larger simulation lateral area and longer simulation time. However, the latter two are limited under our current resources. Our work was concentrated on detail studies of the interatomic potential effects and the qualitative ablation process.

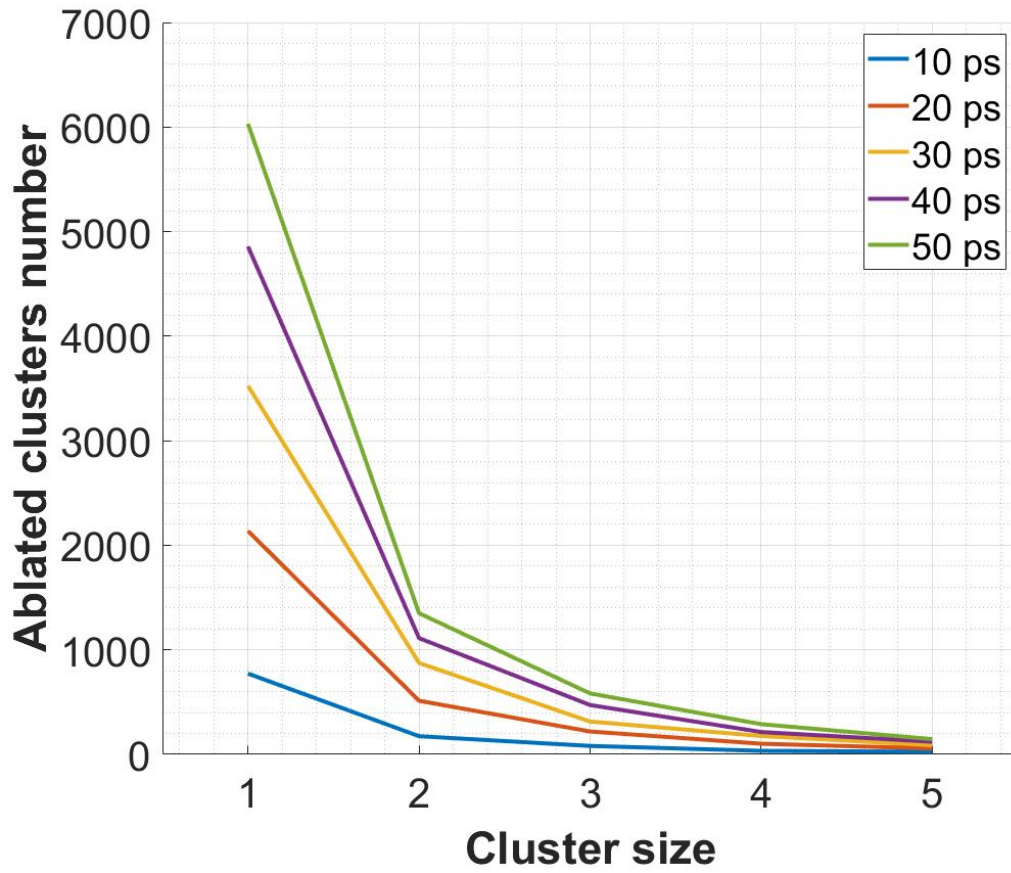


Figure 5.3. Number of clusters with different sizes at times of 10 ps, 20 ps, 30 ps, 40 ps, and 50 ps.

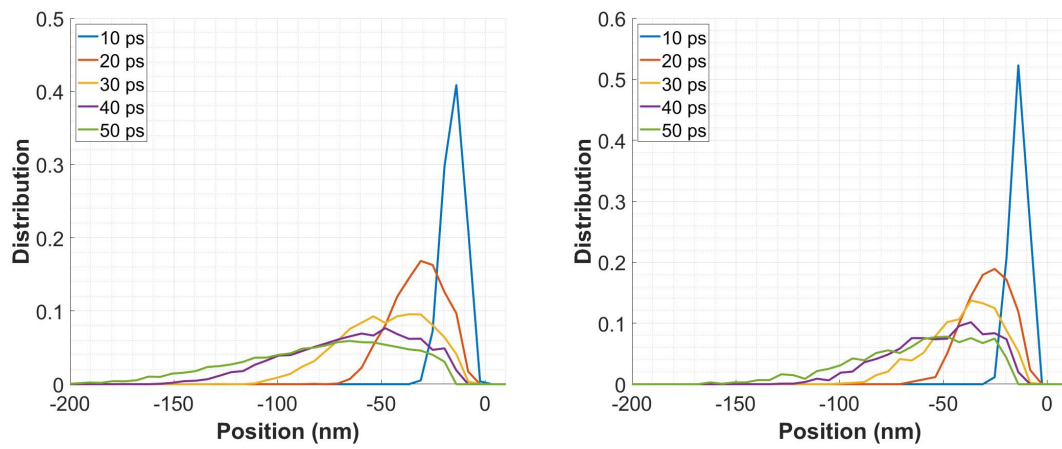


Figure 5.4. Spatial distribution of nanocluster with size 1 (left) and size 2 (right). Position 0 nm means the initial location of the target surface.

6. PHASE CHANGE STUDY

6.1 Introduction

In this chapter, the simulated surface movement results were benchmarked with the experimental data. Furthermore, we extensively studied the effects of target thickness on temperature and phase change (melting). Three thicknesses, 200 nm, 500 nm, and 1500 nm (bulk), and two absorbed fluences, 100 and 150 mJ/cm², were studied. The results for the cases of 200 nm thick material are very different from the results for 500 nm and bulk material. Homogeneous melting and surface shrinking were only observed in the case of 200 nm. Homogenous melting occurs when the electron subsystem reaches thermal equilibrium before lattice-electron equilibrium and melting happens simultaneously in a large area of the material with absorbed fluence 100 mJ/cm² and above.

Even though we believe the electron blast force should vanish at the surface, we studied the blast force which peaks at the surface and found this blast force would cause short ablation.

6.2 Simulation setup

For the simulated cases, the target material gold is initially at room temperature (300 K). The MD simulation box with a lateral area of 4.08 nm × 4.08 nm has periodic boundary conditions in the directions perpendicular to the incident laser, and a fixed boundary condition in the laser incident direction. The cell sizes for lattice and electron temperatures are 4.08×4.08×4.08 nm³ and 4.08×4.08×20.0 nm³ in the MD and TTM parts, respectively. The laser pulse is 80 fs with a Gaussian shape. The timestep in MD is 1 fs. Laser penetration depth is 13 nm and absorbed laser fluence is considered. The electron blast force peaks at the surface as described in equation 2.7.

The electron heat capacity (C_e) is adopted from Lin's data [22], electron-phonon coupling factor (G) is calculated from Ashitkov's approximation equation (equation 4.17) [25], the electron thermal conductivity (K_e) is adopted from work by Petrov *et al.* [23] as described in previous chapter. The interatomic potential for gold is from Purja Pun's work [80].

6.3 Surface movement benchmarking

Initially, we modeled recent experiments to determine the range of parameters which will allow us to reproduce the experimental results. A laser pulse with absorbed fluence of 100 mJ/cm² and 80 fs duration is used in these simulations. The target is 500 nm gold.

Figure 6.1 shows our simulation results as well as the experimental data from Ashitkov *et al.* [25]. Laser incident fluences are given for the experimental results while laser absorbed fluence was used in the simulation.

Our results very well reproduce experimental data at earlier time before 50 ps obtained for the laser fluence of 1.56 J/cm². However, the surface movement velocity in our results after 100 ps fits well with the experimental data of lower laser fluence of 1.3 J/cm². Deviation of our results from the measurements of surface displacement at later time can be explained by the sensitivity of surface measurement near laser ablation threshold and the inaccuracy in the methods and parameters for modeling of material in the metastable phase. Therefore, it is reasonable to state that the input laser fluence in accordance with our simulation is between 1.3 J/cm² and 1.56 J/cm². By simple calculation, we can predict the overall reflectivity of the gold surface as 91.67% to 93.59% for the 1240 nm lasers.

6.4 Phase change simple study

Further analysis of our simulation results explained changes in the surface displacement curve. We studied the phase change in the target during the first 300 ps. Figure 6.2 shows the shift of solid-liquid position and melted layer thickness as functions of time. The entropy gradients were used to determine the location of the Solid-Liquid interface as described in previous chapter.

The roughness in the two graphs of Figure 6.2 is due to the fact that we neglect the coexistence region of liquid and solid, and the S-L interface is not a 2D cross-section, but a 3D region. However, our method is simple and sufficient enough to study the trend of phase change. The melting process starts at around 5 ps and reaches its peak at about 100 ps. After 100 ps, although the melted region is growing slowly due to thermal conduction, the S-L interface is moving back towards to the original surface position because of the thermal

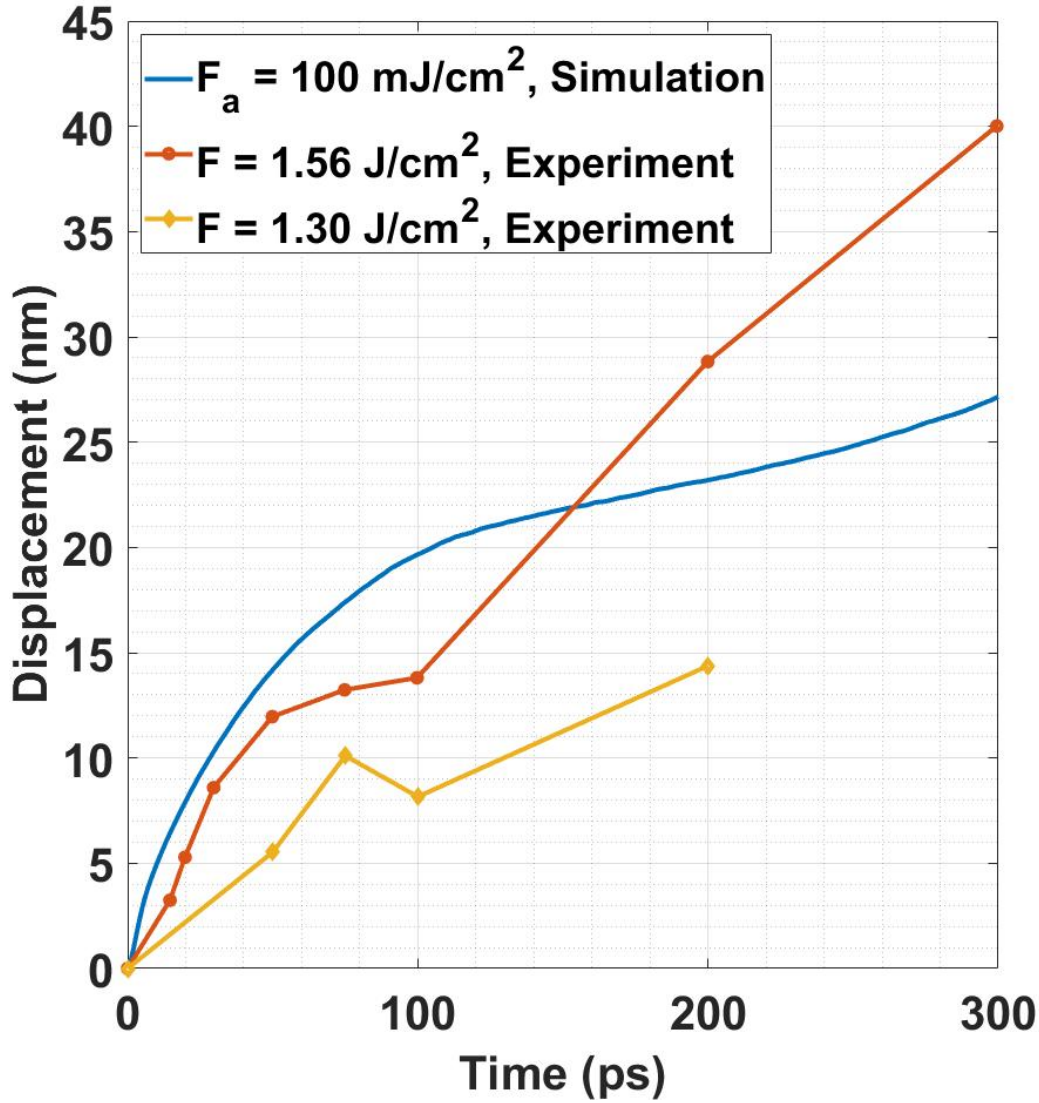


Figure 6.1. Displacement of gold surface obtained in the simulation for absorbed fluence 100 mJ/cm^2 and experimental data [25] with laser fluences 1.56 and 1.30 J/cm^2 .

expansion of the solid region. Therefore, relatively high rate of surface movement at first 100 ps results from both the growing of melted layer and the thermal expansion of the solid layer. Here we can exclude the effect of evaporation because the highest lattice temperature after 100 ps is still far below the boiling point of gold (3000 K) as shown in Figure 6.3.

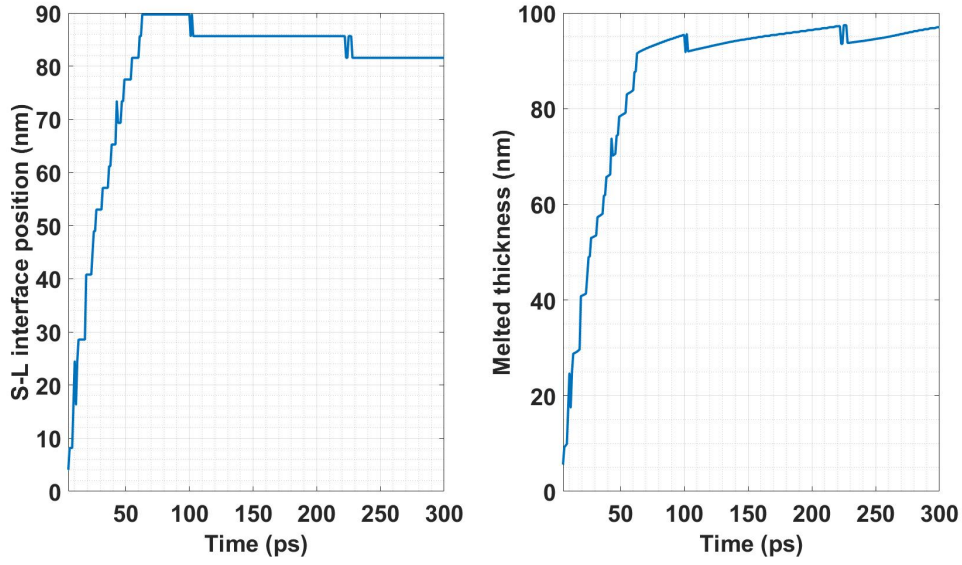


Figure 6.2. Solid-liquid interface position (left) and melted thickness (right) profiles for 500 nm gold target with absorbed laser fluence 100 mJ/cm^2 . Melted thickness is calculated from number of atoms in the melted layer with lattice density correspondent to room temperature.

6.5 The effects of target thickness on temperature and phase change

Three different thicknesses of materials, which are 200 nm, 500 nm, and 1500 nm (bulk), are simulated to study the effects of target thickness with the determined effective thermodynamic parameters. The bulk material in our simulation consists of 500 nm atomistic part and 1000 nm continuum part in the direction of laser irradiation. The other two cases correspond 200 nm and 500 nm gold layers deposited onto a thermal insulator substrate, and therefore we use a fixed boundary condition on the rear surface of the target.

Comparison of the cases between 500 nm and bulk in Figure 6.4 shows that although the layer thickness does not have outstanding effect on the surface temperature, it can significantly affect the temperatures at the deeper part of the material, because the part deeper than 500 nm in the bulk material acts as an extra heat sink compared to the 500 nm target. The temperature evolution on the surface is limited by the electron thermal conductivity, which is an increasing function of electron temperature, therefore the electron temperatures are comparable for these two cases. Unlike 500 nm and bulk material, thin

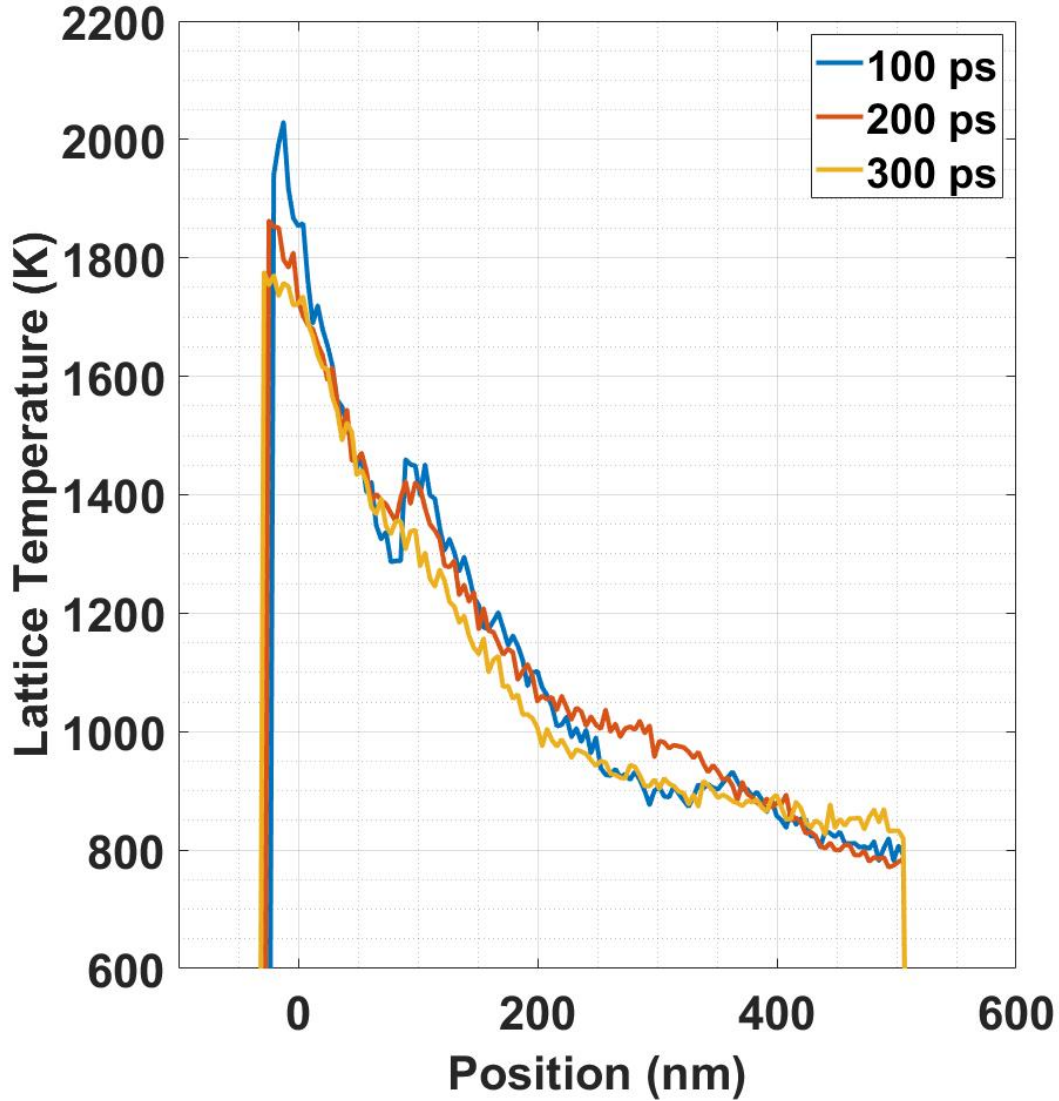


Figure 6.3. Lattice temperatures at 100 ps, 200 ps and 300 ps with absorbed fluence 100 mJ/cm^2 . The peaks in the middle indicate the solid-liquid interface.

gold film with 200 nm on the substrate has a much higher temperature than the previous two. When the bulk material is considered as a surface layer with an additional heat sink, this heat sink has much greater effect on heat dissipation in the thinner surface layer.

Figure 6.5 and Figure 6.6 show the temperature profiles of the lattice at 10 ps and 300 ps after laser irradiation, respectively.

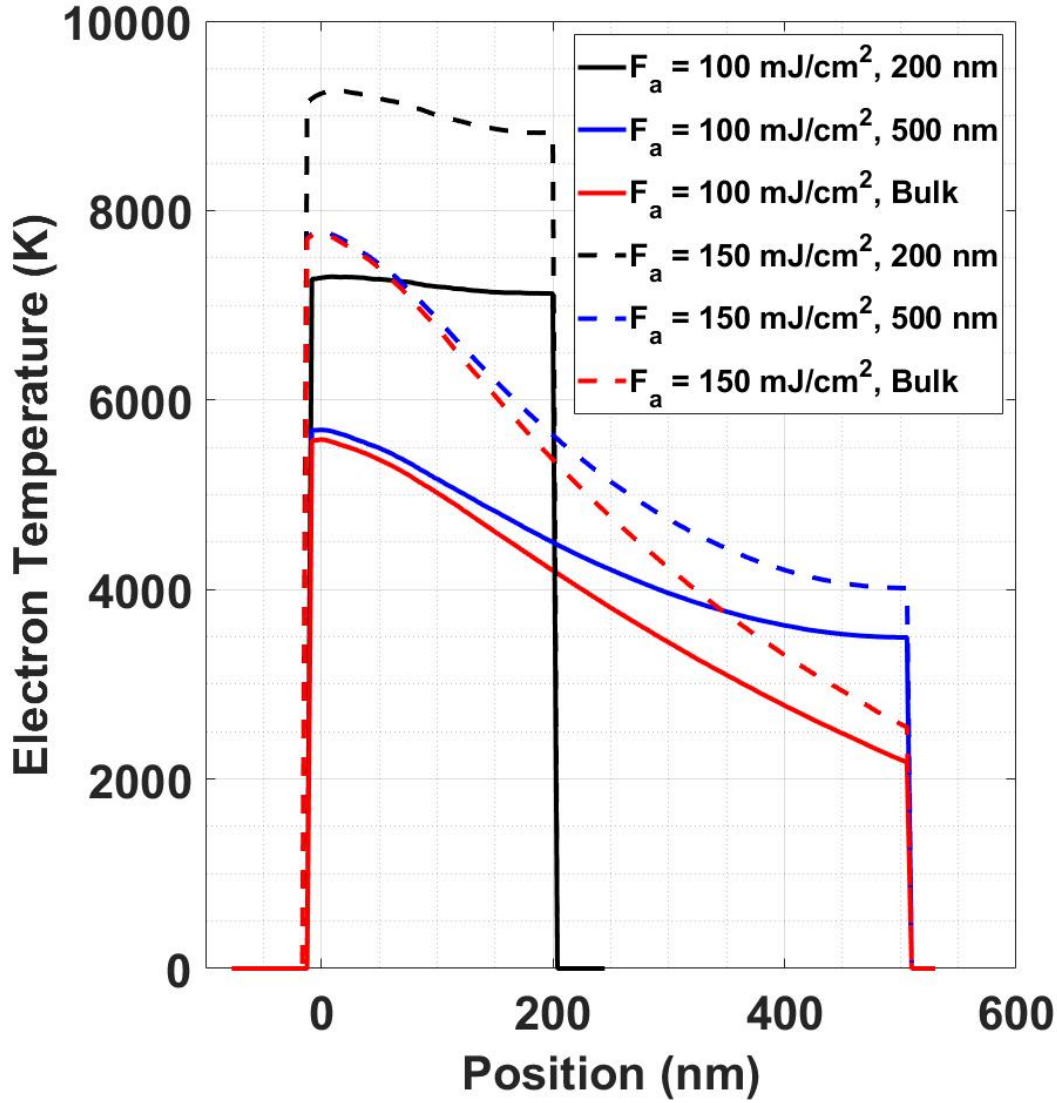


Figure 6.4. Electron temperatures at 10 ps after laser irradiation for two different absorbed laser fluences (100 mJ/cm^2 and 150 mJ/cm^2) and three different target thicknesses (200 nm, 500 nm, bulk)

In Figure 6.5, there are two peaks in the middle for the cases of 150 mJ/cm^2 . The one at around 15 nm represents the S-L interface and the one at around 50 nm is an overheating peak following the strong compressive stress wave.

At 300 ps, as shown in Figure 6.6, the electron temperature profiles are the same with their corresponding lattice temperature profiles since the lattice and electron subsystems

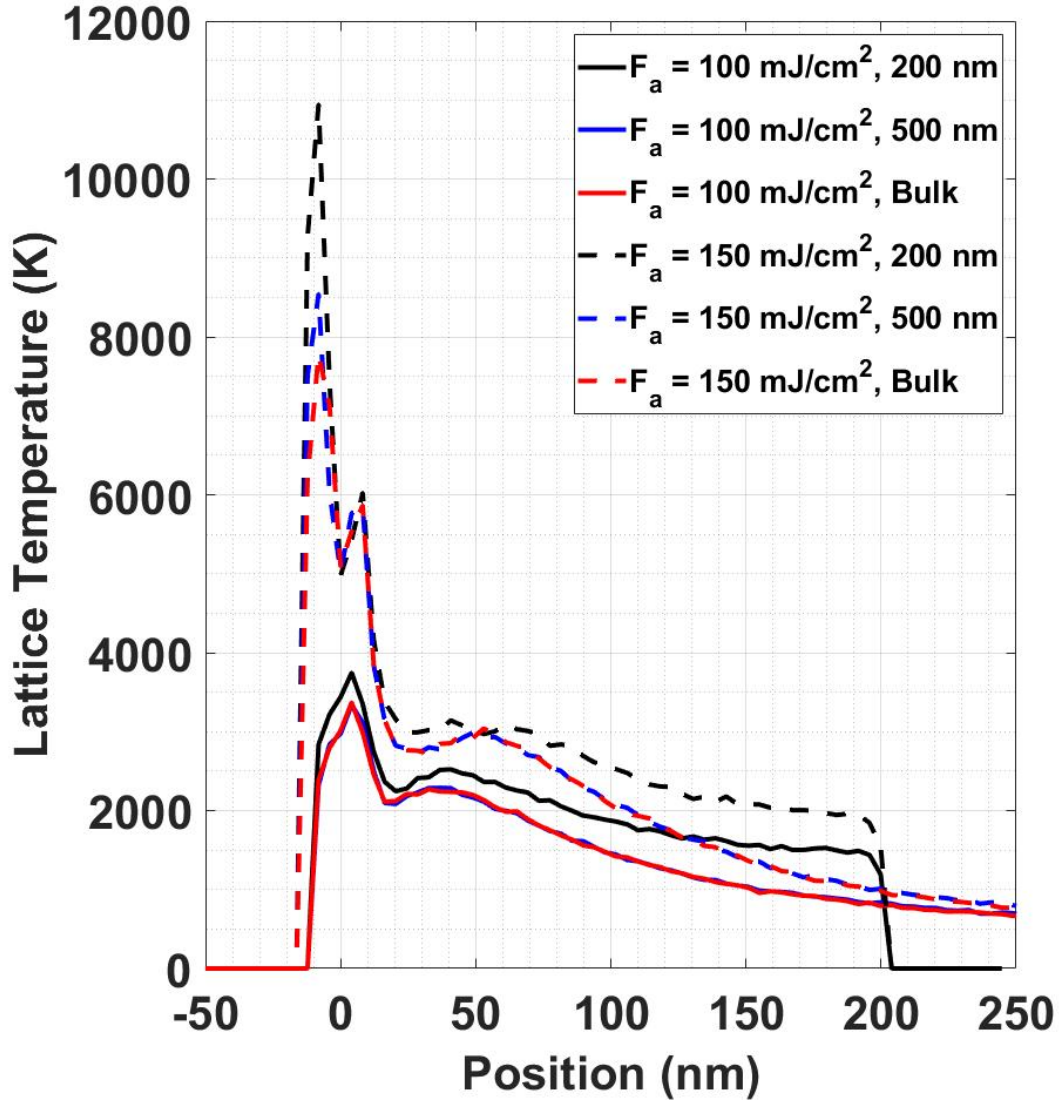


Figure 6.5. Lattice temperatures at 10 ps after laser irradiation for two different absorbed laser fluences (100 mJ/cm^2 and 150 mJ/cm^2) and three different target thicknesses (200 nm, 500 nm, bulk)

have already reached equilibrium. Equilibrium between the two subsystems should not be broken by the heat dissipation after the initial equilibrium without further energy input. Therefore, electron thermal conductivity is set to be a smaller value in the region of thermal equilibrium in our model to maintain the equilibrated state.

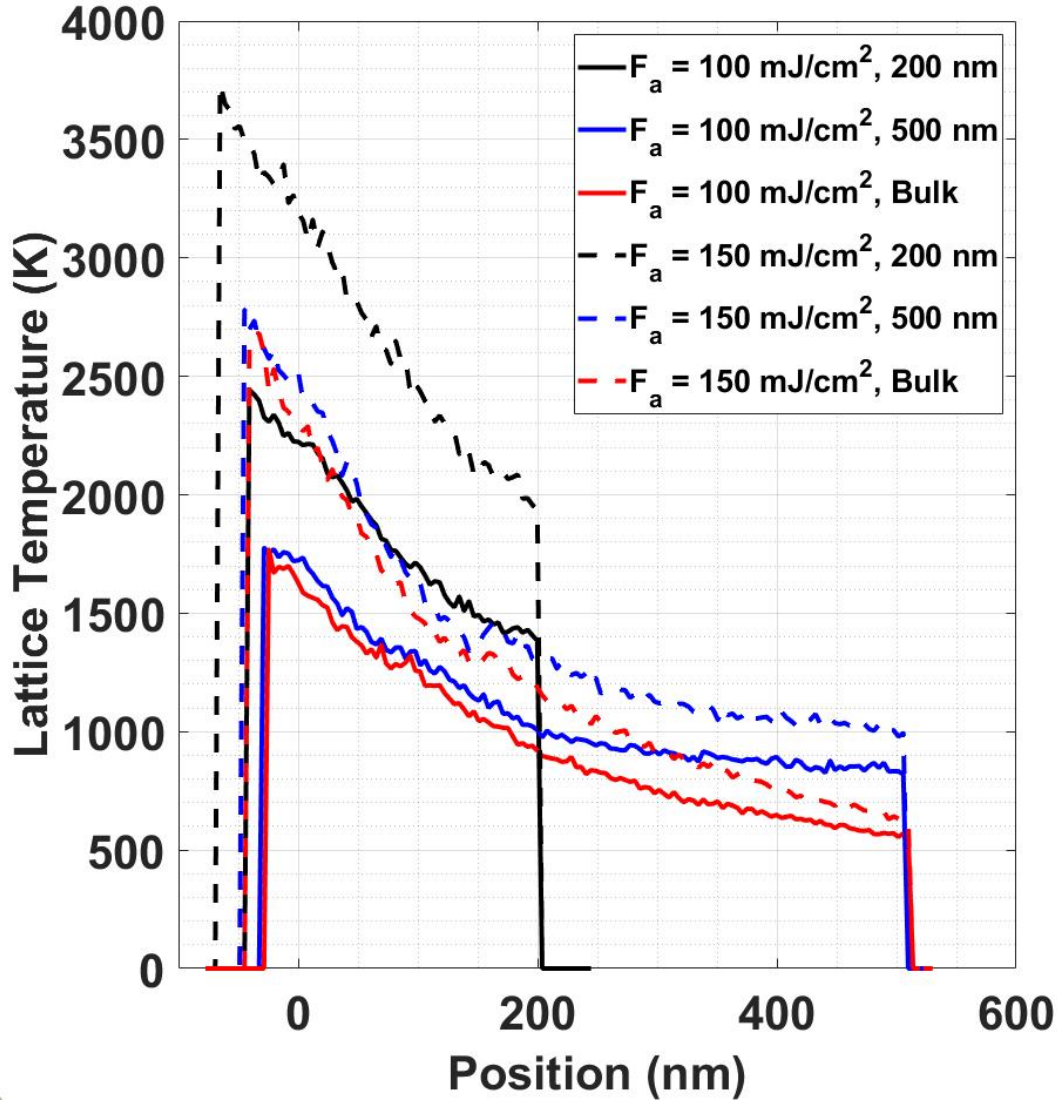


Figure 6.6. Lattice temperatures at 300 ps after laser irradiation for two different absorbed laser fluences (100 mJ/cm^2 and 150 mJ/cm^2) and three different target thicknesses (200 nm, 500 nm, bulk)

In the case of 200 nm target, the shapes of electron temperature profiles change from level lines at 10 ps in Figure 6.4 to tilted lines at 300 ps in Figure 6.6 under both absorbed fluences because the part near to the surface reaches high-temperature equilibrium state earlier by electron phonon coupling which leads to earlier low electron thermal conductivity and less heat dissipation.

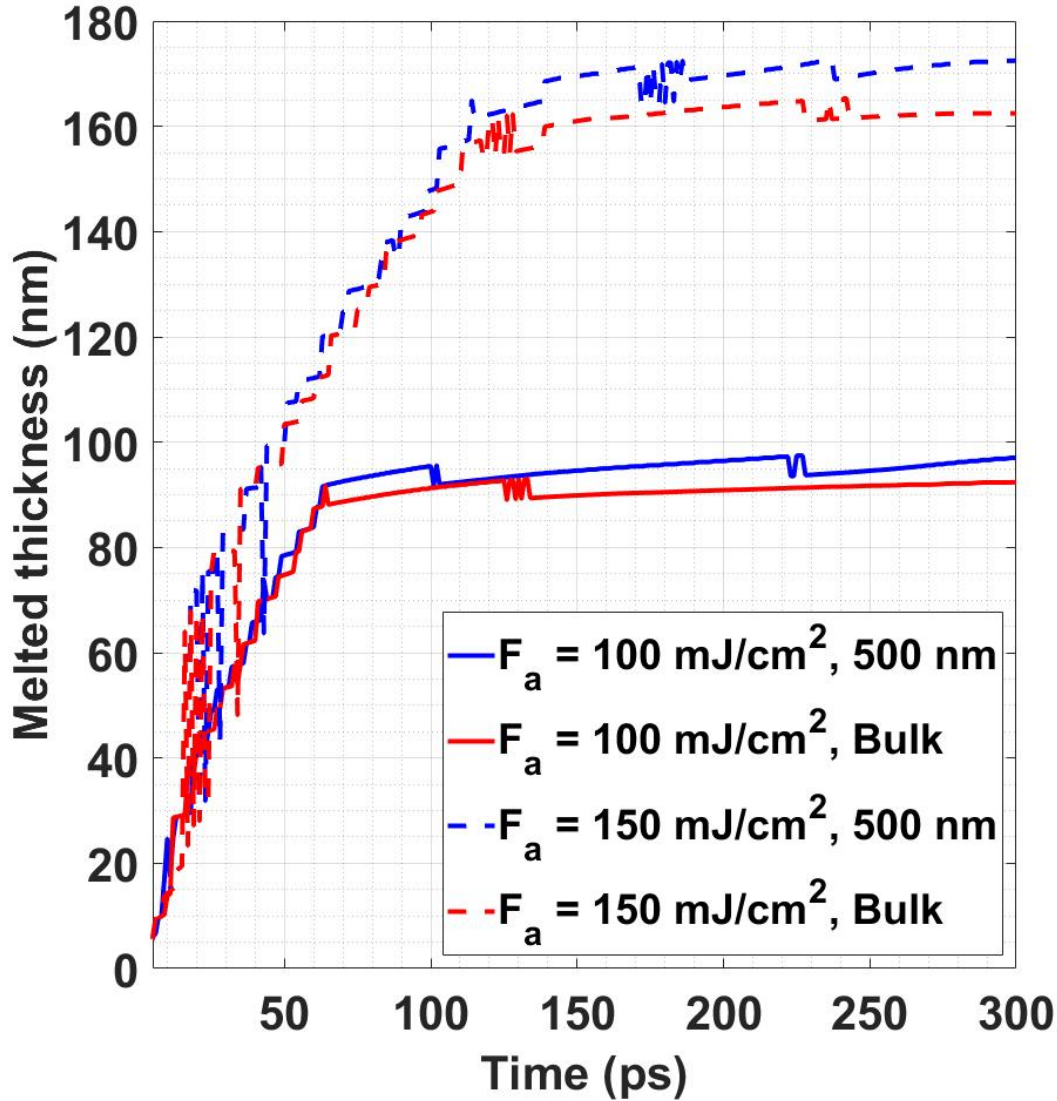


Figure 6.7. Melted thicknesses during the first 300 ps after laser irradiation for two different absorbed laser fluences (100 mJ/cm^2 and 150 mJ/cm^2) and two different target thicknesses (500 nm, bulk)

Layer thickness has small impact on the temperatures in the case of 500 nm and bulk samples, and therefore the melted layers have similar thicknesses, as shown in Figure 6.7. The growth of the melted layer significantly slows down starting at 60 ps and 130 ps for the cases of absorbed fluences 100 mJ/cm^2 and 150 mJ/cm^2 , respectively. After 150 ps, the melted layers become stable, and the thickness now is considered the overall melted thickness

caused by the laser pulse with this absorbed fluence. The simulated melted thicknesses for bulk material are compared with the simulation results given in the work by Starikov and Pisarev [57], as shown in Figure 6.8. Smaller predicted values in our simulation mainly result from the higher electron thermal conductivity.

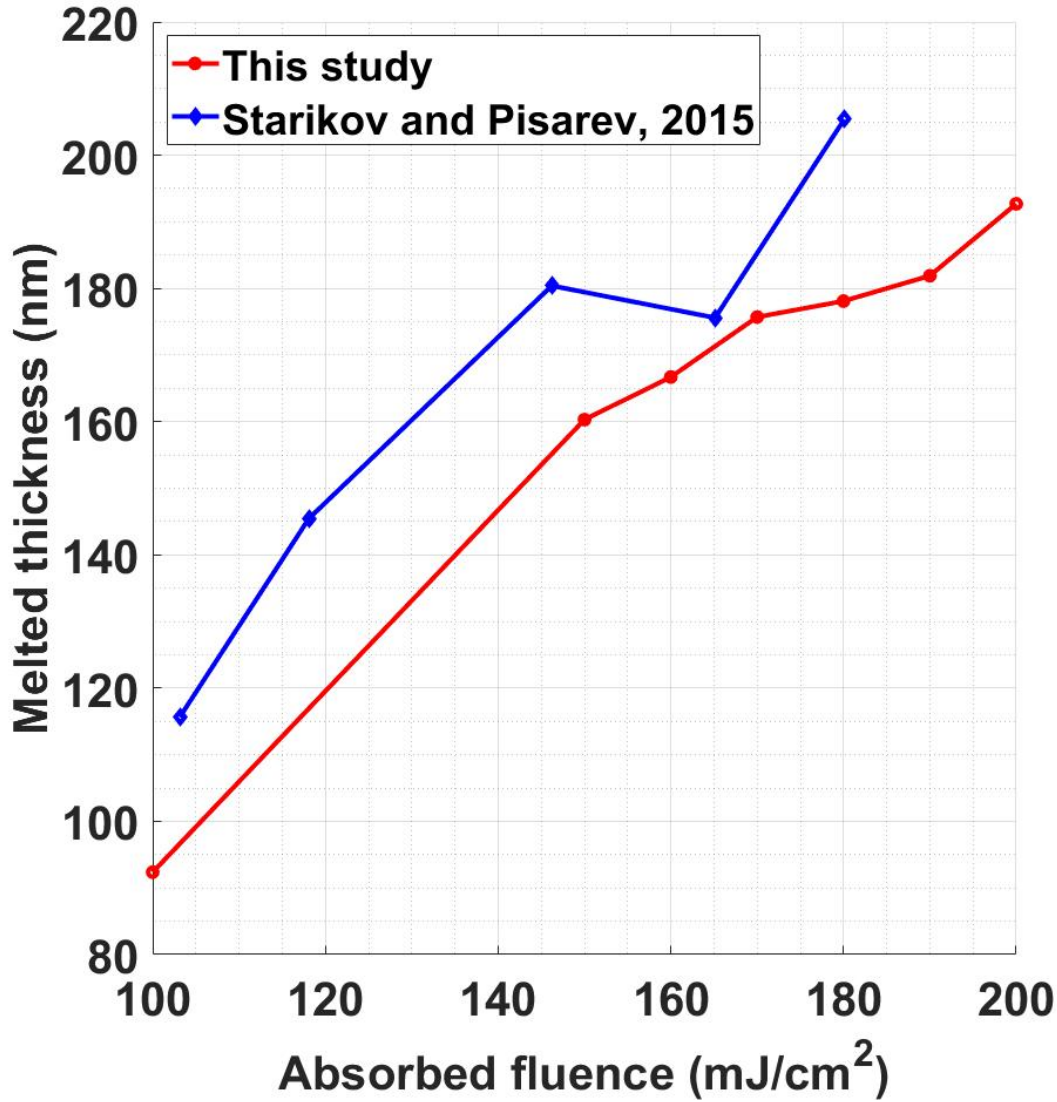


Figure 6.8. Melted thicknesses of gold bulk material for absorbed fluences from 100 mJ/cm² to 200 mJ/cm².

However, in the case of 200 nm, the melting process is notably different. After continuing linearly increasing of the melted layer during the first 80 ps for absorbed fluence 100 mJ/cm²

as shown in Figure 6.9 and the first 10 ps for absorbed fluence 150 mJ/cm^2 , melting occurs in the entire region of the gold layer. This is because the electron-lattice energy transfer rate is similar across the entire area when thermal equilibrium inside the electron subsystem was achieved at early time as shown in Figure 6.4. Consequently, as shown in Figure 6.10, the non-melted layer is superheated and that leads to homogenous nucleation of the liquid phase [81]. The whole 200 nm layer is melted at 110 ps and 90 ps for the cases of absorbed fluences 100 mJ/cm^2 and 150 mJ/cm^2 , respectively. The timing of melting for the whole target material here is based on the observation of the MD snapshots of all atoms.

From the surface movement profiles for absorbed fluence 150 mJ/cm^2 , as shown in Figure 6.11 for 500 nm and bulk and Figure 6.12 for 200 nm, there is an abrupt change of surface velocity at around 75 ps for all gold thicknesses. This is due to the blast force expression used in our simulations and it will be further discussed in the next section.

In the case of 200 nm thin film, because homogeneous melting happens in the entire layer, surface movement has very different behaviors in comparison with thicker targets. As shown in Figure 6.12, for both absorbed laser fluences, the target expands by the melting process during the first 200 ps after laser irradiation but then shrinks and the surface moves backwards. Before 200 ps, the target grows with more intense energy transfer to the lattice subsystem in comparison with the cases of thicker targets. However, the energy is not large enough to fully separate the surface from the target to cause ablation. Then after 200 ps, the interatomic force described by EAM potential in our simulation overcomes the effects of thermal expansion, therefore the material shrinks. At the same time, the target's potential energy converts to its thermal energy which causes the increase in lattice temperature, as shown in Figure 6.13.

6.6 The effects of the electron blast force

As we mentioned before, the Purja Pun's interatomic potential is not suitable due to overestimation of bond strength at high temperatures. The study here is just to analyze the effects of the electron blast force which peaks at the surface as described in equation 2.7.

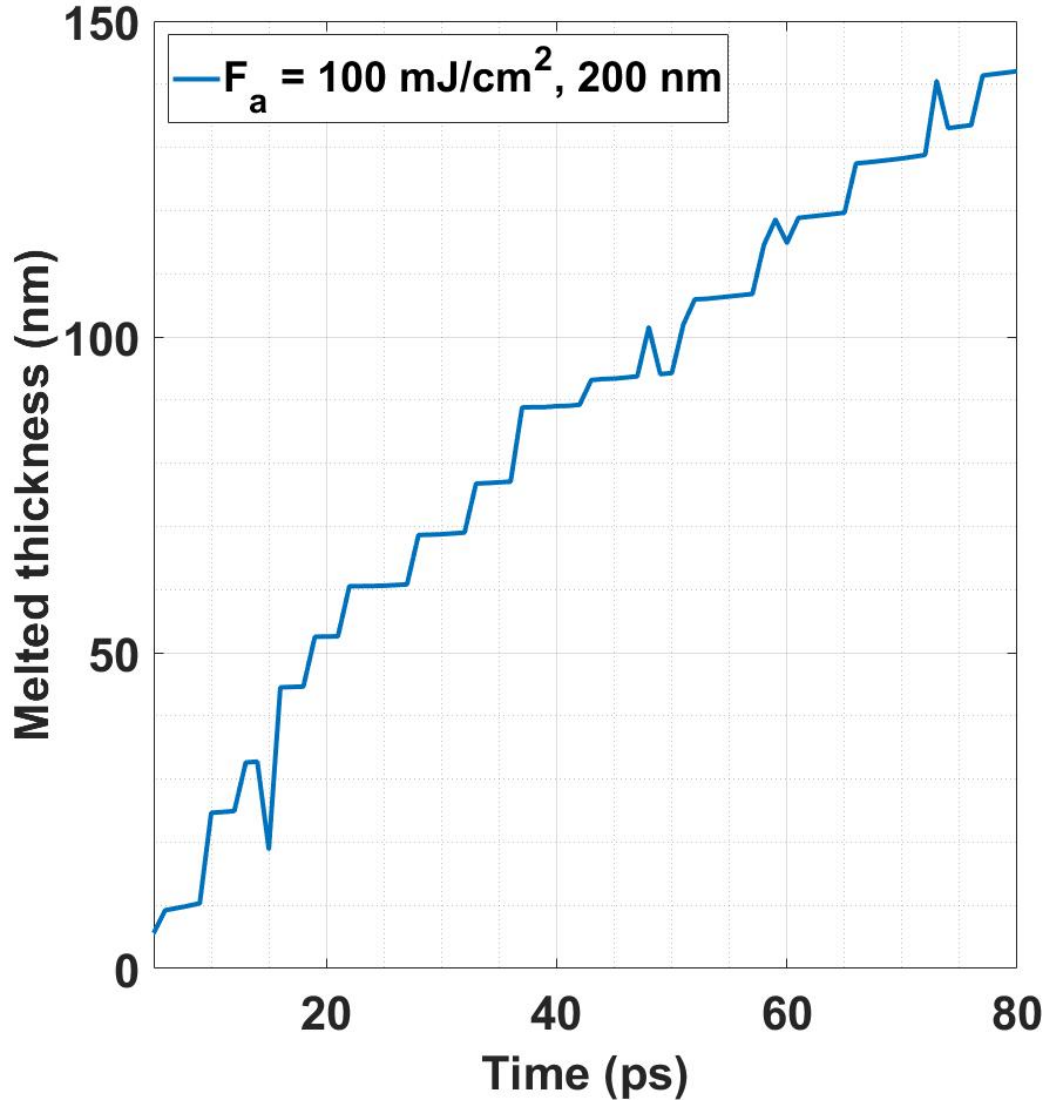


Figure 6.9. Melting profile for 200 nm gold during the first 80 ps with absorbed fluence 100 mJ/cm².

In Figure 6.14, a void area is created due to the velocity difference of the atoms on the two sides of the area. The atoms on the left initially has higher velocity caused by the strong electron blast force from the surface electrons. However, this force is not strong enough to fully separate these atoms from the rest of the target. Later, the left side is slowed down by the drag force while the right side speeds up through thermal expansion and therefore the void shrinks and disappears.

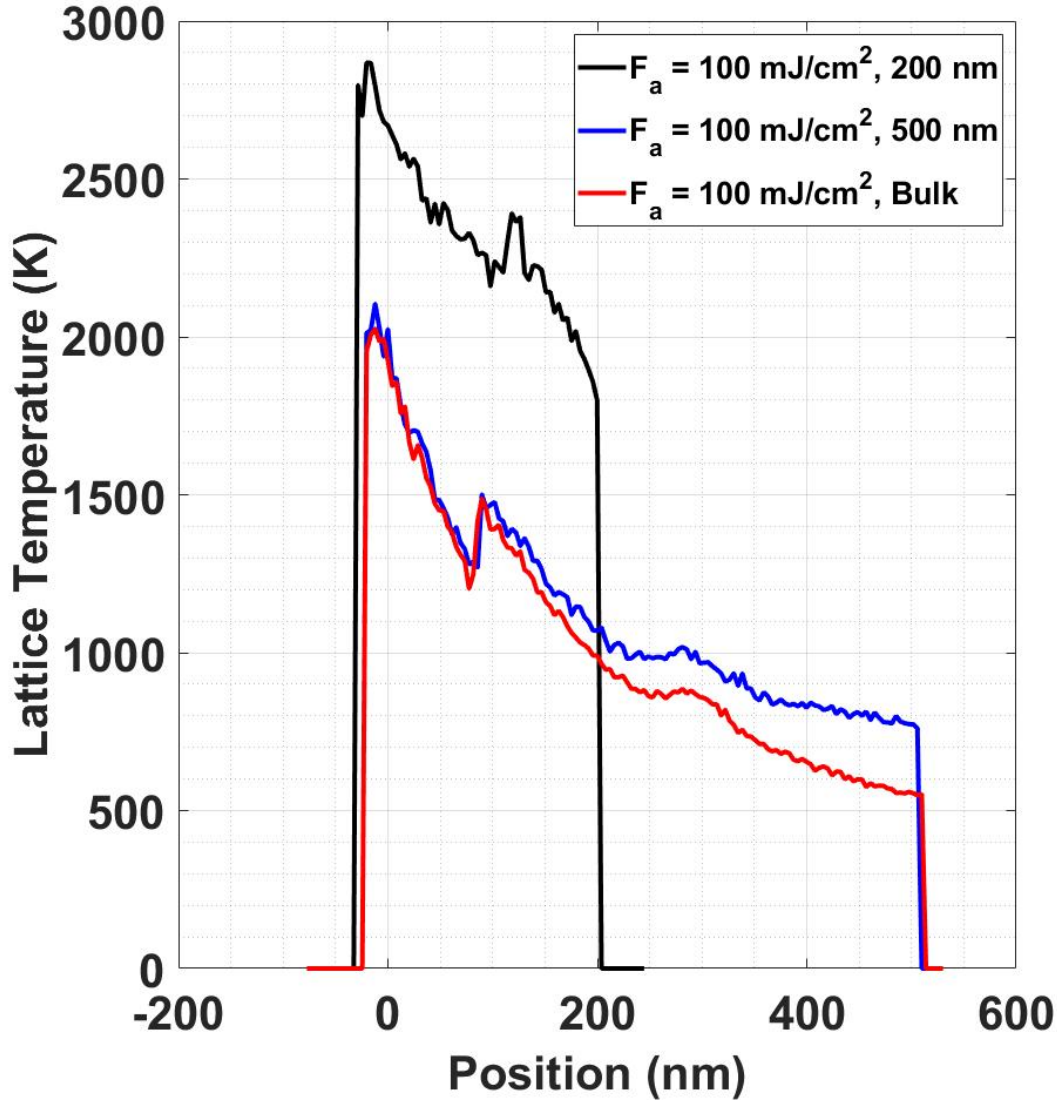


Figure 6.10. Lattice temperatures at 80 ps with 100 mJ/cm² absorbed laser fluence for three different target thicknesses (200 nm, 500 nm, bulk).

However, when the absorbed laser fluence increases, surface ablation occurs as shown in Figure 6.15. This ablation is mainly caused by the blast force of the nonequilibrium surface electrons. Our simulation results show that the ablation does not occur if the blast force is not included. In the paper by Starikov and Pisarev [57], this type of ablation is called the short type. This short ablation is mentioned elsewhere by Norman *et al.* [82] and Chimier *et al.* [83]. The long type, caused by rarefaction wave is not shown in our study, because

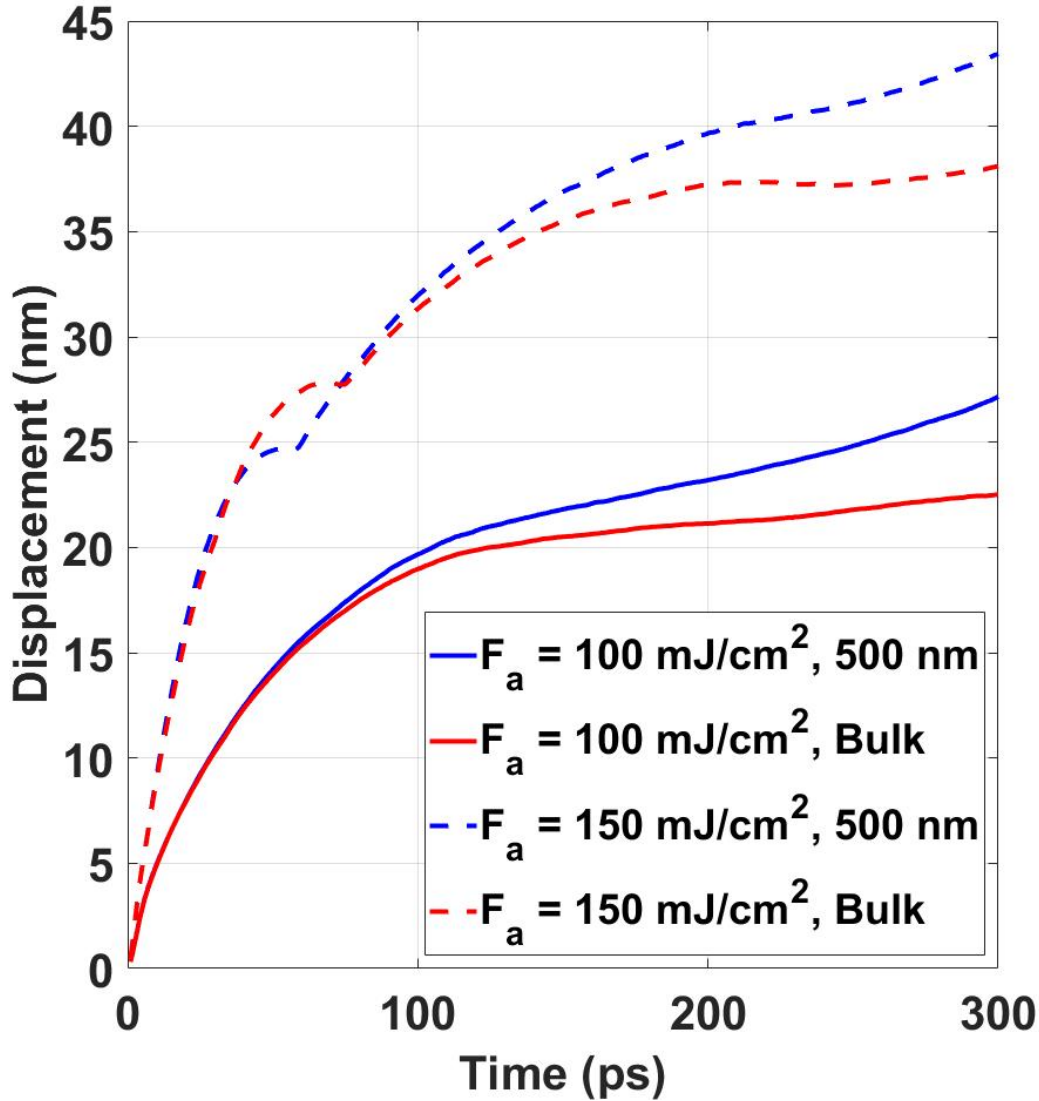


Figure 6.11. Surface movement profiles of gold during the first 300 ps after laser irradiation for two different absorbed laser fluences (100 mJ/cm^2 and 150 mJ/cm^2) and two different target thicknesses (500 nm and bulk)

the interatomic potential is not suitable to predict such ablation mechanism. The absorbed fluence thresholds for the short type of ablation in the cases of 200 nm, 500 nm, and bulk gold are 170 mJ/cm^2 , 160 mJ/cm^2 , and 160 mJ/cm^2 respectively, which are much higher than those predicted by Starikov and Pisarev because of the much higher electron thermal conductivity in our study. The threshold for 200 nm is slightly larger than those in the case

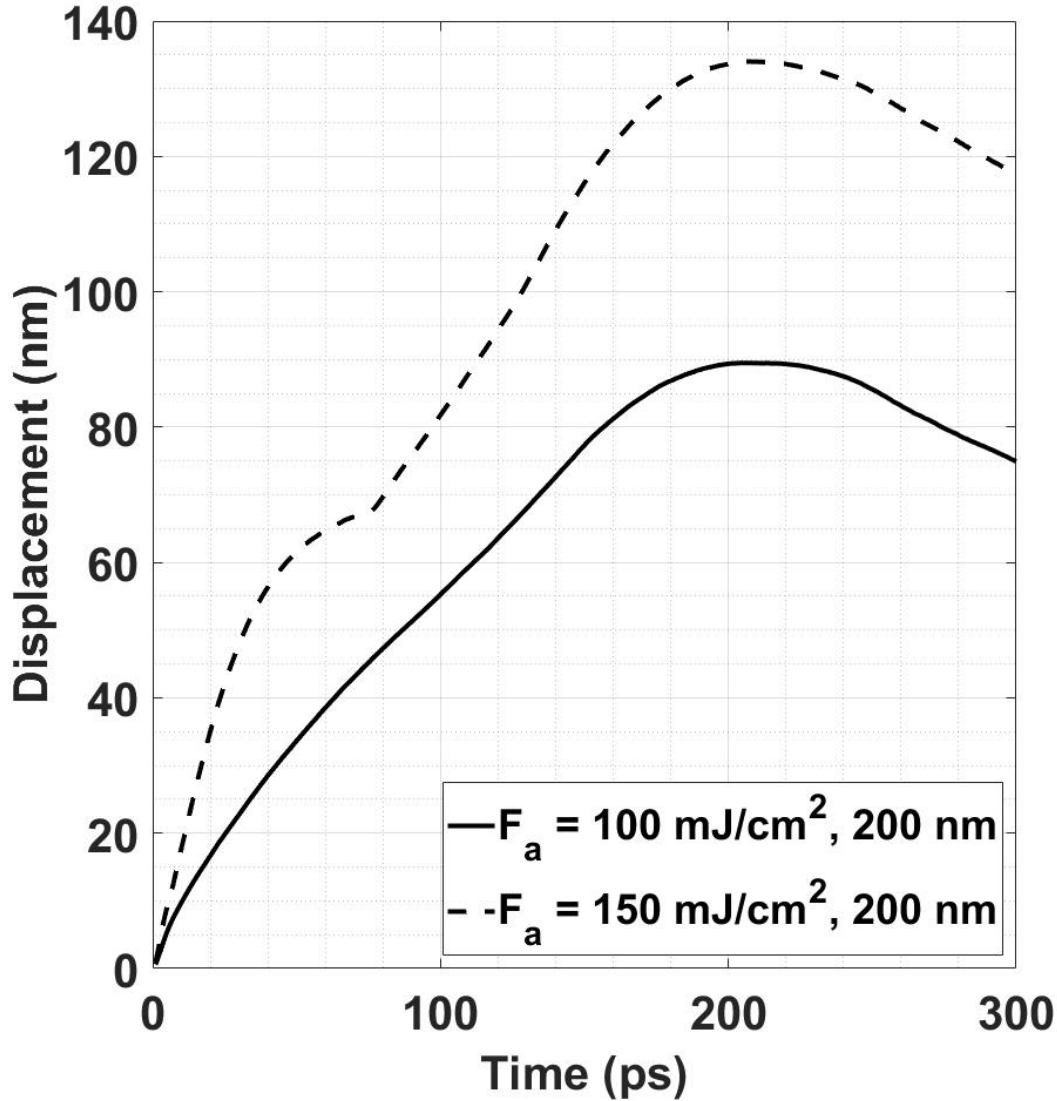


Figure 6.12. Surface movement profiles of 200 nm gold during the first 300 ps after laser irradiation for two different absorbed laser fluences (100 mJ/cm^2 and 150 mJ/cm^2).

of thicker targets because the thermal expansion is faster and the velocity difference of atoms with different depth is smaller, and the potentially ablated part are more difficult to separate from the rest of the material. However, this effect is very small and can be neglected in other studies. At each of their thresholds, the ablated thicknesses are 4.43 nm, 3.42 nm, and 4.00 nm for 200 nm, 500 nm, and bulk gold respectively as shown in Figure 6.15.

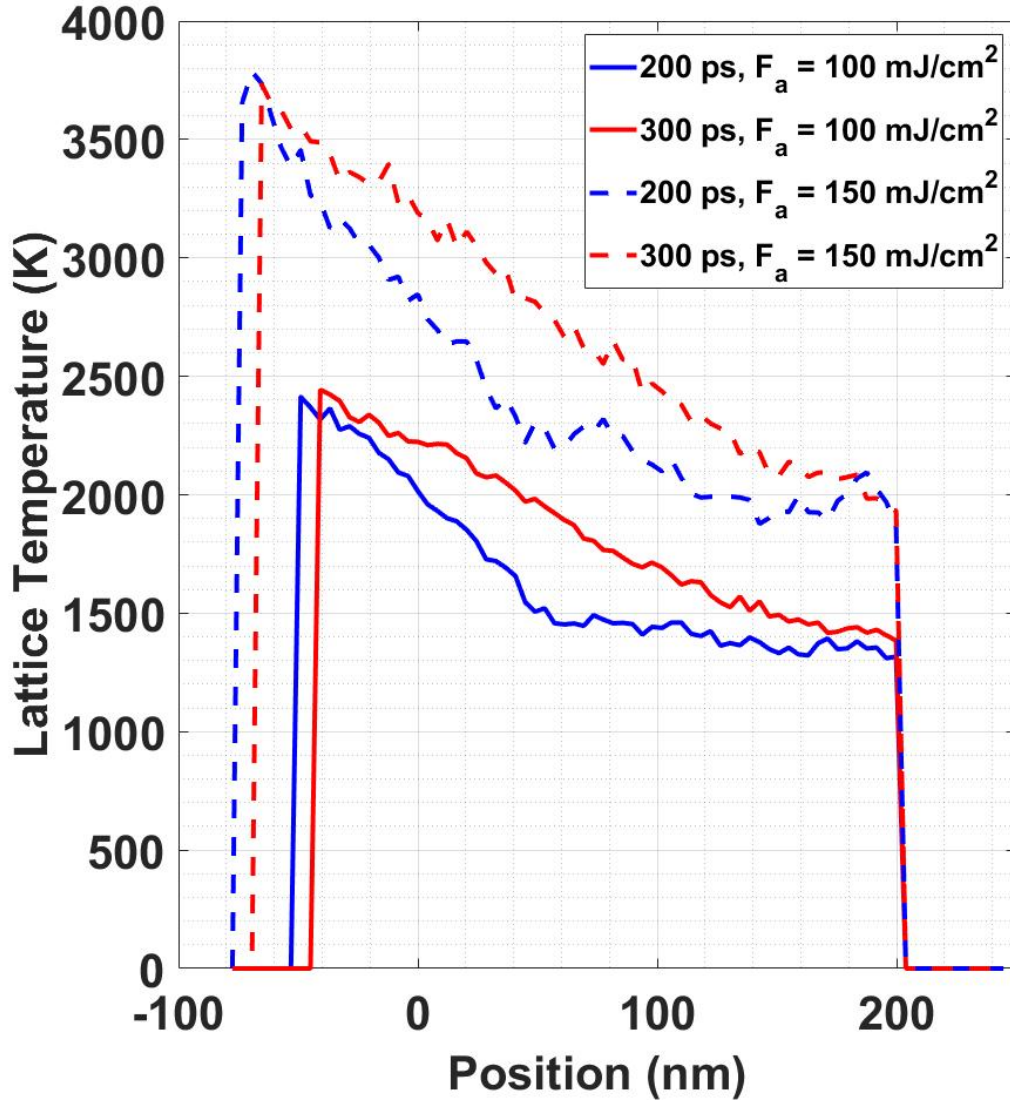


Figure 6.13. Lattice temperatures of 200 nm gold thin film at 200 ps and 300 ps after laser irradiation for two different absorbed laser fluences (100 mJ/cm^2 and 150 mJ/cm^2).

Similar temperatures of nonequilibrium electrons on the surface at early times result in similar ablated thicknesses for the three cases, as shown in Figure 6.16. Small deviations are from the uncertainty caused by the randomness of the void formation.

However, our results and discussions in the next chapter will show the short ablation can be predicted by the nonequilibrium effects of the electron temperature dependent (ETD) in-

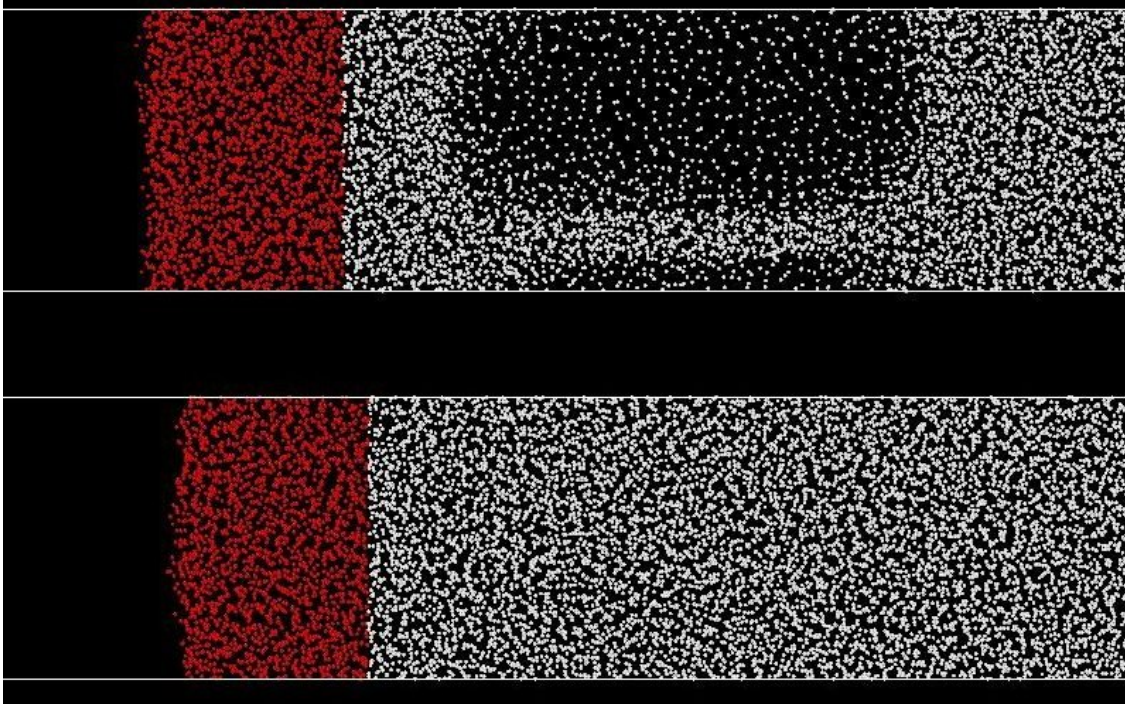


Figure 6.14. Snapshots of the surfaces of 500 nm gold film at 40 ps (top) and 70 ps (bottom). The red regions indicate the 30 nm surface layers. Note that these snapshots are taken at different locations in the simulation box.

teratomic potential developed by Norman *et al.* [43], indicating that the blast force vanished at the surface (equation 2.6) should be used.

6.7 Summary

We benchmarked our hybrid modeling of femtosecond laser interaction with gold target with both experiments and other simulation studies. Our simulation results showed good agreements with the experiments [25] of surface movement of 500 nm gold irradiated by 80 fs laser with fluence 1.3 J/cm^2 and 1.56 J/cm^2 . From the analysis of the absorbed fluence effects, we estimated the total laser reflectivity in the study is between 92% and 94%. We also showed similar results of melted thickness for bulk material with the work by Starikov and Pisarev [57] for the absorbed laser fluence from 100 mJ/cm^2 to 200 mJ/cm^2 .

We also studied the effects of target thickness on material heating and ablation and showed that 500 nm or thicker gold layer have very similar response to the laser pulse below

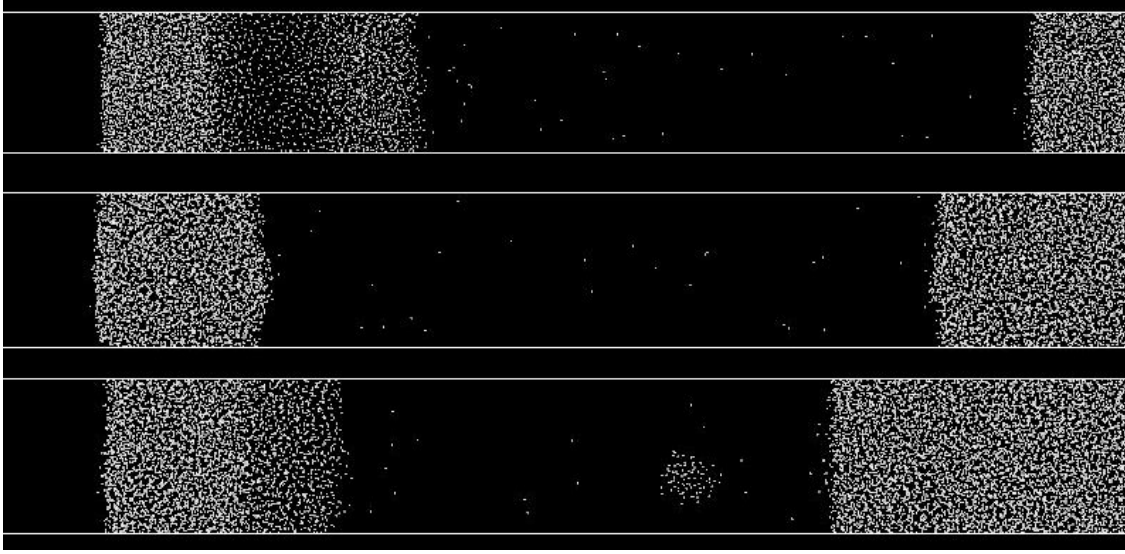


Figure 6.15. Snapshots of the ablated atoms in the cases of 200 nm (top), 500 nm (middle) and bulk (bottom) at their own ablation thresholds (170 mJ/cm², 160 mJ/cm², and 160 mJ/cm², respectively) at 70 ps. Note that these snapshots are taken at different locations in the simulation box.

the ablation threshold, especially on the surface. However, thinner layers, for example 200 nm target, showed different tendency in material expansion. The electron subsystem reaches thermal equilibrium in the entire target before lattice-electron equilibrium and that causes melting simultaneously in a large area of the material with absorbed fluence 100 mJ/cm² and above.

Lastly, we showed the effects of nonequilibrium electron blast force on void formation and even short ablation in the surface area. This type of ablation happens at very early time and greatly depends on the electron temperature on the surface. Therefore it is not affected by the thickness of the target but greatly influenced by the electron thermal conductivity. The ablated thickness for gold was calculated around 4 nm at the threshold around 160 mJ/cm² of the absorbed laser fluence.

However, our further studies indicated that the blast force should vanish at the surface and, therefore, is not responsible for the short ablation. The short ablation could be instead caused by the nonequilibrium electron effect (electronic pressure by localized electrons) in-

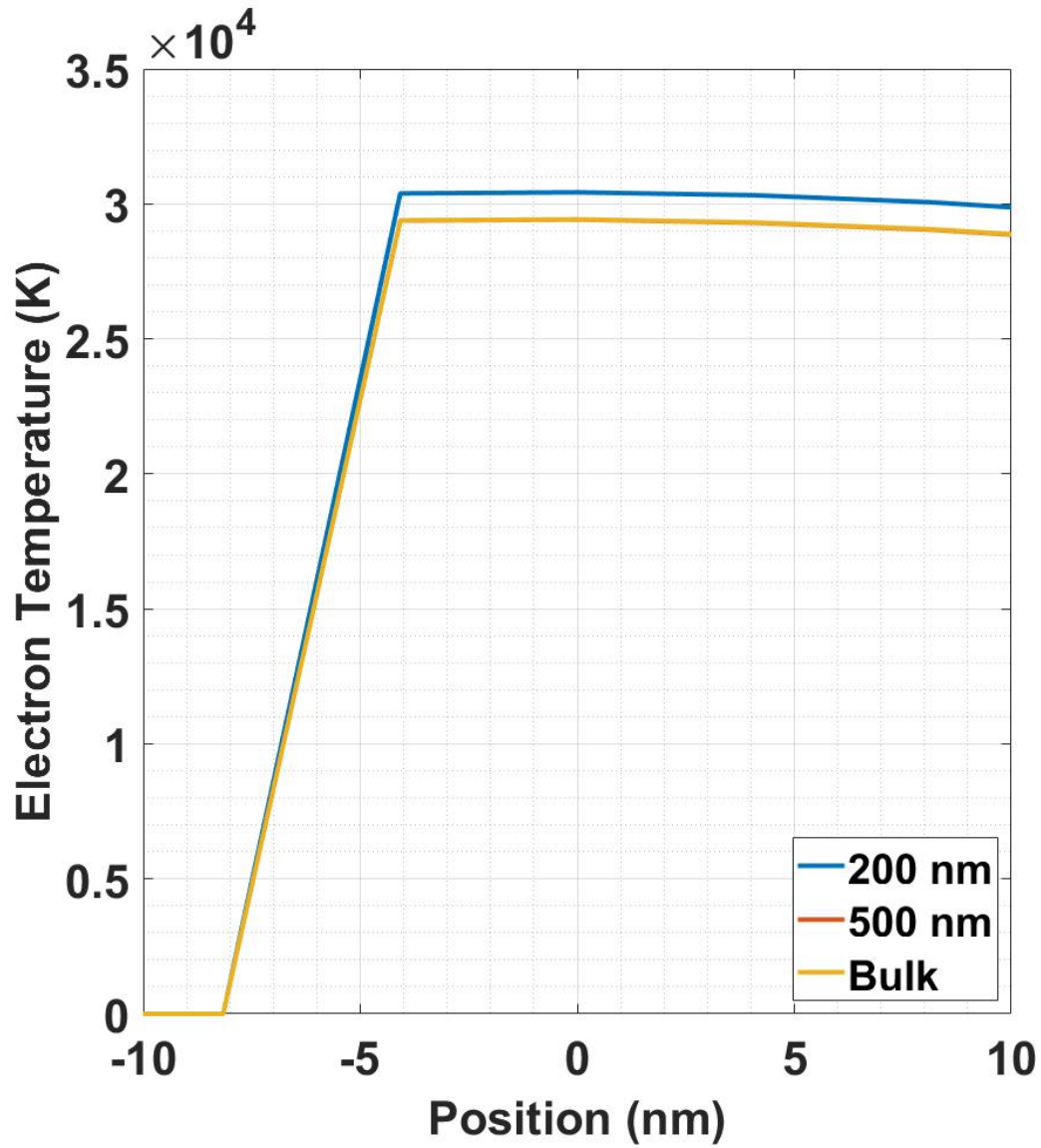


Figure 6.16. Electron temperatures on the surface at 1 ps in the cases of 200 nm, 500 nm and bulk at their own ablation thresholds (170 mJ/cm², 160 mJ/cm², and 160 mJ/cm² respectively). The profiles of 500 nm and bulk overlap in the graph.

cluded in the electron temperature dependent (ETD) interatomic potential as described in the next chapter.

7. SINGLE PULSE ABLATION STUDY

7.1 Introduction

In this chapter, we studied the effects of electronic pressure by localized electrons using the electron temperature dependent (ETD) interatomic potential. Melting and ablation studies over a wide range of absorbed laser fluences, 40-150 mJ/cm², were performed.

We showed two ablation regimes as a function of laser fluence and three ablation mechanisms including nonthermal ablation by electronic pressure, spallation by thermal stress, and phase explosion. The electronic pressure induced by the ETD potential can cause ablation of thin layers in the low fluence regime. The onset of spallation is responsible for the increase of ablation growth rate with laser fluence. However, the appearance of phase explosion/explosive boiling does not produce significant effects on the ablation depth. This mechanism suppresses the effects of electronic pressure at higher laser fluences and ablates the target surface into single atoms and small clusters.

Our results agreed well with the experiments on ablation depth and velocities of ablated matter in the high ablation regime. The ETD potential continuously updated in accordance with electron temperature allows production of both the U shape profile of plume atomization degree and better ablation depth profiles in low and intermediate fluence regimes as shown in the experiments.

This section is reprinted from Yuan and Sizyuk (2021) Ablation study in gold irradiated by single femtosecond laser pulse with electron temperature dependent interatomic potential and electron–phonon coupling factor. *Laser Physics*, **31**(3), 036002. [45]. "© Astro Ltd. Reproduced with permission. All rights reserved".

7.2 Simulation setup

For the simulated cases, the target material gold is initially at room temperature (300 K). The MD simulation box with a lateral area of 12.2 nm × 12.2 nm and a thickness of 407.8 nm has periodic boundary conditions in the directions perpendicular to the incident laser, and a fixed boundary condition in the laser incident direction. With the same lateral

size, the target is 203.9 nm thick in the MD part and 1800.0 nm thick in the TTM part. The cell sizes for lattice and electron temperatures are $4.1 \times 4.1 \times 4.1 \text{ nm}^3$ and $4.1 \times 4.1 \times 10.0 \text{ nm}^3$ in the MD and TTM parts, respectively. There are approximately 1.8 million atoms in the MD simulation. The laser pulse is 100 fs with a Gaussian shape. The timestep in MD is 1 fs. Laser penetration depth is 10 nm and absorbed laser fluence is considered. The electron blast force vanishes at the surface as described in equation 2.6.

The electron heat capacity (C_e) and electron-phonon coupling factor (G) are adopted from Lin's data [22], the electron thermal conductivity (K_e) is calculated by the expression developed by Anisimov and Rethfeld [24] as described in previous chapter. The electron temperature dependent (ETD) interatomic potential for gold [43] is used and two potentials, 1T and 5T, are derived from it.

7.3 Melting study with ETD interatomic potential

We studied material melting using two different values of electron-phonon coupling factor G to compare with the results in Starikov and Pisarev's work [57]. One is a function of electron temperature from Lin's data [22] and the other is a constant value, $3.0 \times 10^{16} \text{ Wm}^{-3}\text{K}^{-1}$. We performed our simulations using both the 5T and the 1T potentials with both sets of electron-phonon coupling factor G and found that melting and maximum electron temperature profiles are not sensitive to the potentials used in our simulations (difference is lower than 1%), so only results with the 1T potential are shown in Figure 7.1. Note that the potential used in the 1T simulations is the same as the one in Starikov and Pisarev's work [57], but the blast force and the lattice temperature are defined differently.

The melting thickness profiles of gold and maximum electron temperature are shown in Figure 7.1 for various absorbed fluences from 40 mJ/cm² to 150 mJ/cm². Comparison of results obtained with different G factors shows that the simulations with constant G value underestimate melting thickness in low fluence regime, because of the underestimation of the coupling effect. These simulations also overestimate melting thickness in high fluence regime due to thicker heat-affected zones by slower electron-lattice relaxation.

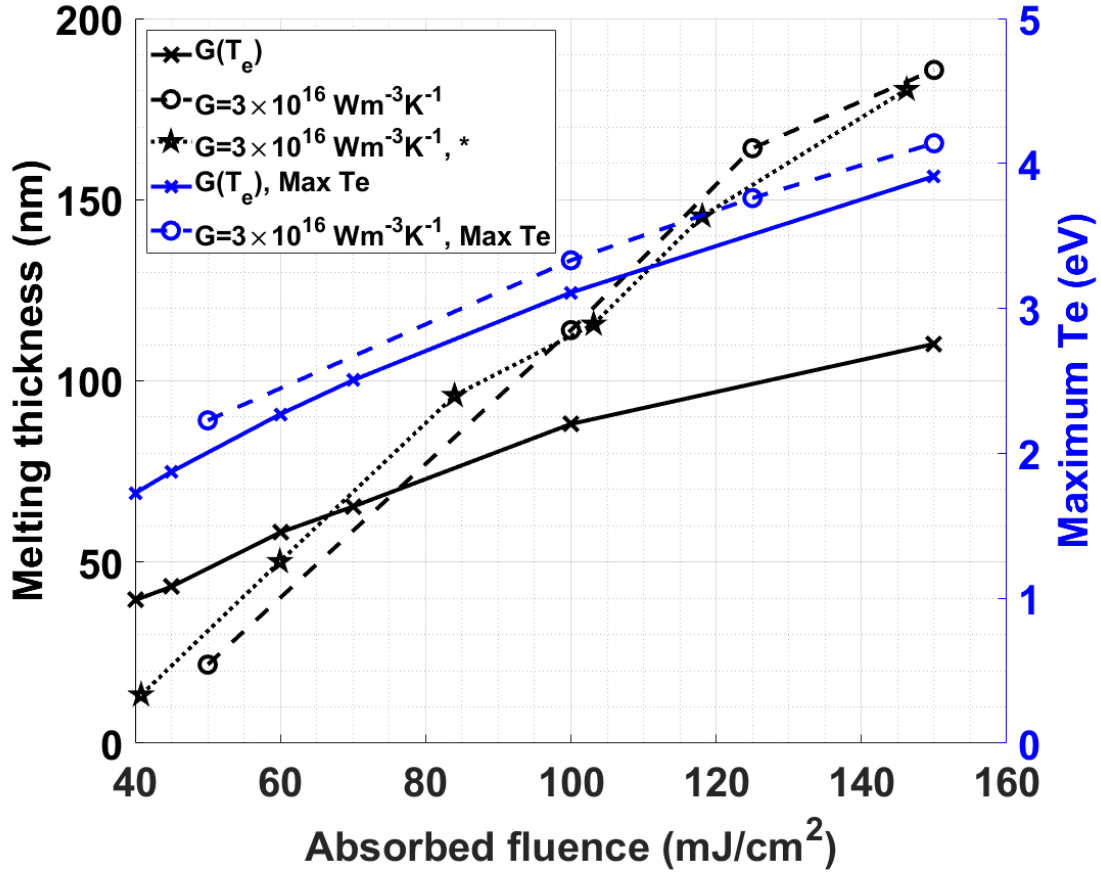


Figure 7.1. Melting thicknesses and maximum electron temperature for different absorbed fluences in gold: (*) is the data from Starikov and Pisarev's results [57]. The 1T potential was used in these simulations. The lines are drawn to guide the eye.

7.4 Energy conservation with the 5T potential

Since the 5T potential will change the energy in the lattice subsystem without considering the corresponding energy change in the electron subsystem, the total energy of the system will not be conserved. However, with Lin's G , this nonconservation is negligible. During the first 10 ps, when potential change only occurs and the coupling between subsystems is significant, the energy gain due to the 5T potential with changing electron temperature (also the energy change of the whole system) is no more than 2.2% of the energy gain from lattice-electron coupling. While using the constant G ($3.0 \times 10^{16} \text{ Wm}^{-3}\text{K}^{-1}$), due to its

small value, the energy change from the 5T potential is much more substantial compared to the lattice-electron coupling, and this results in a value of more than 10% in the same comparison. Therefore, it is necessary to study the effects of the 5T potential with an electron temperature dependent G in terms of energy conservation.

7.5 Comparison of the 5T and the 1T potentials

Figure 7.2 shows the density profiles after laser irradiation at the absorbed fluence 45 mJ/cm^2 for both the 5T and the 1T potentials. In the case of the 5T potential, a thinner layer of 10 nm was fully ablated, and a void of 10 nm diameter was formed and stabilized in the subsurface of the target. However, a thicker layer of 18 nm was ablated in the simulation of the 1T potential. To exclude the effects of the electron blast force on fast ablation, we performed other simulations with the 5T potential without taking into account the electron blast force, and similar ablation phenomena were observed.

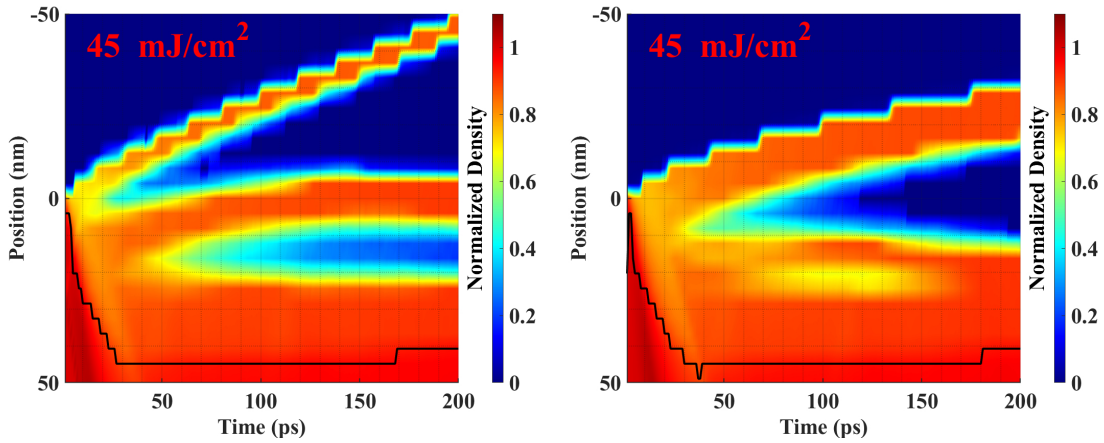


Figure 7.2. Colormaps of target normalized density in gold at the absorbed fluence 45 mJ/cm^2 . Left – the 5T potential; right – the 1T potential.

As shown in Figure 7.3, the target surface responses to a single 45 mJ/cm^2 laser pulse are very different between the 5T and the 1T potentials. In the lattice temperature distribution shown in Figure 7.3(a), there is a heat center on the expanding surface at around 8 ps in the case of the 5T potential, which is not seen in the case of the 1T potential. The process of surface expansion corresponds to the transformation of potential energy into kinetic energy

due to larger lattice parameters/constants in equilibrium at higher electron temperatures according to the 5T potential. It was mentioned by Daraszewicz [78] that with higher electron temperature, the equilibrium lattice parameter becomes larger which causes bond softening on the surface where the target can expand freely under electronic pressure. This electronic pressure is caused by the localized electrons and these effects are implicitly expressed by the 5T potential [43], [51]. Note that the 5T potential is a discrete function of electron temperature in our simulations, and with a more accurate ETD potential which continuously changed with electron temperature, the surface could be ablated in the form of individual atoms.

In Figure 7.3(b), simulations with the 5T potential showed strong compressive stress caused by electronic pressure occurring in the subsurface area before 3 ps after laser irradiation. Consequently, this strong compressive stress is followed by a strong unloading tensile stress at around 8 ps, as shown in Figure 7.3(c). This tensile stress is responsible for the ablation of the thin liquid layer in the case of the 5T potential illustrated in Figure 7.2. In the case of the 1T potential, the compressive stress wave (Figure 7.3(b)) induced by the rapid heating of lattice under a nearly constant volume condition leads to the ablation as shown in Figure 7.2. The simulations with the 1T potential predict that photomechanical cavitation due to rapid lattice heating, called spallation, is responsible for the ablation at low laser fluence. Comparison of above results shows that in the case of the 5T potential, the electronic nonthermal ablation removes hot thin layers, suppressing spallation under low fluences.

7.6 Ablation mechanisms

To compare with experimental results, we converted the laser fluences in the experiments into absorbed fluences by utilizing the absorptance measured by Vorobyev and Guo [28]. Figure 7.4 shows the ablation depth profile with respect to various absorbed laser fluences. Two ablation regimes are seen because of the effects of electronic pressure in the case of the 5T potential. Predicted in our simulations, the transition fluence between two regimes is around 60 mJ/cm^2 , which agrees well with the experimental results from works by Noël *et*

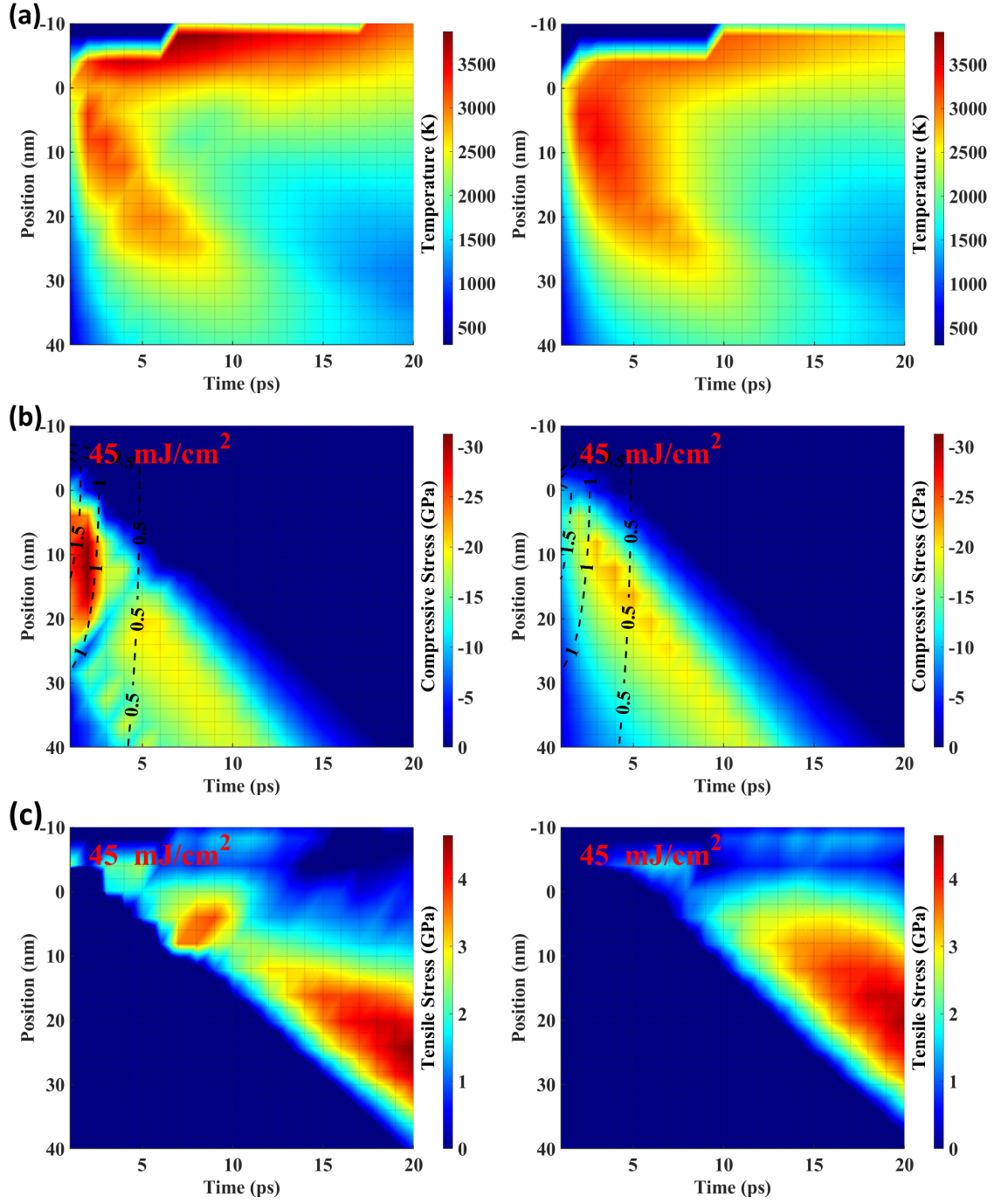


Figure 7.3. Colormaps of target surface properties within 20 ps after 45 mJ/cm² laser irradiation with the 5T potential (Left) and the 1T potential (Right). These properties are lattice temperature (a), compressive stress (b), and tensile stress (c). The black dashed lines in (b) indicate the electron temperature in eV.

al. [12] and Hermann *et al.* [29]. However, even with the 5T potential, we overestimated the ablation threshold and the ablation thickness at low absorbed fluences in comparison with the experimental results. The discrepancy results from the discrete nature of the 5T potential. In reality, an interatomic potential, continuously changed with electron temperature, would have a greater effect on the surface and be able to cause single atoms and thin layers to be ablated in lower fluence regimes. The energy removal from the surface by these single atoms and thin layers ablated by electronic pressure will subdue the effects of thermal pressure as indicated in Figure 7.2. Therefore, with an interatomic potential continuously changed with electron temperature, one can predict a lower ablation threshold and shallower ablation depth caused by spallation in the intermediate fluence regime, and the results will agree very well with the experimental data. Figure 7.5 shows the ablation process by target density colormaps with different absorbed fluences in simulations with the 5T potential.

With the fluence higher than 120 mJ/cm^2 , our simulation results with both the 5T and the 1T potentials agree well with the experiments. At these fluences, the effects of electronic pressure caused by the 5T potential are dominated by the rapid thermal expansion due to phase change. The diminishment of the tensile stresses caused by electronic pressure is shown in Figure 7.6, suggesting the ablation of single atoms and small amorphous clusters from the surface is now due to explosive boiling/phase explosion.

Note that our prediction of the physical processes is based mainly on the change of ablation depth with different absorbed laser fluences. The previous papers [12], [29] did not include confidence intervals and the 5T potential is an approximation of the continuous function of electron temperature. Therefore, it might be not accurate to compare the exact ablation depth when its value is already small (tens of nm).

Experimental results [12], [29] also showed a large ratio of atomized ablated matter to overall ablated material at low fluences that can be explained by the electronic pressure caused by the ETD potential. The sudden decrease of the atomization degree of the ablated matter with increasing fluence is due to the onset of ablation by spallation and the slow increase in high fluence regime results from the production of single atoms or small clusters through phase explosion.

With the absorbed fluence of 150 mJ/cm^2 , we can roughly divide the ablated matter into two groups, one close to the surface is ablated by phase explosion and the other one is ablated by spallation appearing as gold layers. Comparison with the velocity of ablated matter measured in experiments [12] showed that our highest velocity of ablated single atoms or small clusters by phase explosion is on the same order of 10^3 m/s and the slowest velocity of ablated layer by spallation is about 100 m/s matching with the nanoparticle velocity (around 100 m/s) in the experiments.

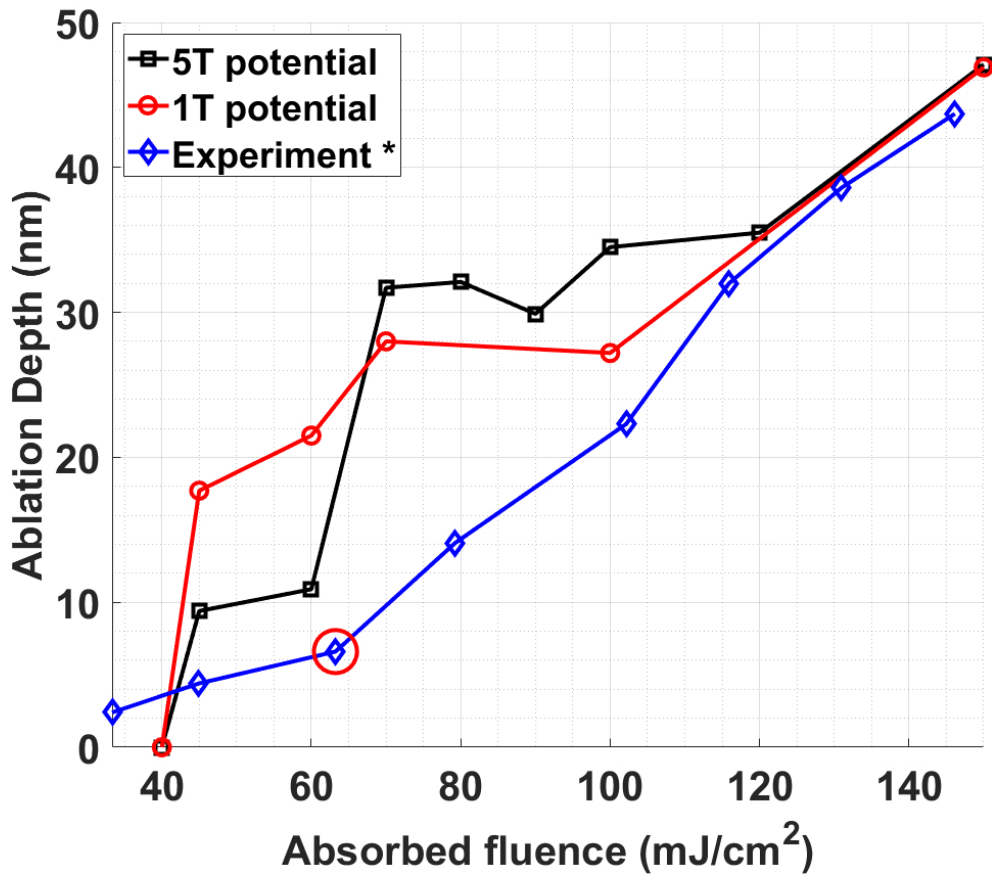


Figure 7.4. Ablation depth for different absorbed fluences in gold: (*) is the data measured by Hermann *et al.* [29] with absorptance from work by Vorobyev and Guo [28]. The circled point indicates the transition of the two ablation regimes. The lines are drawn to guide the eye.

We also briefly performed the same study with electron thermal conductivity taken from work by Petrov *et al.* [23] which is much larger than the one mainly used in this chapter.

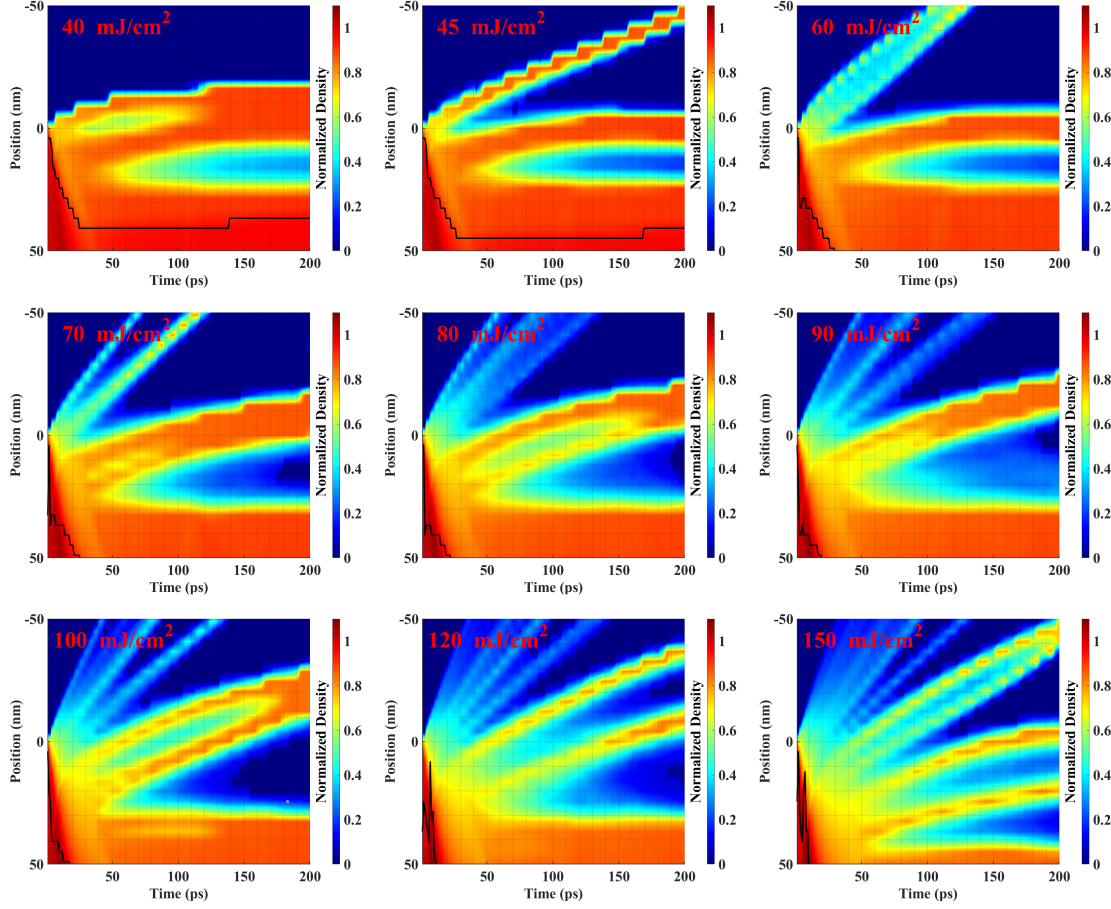


Figure 7.5. Colormaps of target density in gold at absorbed fluences from 40 mJ/cm^2 to 150 mJ/cm^2 with the 5T potential. The black lines indicate the solid-liquid interface.

No ablation is seen even with absorbed fluence up to 150 mJ/cm^2 . The potential reasons for this might be the discontinuity of the 5T potential or the overestimation of the electron thermal conductivity by Petrov *et al.*.

7.7 Summary

We studied melting and ablation dynamics in gold irradiated by a femtosecond laser based on our hybrid MD-TTM simulations with the 5T potential and temperature dependent electron-phonon coupling factor G . It was found that the overall melting thickness is not affected by the nonthermal effects from the 5T potential with the studied absorbed fluence

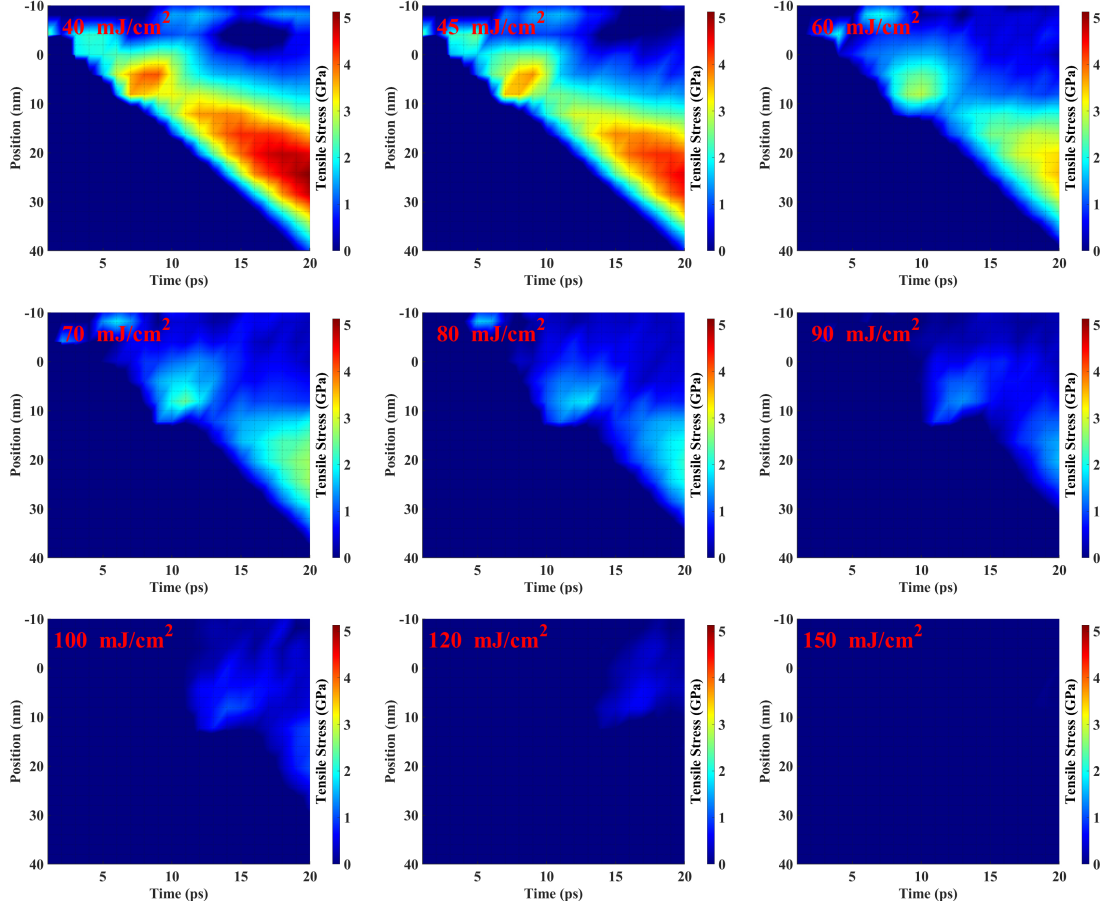


Figure 7.6. Colormaps of target tensile stress in gold within 20 ps after laser irradiation at absorbed fluences from 40 mJ/cm² to 150 mJ/cm² with the 5T potential.

(40 mJ/cm² - 150 mJ/cm²), but it is very sensitive to the electron-phonon coupling factor G used in the simulations. Two ablation regimes in accordance with laser fluence were predicted in our simulations in the case of the 5T potential.

Three different ablation mechanisms, namely nonthermal ablation caused by electronic pressure, spallation caused by thermal pressure, and phase explosion, were observed at different absorbed fluences. We also pointed out that continuously changing ETD potential with respect to electron temperature can cause direct ablation of surface atoms by high electronic pressure. In the low fluence regime, ablation is mainly caused by electronic pressure from localized electrons implicitly described by the ETD potential. While in the intermediate fluence regime, spallation from the nucleation and growth of void in the subsurface layer

caused by thermal stress occurs and leads to the ablation of thick layers. The onset of this spallation is the transition point between the two commonly recognized ablation regimes. In the high fluence regime, phase explosion/explosive boiling starts to take over the effects of electronic pressure and becomes the dominant ablation mechanism for the surface atoms. Single atoms and small clusters are ablated by phase explosion in the high fluence regime.

Although we correctly predicted the ablation thickness and the velocities of ablated matter in the high fluence regime with experiments by Noël *et al.* [12] and Hermann *et al.* [29], a more accurate ablation picture for lower fluences could be obtained with the implementation of more accurate ETD potential, continuously changed with electron temperature. Then, the U shape profile of the plume atomization degree with respect to laser fluence found in the experiments can be better explained.

8. DUAL PULSE ABLATION STUDY

8.1 Introduction

In this chapter, we studied the effects of delay time of double laser pulses on ablation process with both low and high absorbed fluences. Very different phenomena are observed for the two absorbed fluences. With low absorbed fluence, longer delay time reduces the effects of nonthermal ablation and has an optimal value for spallation. While with high absorbed fluence, spallation becomes weaker and phase explosion becomes stronger with increasing delay time.

8.2 Simulation setup

For the simulated cases, the target material gold is initially at room temperature (300 K). The MD simulation box with a lateral area of $12.2 \text{ nm} \times 12.2 \text{ nm}$ and a thickness of 407.8 nm has periodic boundary conditions in the directions perpendicular to the incident laser, and a fixed boundary condition in the laser incident direction. With the same lateral size, the target is 203.9 nm thick in the MD part and 1800.0 nm thick in the TTM part. The cell sizes for lattice and electron temperatures are $4.1 \times 4.1 \times 4.1 \text{ nm}^3$ and $4.1 \times 4.1 \times 10.0 \text{ nm}^3$ in the MD and TTM parts, respectively. There are approximately 1.8 million atoms in the MD simulation. The laser pulse is 100 fs with a Gaussian shape. The timestep in MD is 1 fs. Laser penetration depth is 10 nm and absorbed laser fluence is considered. The electron blast force vanishes at the surface as described in equation 2.6.

The electron heat capacity (C_e) and electron-phonon coupling factor (G) are adopted from Lin's data [22], the electron thermal conductivity (K_e) is calculated by the expression developed by Anisimov and Rethfeld [24]. The electron temperature dependent (ETD) interatomic potential for gold [43], also called the 5T potential, is used.

For the cases of double pulse irradiation, the two pulses are the same in pulse shape and pulse duration with the single pulse. The intensities of the two individual pulses are the same. For convenience, we considered the experiments using double pulses with 0 ps delay

time are the same as the experiments using a single pulse of double intensity. Therefore, the overall absorbed fluences of those two cases are the same.

8.3 Low overall absorbed fluence

We first studied double pulse each of absorbed fluences 25 mJ/cm^2 with different delay times. The overall absorbed fluence is 50 mJ/cm^2 . From previous study in the last chapter [45], with this absorbed fluence, only nonthermal ablation caused by electronic pressure implicitly described by the 5T potential occurs. Therefore, only a very thin surface layer is ablated by a single pulse. However, as shown in Figure 8.1, delay time will greatly alter the ablation process while it does not have much effect on the overall melting depth. With increasing delay time from 0 ps to 50 ps, the ablation mechanism changes from nonthermal ablation in the case without delaying to spallation when delay time is 10 ps; and no ablation was observed with delay time longer than 20 ps. Nonthermal ablation of thin layers and spallation are both ablation mechanisms of liquid layers. They require the tensile stress at the ablation point to be greater than 3.5 GPa (4 GPa predicted by Schäfer *et al.* [40]), and fast surface expansion. The surface expansion in nonthermal ablation is mainly due to the interatomic force from the changing of interatomic potential caused by the rapidly increasing electron temperature. While the surface expansion in spallation is due to melting and thermal expansion of liquid material caused by rapid heating of the lattice.

The decreasing of electronic effects from the ETD potential causes the transition from nonthermal ablation, corresponding to delay time up to 5 ps in Figure 8.1, to spallation in the case of 10 ps delay time. The electronic effects are reflected by the compressive stress and the electron temperature, as shown in Figure 8.2. Stronger compressive wave, higher electron temperature, and closer hot electron centers represent stronger electronic effects.

Figure 8.3 shows the lattice temperature and surface movement during the first 50 ps after first laser pulse irradiation. Comparison of the cases with delay times of 10 ps and 20 ps shows the surface temperature is higher, and the surface expands faster in the case of 10 ps. This difference is the reason for the transition from spallation to no ablation.

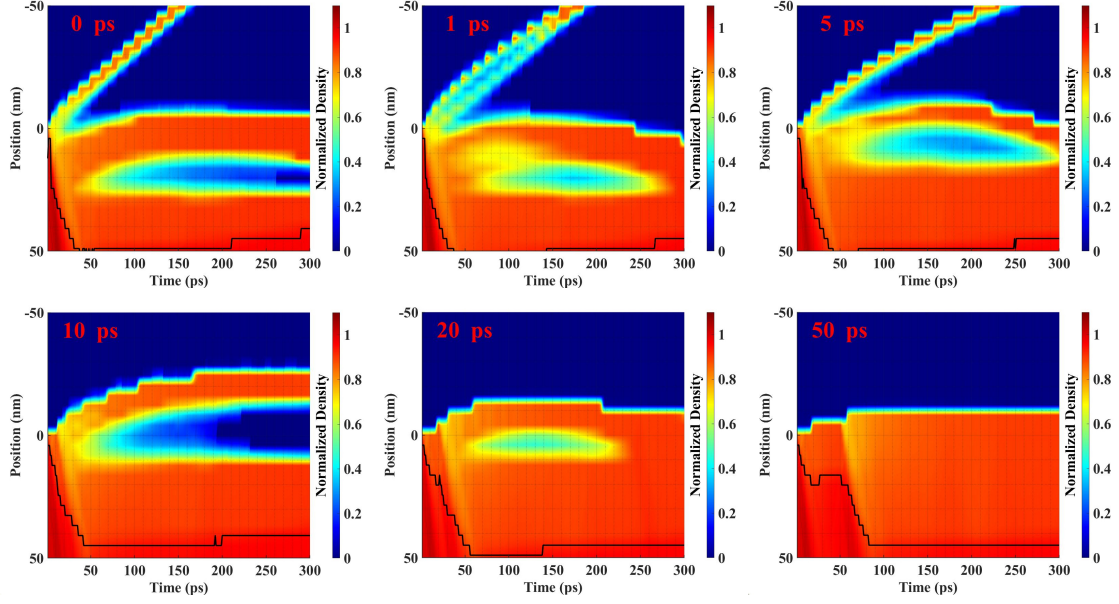


Figure 8.1. Colormaps of target density in gold irradiated by two identical pulses each of absorbed fluences 25 mJ/cm^2 with different delay times. The black lines indicate the solid-liquid interface.

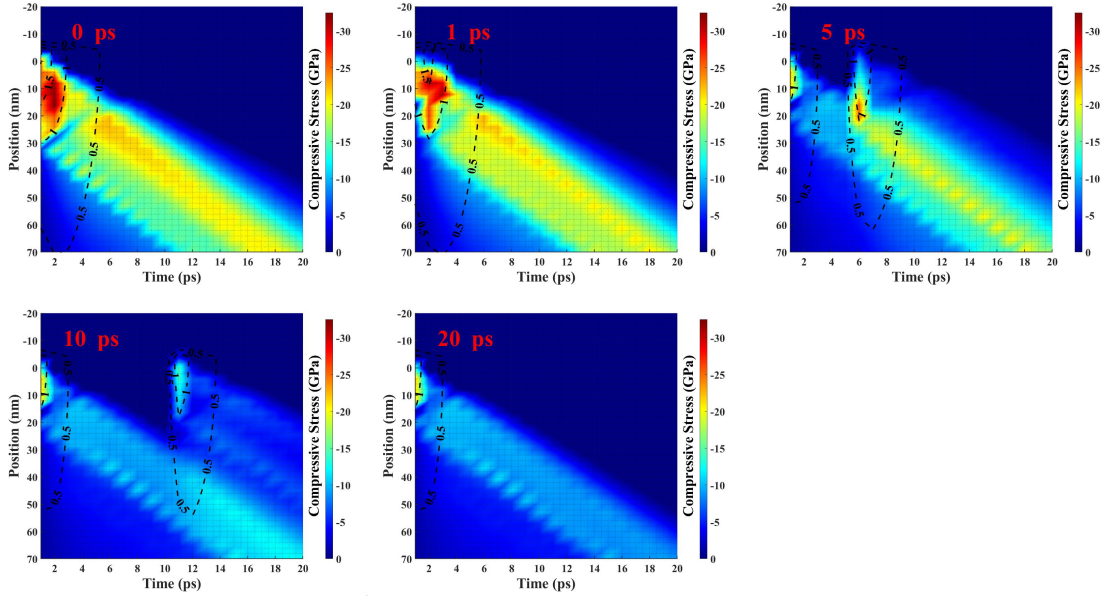


Figure 8.2. Colormaps of target compressive stress in gold irradiated by two identical pulses each of absorbed fluences 25 mJ/cm^2 with different delay times. The black dashed lines indicate the electron temperature in eV.

The tensile stress following the compressive stress wave is shown in Figure 8.4. Unlike the compressive stresses, the tensile stresses are of similar values across different delay times. The delay time only changes the time when the tensile stress peak occurs. The tensile stress in solid in the case of 50 ps delay time has different shape of that in liquid in the cases of other delay times.

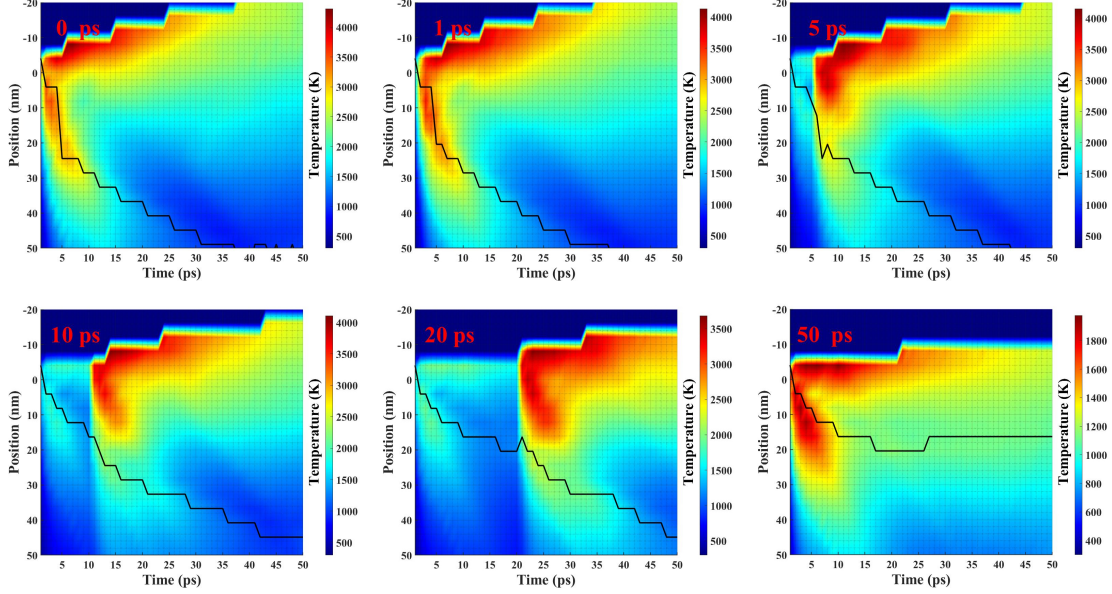


Figure 8.3. Colormaps of target lattice temperature in gold irradiated by two identical pulses each of absorbed fluences 25 mJ/cm^2 with different delay times. The black lines indicate the solid-liquid interface.

8.4 High overall absorbed fluence

In this section, we studied double pulse each of absorbed fluences 50 mJ/cm^2 with different delay times. The overall absorbed fluence is 100 mJ/cm^2 . We made sure the second pulse hit the target before the ablation caused by the first pulse, therefore we only studied the cases with delay time up to 10 ps.

Figure 8.5 shows the density of the gold target irradiated by double pulses with different delay times. With increasing delay time up to 10 ps, the effects of spallation become weaker. This is reflected by the thinner and slower layers ablated by spallation. At the same time, the effects of phase explosion become stronger, this can be observed in Figure 8.5 and it is

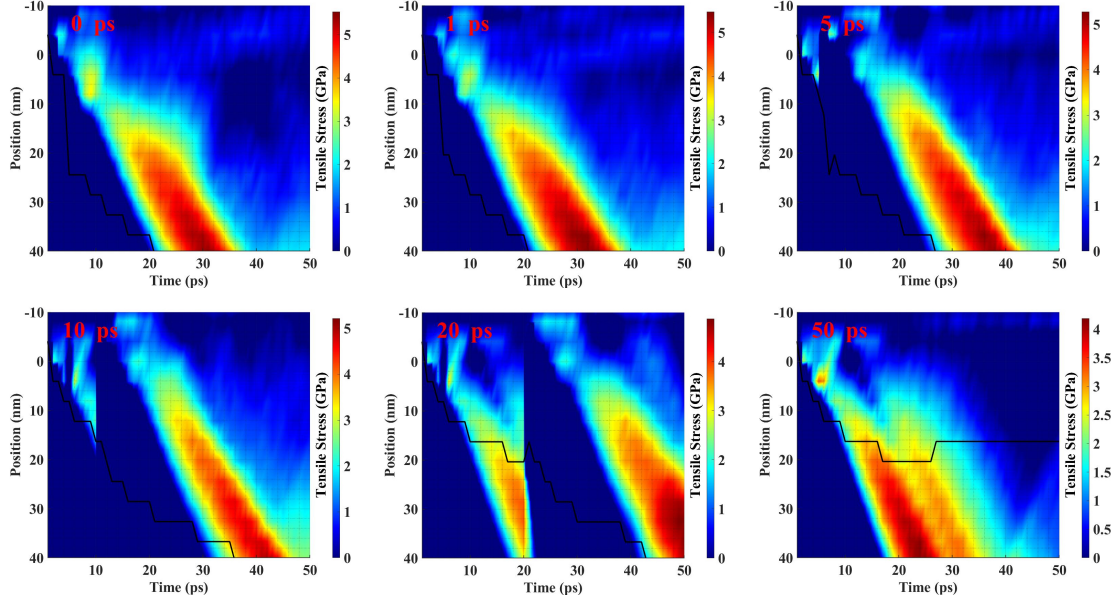


Figure 8.4. Colormaps of target tensile stress in gold irradiated by two identical pulses each of absorbed fluences 25 mJ/cm^2 with different delay times. The black lines indicate the solid-liquid interface.

also reflected by the lattice temperature as shown in Figure 8.6. With longer delay time, the surface electron temperatures before the second pulse become lower, and this leads to lower electron thermal conductivity. Therefore, heating of the surface electrons by the second pulse results in hotter lattice through electron-lattice coupling. Phase explosion is strongly affected by the rapid heating of the lattice causing rapid boiling. Therefore, with higher surface temperature in the cases of longer delay time, phase explosion is stronger.

However, the overall ablation depth in the case of longer delay times is smaller due to weaker spallation, as shown in Figure 8.5.

8.5 Summary

We performed simulations with low and high absorbed fluences to study the effect of delay time between two pulses on the ablation process. With low absorbed fluence, ablation mechanism changes from nonthermal ablation with 0 ps delay time to spallation with 10 ps delay time and to no ablation with delay time longer than 20 ps. While with high absorbed fluence, longer delay time enhances phase explosion and hinders spallation.

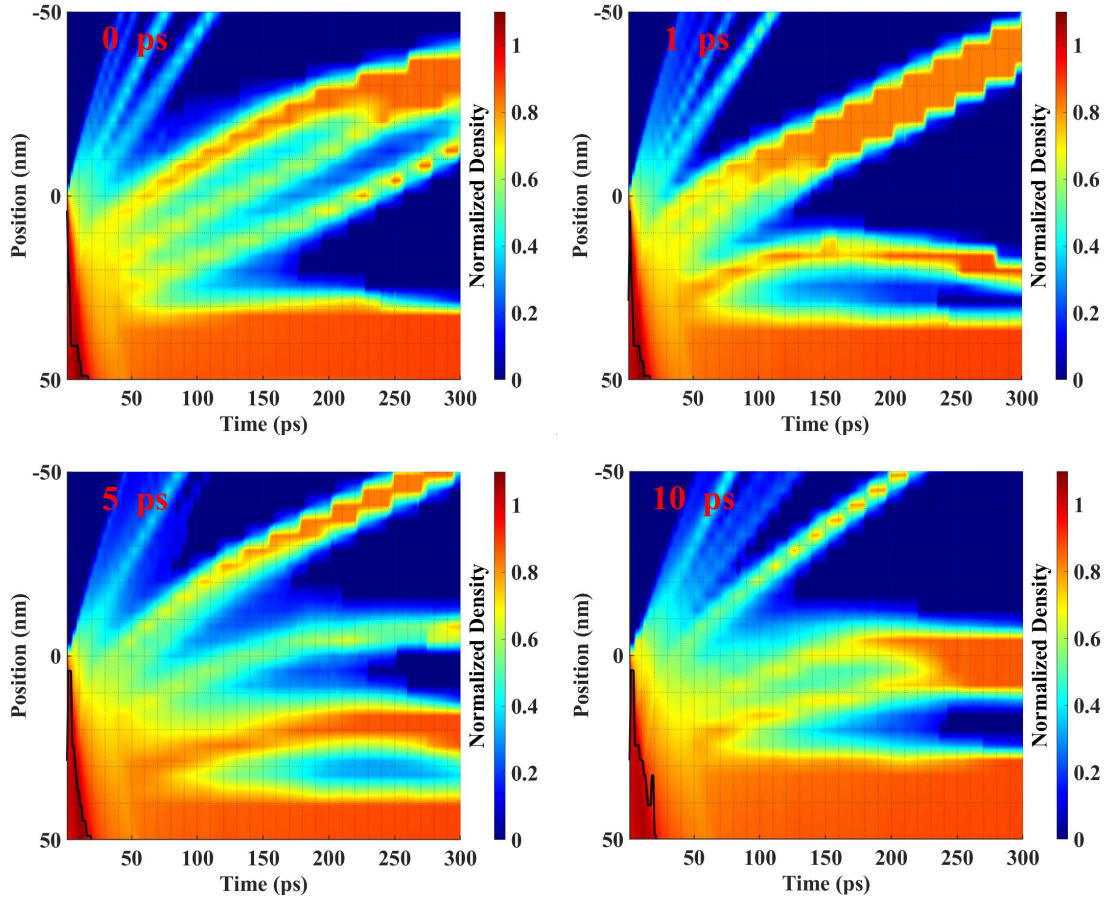


Figure 8.5. Colormaps of target density in gold irradiated by double identical pulses each of absorbed fluences 50 mJ/cm^2 with different delay times. The black lines indicate the solid-liquid interface.

As mentioned in the previous chapter, nonthermal ablation and phase explosion will ablate more single atoms and small clusters, while spallation will ablate thick liquid layers which will disintegrate and form nanoparticles. Therefore, for better production of nanoparticles, low absorbed fluence with 10 ps delay time is optimal according to our study.

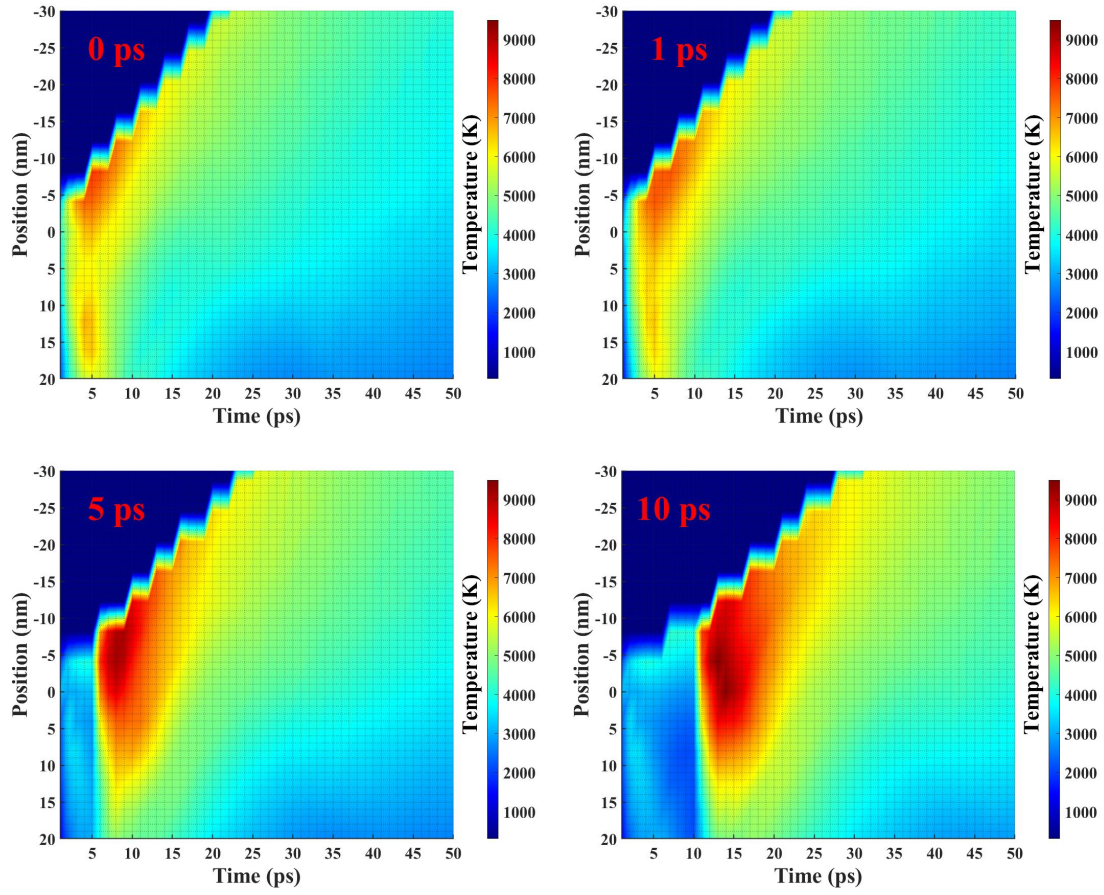


Figure 8.6. Colormaps of target lattice temperature in gold irradiated by two identical pulses each of absorbed fluences 50 mJ/cm^2 with different delay times.

9. SUMMARY AND FUTURE WORK

9.1 Summary

The dissertation reports the development of a numerical method combining molecular dynamics (MD) and the two-temperature model (TTM) considering the electron temperature dependence of all thermodynamic parameters and the interatomic potential to study phase change and ablation of gold after femtosecond laser irradiation. The electron blast force caused by the free electron pressure has two different equations. One shows that the electron blast force vanishes at the surface and the other shows that it peaks at the surface. We conjecture that this force should cause only lattice deformation in the material; therefore, the expression that vanishes at the surface should be used. The flux-limited model was also included to account for the inaccuracy of Fourier thermal conduction law when the electron temperature gradient is steep. A pressure transmitting and heat conducting boundary is used between the atomistic and the continuum parts for bulk materials. Introducing continuum parts to replace atomistic parts in the bulk greatly reduces the computational work without affecting the accuracy of the calculations.

Collision theory was used to obtain the electron collision frequencies, which are required in the calculation of electron thermal conductivity. However, the interpolation between the solid state and plasma state using collision theory underestimates the complexity of warm dense matter and therefore, the corresponding heat capacity and thermal conductivity differ significantly from the *ab initio* calculations and analytical expressions from other studies.

Melting of gold was extensively studied with an electron temperature independent (ETI) interatomic potential. Even the ETI potential overestimates the bond strength at high electron temperatures, melting is rarely affected since the temperature at the solid-liquid interface is relatively low. Especially, the effects of the target thickness on melting were investigated. Homogeneous melting was found in the case of thin films and melting growing with the movement of the solid-liquid interface was seen in the case of thick film and bulk.

The ablation process was studied with the electron temperature dependent (ETD) interatomic potential. Three ablation mechanisms were found in our simulations with different laser fluence. Short nonthermal ablation was only observed at the ablation threshold. Non-

thermal ablation was caused by the electronic pressure from localized electrons implicitly described by ETD potential. With increasing laser fluence, spallation occurred. Spallation, which is the ablation of liquid layers, was caused by thermal expansion of surface and tensile stress following the strong compressive stress wave. In the high laser fluence regime, phase explosion occurred on the surface and coexisted with spallation. Phase explosion is also called explosive boiling which occurs when the strong rapid heating of lattice causes rapid phase change.

The effects of the delay time in double pulse irradiation were also studied. It is shown that delay time has a minimal effect on melting depth and mostly affects processes on the surface. In the low laser fluence regime, nonthermal ablation was observed for single pulse irradiation, which is considered double pulse irradiation without delay between the pulses. Spallation occurs with increasing delay time; however, increasing the delay time too much causes spallation to disappear, resulting no ablation. In the high laser fluence regime, phase explosion gets stronger with longer delay time while spallation becomes weaker. Therefore, for better nanoparticle production (more and thicker ablated layers from spallation), low ablation regime with an optimal delay time is preferred.

9.2 Future work

To extend this work, one simple way is to study other metals, semiconductors, and dielectrics using our Femto3D code. The difficulty for all these simulations is to obtain material thermodynamic parameters. Coulomb explosion does not influence much in metals since there are enough free electrons to cause effective screening [54]. However, it will not be the case for semiconductors and dielectrics. Therefore, for these two kinds of materials, an extra force from the electric field caused by nonequilibrium electrons should be added to the model. The surrounding of the target has a great influence on the melting and ablation of the material. The effects of noble gases of different pressures or liquid, such as water [84], are worth to investigate.

If the computational power is allowed, simulations in larger temporal and spatial scales can study the formation of nanoparticles and their spatial, size, and velocity distribution.

Defects in materials and their effects of material properties can be studied as well. Moreover, without expanding the lateral area in the MD simulations, a finite element (FE) method can be used to describe the surrounding area of the MD region. A seamless coupling (handshakes) method connecting the FE and MD regions was proposed by Broughton *et al.* [85].

As mentioned in Chapter 7, a more accurate ETD potential, which is continuously changed with the electron temperature, can give more insights in the nonthermal ablation process. Experiments measuring the thermodynamic parameters, especially K_e and G , would contribute much to the quantitative results.

At much higher laser fluence regime (beyond the studies in the dissertation), electron emission [56] and melt expulsion mentioned by Zhigilei *et al.* [41] should be considered. The latter process can be studied by replacing the classical TTM model by a hydrodynamic two-temperature hybrid model (HD-TTM) in the continuum part for bulk materials.

Decomposition of the ablated layers and redeposition of the ablated matter are important in the study of nanoparticle production and micromachining, respectively. Since both happen at much later times (> 1 ns) and require greater temporal and spatial scales, hydrodynamic model may be a good option to study these processes.

Our simulations showed that preheating the target to a temperature below the melting point has similar effects on the ablation process as the double pulse simulations at low fluences, which can convert nonthermal ablation to spallation to achieve better nanoparticle production. Preheating the target, however, is a much less expensive way in terms of laser energy input compared with double pulse irradiation. Experiments to verify these simulation results are needed.

REFERENCES

- [1] S. Nolte, C. Momma, H. Jacobs, A. Tünnermann, B. N. Chichkov, B. Wellegehausen, and H. Welling, “Ablation of metals by ultrashort laser pulses,” *J. Opt. Soc. Am. B*, vol. 14, no. 10, pp. 2716–2722, Oct. 1997. DOI: [10.1364/JOSAB.14.002716](https://doi.org/10.1364/JOSAB.14.002716). [Online]. Available: <http://josab.osa.org/abstract.cfm?URI=josab-14-10-2716>.
- [2] K. Furusawa, K. Takahashi, H. Kumagai, K. Midorikawa, and M. Obara, “Ablation characteristics of au, ag, and cu metals using a femtosecond ti:sapphire laser,” *Applied Physics A: Materials Science & Processing*, vol. 69, no. 7, S359–S366, Dec. 1999, ISSN: 0947-8396, 1432-0630. DOI: [10.1007/s003390051417](https://doi.org/10.1007/s003390051417).
- [3] M. V. Shugaev, C. Wu, O. Armbruster, A. Naghilou, N. Brouwer, D. S. Ivanov, T. J.-Y. Derrien, N. M. Bulgakova, W. Kautek, B. Rethfeld, and et al., “Fundamentals of ultrafast laser–material interaction,” *MRS Bulletin*, vol. 41, no. 12, pp. 960–968, 2016. DOI: [10.1557/mrs.2016.274](https://doi.org/10.1557/mrs.2016.274).
- [4] B. Rethfeld, D. S. Ivanov, M. E. Garcia, and S. I. Anisimov, “Modelling ultrafast laser ablation,” *Journal of Physics D: Applied Physics*, vol. 50, no. 19, p. 193 001, Apr. 2017. DOI: [10.1088/1361-6463/50/19/193001](https://doi.org/10.1088/1361-6463/50/19/193001). [Online]. Available: <https://doi.org/10.1088/1361-6463/50/19/193001>.
- [5] A. A. Ionin, S. I. Kudryashov, and A. A. Samokhin, “Material surface ablation produced by ultrashort laser pulses,” *Physics-Uspekhi*, vol. 60, no. 2, pp. 149–160, Feb. 2017. DOI: [10.3367/ufne.2016.09.037974](https://doi.org/10.3367/ufne.2016.09.037974). [Online]. Available: <https://doi.org/10.3367/ufne.2016.09.037974>.
- [6] A. H. Zewail, “Femtochemistry,” in *Femtochemistry: Ultrafast Dynamics of the Chemical Bond*, pp. 3–22. DOI: [10.1142/9789814287609_0001](https://doi.org/10.1142/9789814287609_0001). [Online]. Available: https://www.worldscientific.com/doi/abs/10.1142/9789814287609_0001.
- [7] W. H. Knox, “Ultrafast technology in telecommunications,” *IEEE Journal of Selected Topics in Quantum Electronics*, vol. 6, no. 6, pp. 1273–1278, 2000. DOI: [10.1109/2944.902178](https://doi.org/10.1109/2944.902178).
- [8] V. Margetic, A. Pakulev, A. Stockhaus, M. Bolshov, K. Niemax, and R. Hergenröder, “A comparison of nanosecond and femtosecond laser-induced plasma spectroscopy of brass samples,” *Spectrochimica Acta Part B: Atomic Spectroscopy*, vol. 55, no. 11, pp. 1771–1785, 2000, ISSN: 0584-8547. DOI: [https://doi.org/10.1016/S0584-8547\(00\)00275-5](https://doi.org/10.1016/S0584-8547(00)00275-5). [Online]. Available: <https://www.sciencedirect.com/science/article/pii/S0584854700002755>.

- [9] K. Stelmazczyk, P. Rohwetter, G. Méjean, J. Yu, E. Salmon, J. Kasparian, R. Ackermann, J.-P. Wolf, and L. Wöste, “Long-distance remote laser-induced breakdown spectroscopy using filamentation in air,” *Applied Physics Letters*, vol. 85, no. 18, pp. 3977–3979, 2004. DOI: [10.1063/1.1812843](https://doi.org/10.1063/1.1812843). eprint: <https://doi.org/10.1063/1.1812843>. [Online]. Available: <https://doi.org/10.1063/1.1812843>.
- [10] D. Bäuerle, *Laser processing and chemistry*, Fourth edition. Springer, 2011, ISBN: 978-3-642-17613-5. [Online]. Available: <https://doi.org/10.1007/978-3-642-17613-5>.
- [11] M. von Allmen and A. Blatter, *Laser-Beam Interactions with Materials*, ser. Springer Series in Materials Science. Springer Berlin Heidelberg, 1995, vol. 2, ISBN: 978-3-540-59401-7. DOI: [10.1007/978-3-642-57813-7](https://doi.org/10.1007/978-3-642-57813-7). [Online]. Available: <http://link.springer.com/10.1007/978-3-642-57813-7>.
- [12] S. Noël, J. Hermann, and T. Itina, “Investigation of nanoparticle generation during femtosecond laser ablation of metals,” *Applied Surface Science*, vol. 253, no. 15, pp. 6310–6315, 2007, ISSN: 0169-4332. DOI: <https://doi.org/10.1016/j.apsusc.2007.01.081>. [Online]. Available: <https://www.sciencedirect.com/science/article/pii/S0169433207001468>.
- [13] B. Rethfeld, A. Kaiser, M. Vicanek, and G. Simon, “Ultrafast dynamics of nonequilibrium electrons in metals under femtosecond laser irradiation,” *Phys. Rev. B*, vol. 65, p. 214 303, 21 May 2002. DOI: [10.1103/PhysRevB.65.214303](https://doi.org/10.1103/PhysRevB.65.214303). [Online]. Available: <https://link.aps.org/doi/10.1103/PhysRevB.65.214303>.
- [14] S.-S. Wellershoff, J. Hohlfeld, J. Gädde, and E. Matthias, “The role of electron–phonon coupling in femtosecond laser damage of metals,” *Applied Physics A*, vol. 69, no. 1, S99–S107, Dec. 1999, ISSN: 1432-0630. DOI: [10.1007/s003399900305](https://doi.org/10.1007/s003399900305).
- [15] G. Du, F. Chen, Q. Yang, J. Si, and X. Hou, “Ultrafast temperature relaxation evolution in au film under femtosecond laser pulses irradiation,” *Optics Communications*, vol. 283, no. 9, pp. 1869–1872, 2010, ISSN: 0030-4018. DOI: <https://doi.org/10.1016/j.optcom.2009.12.038>. [Online]. Available: <https://www.sciencedirect.com/science/article/pii/S003040180901311X>.
- [16] A. Suslova, “Multi-dimensional simulation and experimental benchmarking of ultra-short pulsed laser interactions with metallic targets,” 2018.
- [17] J. Zheng, Z. Chen, and Z. Liu, “Atomic force microscopy-based nanolithography on silicon using colloidal au nanoparticles as a nanooxidation mask,” *Langmuir*, vol. 16, no. 24, pp. 9673–9676, 2000. DOI: [10.1021/la000705e](https://doi.org/10.1021/la000705e). eprint: <https://doi.org/10.1021/la000705e>. [Online]. Available: <https://doi.org/10.1021/la000705e>.

- [18] A. T. Bell, “The impact of nanoscience on heterogeneous catalysis,” *Science*, vol. 299, no. 5613, pp. 1688–1691, 2003, ISSN: 0036-8075. DOI: [10.1126/science.1083671](https://doi.org/10.1126/science.1083671). eprint: <https://science.sciencemag.org/content/299/5613/1688.full.pdf>. [Online]. Available: <https://science.sciencemag.org/content/299/5613/1688>.
- [19] Y. Xiao, F. Patolsky, E. Katz, J. F. Hainfeld, and I. Willner, “”plugging into enzymes”: Nanowiring of redox enzymes by a gold nanoparticle,” *Science*, vol. 299, no. 5614, pp. 1877–1881, 2003, ISSN: 0036-8075. DOI: [10.1126/science.1080664](https://doi.org/10.1126/science.1080664). eprint: <https://science.sciencemag.org/content/299/5614/1877.full.pdf>. [Online]. Available: <https://science.sciencemag.org/content/299/5614/1877>.
- [20] S. O. Obare, R. E. Hollowell, and C. J. Murphy, “Sensing strategy for lithium ion based on gold nanoparticles,” *Langmuir*, vol. 18, no. 26, pp. 10 407–10 410, 2002. DOI: [10.1021/la0260335](https://doi.org/10.1021/la0260335). eprint: <https://doi.org/10.1021/la0260335>. [Online]. Available: <https://doi.org/10.1021/la0260335>.
- [21] R. Ernstorfer, M. Harb, C. T. Hebeisen, G. Sciaini, T. Dartigalongue, and R. J. D. Miller, “The formation of warm dense matter: Experimental evidence for electronic bond hardening in gold,” *Science*, vol. 323, no. 5917, pp. 1033–1037, 2009, ISSN: 0036-8075. DOI: [10.1126/science.1162697](https://doi.org/10.1126/science.1162697). eprint: <https://science.sciencemag.org/content/323/5917/1033.full.pdf>. [Online]. Available: <https://science.sciencemag.org/content/323/5917/1033>.
- [22] Z. Lin, L. V. Zhigilei, and V. Celli, “Electron-phonon coupling and electron heat capacity of metals under conditions of strong electron-phonon nonequilibrium,” *Phys. Rev. B*, vol. 77, p. 075 133, 7 Feb. 2008. DOI: [10.1103/PhysRevB.77.075133](https://doi.org/10.1103/PhysRevB.77.075133). [Online]. Available: <https://link.aps.org/doi/10.1103/PhysRevB.77.075133>.
- [23] Y. V. Petrov, N. A. Inogamov, S. I. Anisimov, K. P. Migdal, V. A. Khokhlov, and K. V. Khishchenko, “Thermal conductivity of condensed gold in states with the strongly excited electron subsystem,” *Journal of Physics: Conference Series*, vol. 653, p. 012 087, Nov. 2015. DOI: [10.1088/1742-6596/653/1/012087](https://doi.org/10.1088/1742-6596/653/1/012087). [Online]. Available: <https://doi.org/10.1088/1742-6596/653/1/012087>.
- [24] S. I. Anisimov and B. Rethfeld, “Theory of ultrashort laser pulse interaction with a metal,” in *Nonresonant Laser-Matter Interaction (NLMI-9)*, V. I. Konov and M. N. Libenson, Eds., International Society for Optics and Photonics, vol. 3093, SPIE, 1997, pp. 192–203. DOI: [10.1117/12.271674](https://doi.org/10.1117/12.271674). [Online]. Available: <https://doi.org/10.1117/12.271674>.

- [25] S. I. Ashitkov, P. S. Komarov, V. V. Zhakhovsky, Y. V. Petrov, V. A. Khokhlov, A. A. Yurkevich, D. K. Il'nitsky, N. A. Inogamov, and M. B. Agranat, "Ablation of gold irradiated by femtosecond laser pulse: Experiment and modeling," *Journal of Physics: Conference Series*, vol. 774, p. 012097, Nov. 2016. DOI: [10.1088/1742-6596/774/1/012097](https://doi.org/10.1088/1742-6596/774/1/012097). [Online]. Available: <https://doi.org/10.1088/1742-6596/774/1/012097>.
- [26] T. Q. Qiu and C. L. Tien, "Heat Transfer Mechanisms During Short-Pulse Laser Heating of Metals," *Journal of Heat Transfer*, vol. 115, no. 4, pp. 835–841, Nov. 1993, ISSN: 0022-1481. DOI: [10.1115/1.2911377](https://doi.org/10.1115/1.2911377). eprint: https://asmedigitalcollection.asme.org/heattransfer/article-pdf/115/4/835/5698866/835_1.pdf. [Online]. Available: <https://doi.org/10.1115/1.2911377>.
- [27] D. S. Ivanov and L. V. Zhigilei, "Combined atomistic-continuum modeling of short-pulse laser melting and disintegration of metal films," *Phys. Rev. B*, vol. 68, p. 064114, 6 Aug. 2003. DOI: [10.1103/PhysRevB.68.064114](https://doi.org/10.1103/PhysRevB.68.064114). [Online]. Available: <https://link.aps.org/doi/10.1103/PhysRevB.68.064114>.
- [28] A. Y. Vorobyev and C. Guo, "Enhanced absorptance of gold following multipulse femtosecond laser ablation," *Phys. Rev. B*, vol. 72, p. 195422, 19 Nov. 2005. DOI: [10.1103/PhysRevB.72.195422](https://doi.org/10.1103/PhysRevB.72.195422). [Online]. Available: <https://link.aps.org/doi/10.1103/PhysRevB.72.195422>.
- [29] J. Hermann, S. Noël, T. E. Itina, E. Axente, and M. E. Povarnitsyn, "Correlation between ablation efficiency and nanoparticle generation during the short-pulse laser ablation of metals," *Laser Physics*, vol. 18, no. 4, pp. 374–379, Apr. 2008, ISSN: 1555-6611. DOI: [10.1134/s11490-008-4002-6](https://doi.org/10.1134/s11490-008-4002-6).
- [30] M. Hashida, A. Semerok, O. Gobert, G. Petite, Y. Izawa, and J. Wagner, "Ablation threshold dependence on pulse duration for copper," *Applied Surface Science*, vol. 197–198, pp. 862–867, 2002, COLA'01 SI, ISSN: 0169-4332. DOI: [https://doi.org/10.1016/S0169-4332\(02\)00463-4](https://doi.org/10.1016/S0169-4332(02)00463-4). [Online]. Available: <https://www.sciencedirect.com/science/article/pii/S0169433202004634>.
- [31] D. Roberts, A. du Plessis, and L. Botha, "Femtosecond laser ablation of silver foil with single and double pulses," *Applied Surface Science*, vol. 256, no. 6, pp. 1784–1792, 2010, ISSN: 0169-4332. DOI: <https://doi.org/10.1016/j.apsusc.2009.10.004>. [Online]. Available: <https://www.sciencedirect.com/science/article/pii/S0169433209014202>.
- [32] S. Amoruso, R. Bruzzese, X. Wang, and J. Xia, "Propagation of a femtosecond pulsed laser ablation plume into a background atmosphere," *Applied Physics Letters*, vol. 92, no. 4, p. 041503, 2008. DOI: [10.1063/1.2839582](https://doi.org/10.1063/1.2839582). eprint: <https://doi.org/10.1063/1.2839582>. [Online]. Available: <https://doi.org/10.1063/1.2839582>.

- [33] S. I. Anisimov, B. L. Kapeliovich, and T. L. Perelman, “Electron emission from metal surfaces exposed to ultrashort laser pulses,” *Zhurnal Eksperimentalnoi i Teoreticheskoi Fiziki*, vol. 66, pp. 776–781, Aug. 1974, Provided by the SAO/NASA Astrophysics Data System. [Online]. Available: <https://ui.adsabs.harvard.edu/abs/1974ZhETF..66.776A>.
- [34] L. Jiang and H.-L. Tsai, “Improved Two-Temperature Model and Its Application in Ultrashort Laser Heating of Metal Films,” *Journal of Heat Transfer*, vol. 127, no. 10, pp. 1167–1173, Jun. 2005, ISSN: 0022-1481. DOI: [10.1115/1.2035113](https://doi.org/10.1115/1.2035113). eprint: https://asmedigitalcollection.asme.org/heattransfer/article-pdf/127/10/1167/5504614/1167_1.pdf. [Online]. Available: <https://doi.org/10.1115/1.2035113>.
- [35] A. Suslova and A. Hassanein, “Simulation of femtosecond laser absorption by metallic targets and their thermal evolution,” *Laser and Particle Beams*, vol. 35, no. 3, pp. 415–428, 2017. DOI: [10.1017/S0263034617000404](https://doi.org/10.1017/S0263034617000404).
- [36] N. Nedialkov, P. Atanasov, S. Amoruso, R. Bruzzese, and X. Wang, “Laser ablation of metals by femtosecond pulses: Theoretical and experimental study,” *Applied Surface Science*, vol. 253, no. 19, pp. 7761–7766, 2007, Photon-Assisted Synthesis and Processing of Functional Materials, ISSN: 0169-4332. DOI: <https://doi.org/10.1016/j.apsusc.2007.02.083>. [Online]. Available: <https://www.sciencedirect.com/science/article/pii/S0169433207003182>.
- [37] L. J. Lewis and D. Perez, “Laser ablation with short and ultrashort laser pulses: Basic mechanisms from molecular-dynamics simulations,” *Applied Surface Science*, vol. 255, no. 10, pp. 5101–5106, 2009, Laser and Plasma in Micro- and Nano-Scale Materials Processing and Diagnostics, ISSN: 0169-4332. DOI: <https://doi.org/10.1016/j.apsusc.2008.07.116>. [Online]. Available: <https://www.sciencedirect.com/science/article/pii/S0169433208017285>.
- [38] M. W. Finnis, P. Agnew, and A. J. E. Foreman, “Thermal excitation of electrons in energetic displacement cascades,” *Phys. Rev. B*, vol. 44, pp. 567–574, 2 Jul. 1991. DOI: [10.1103/PhysRevB.44.567](https://doi.org/10.1103/PhysRevB.44.567). [Online]. Available: <https://link.aps.org/doi/10.1103/PhysRevB.44.567>.
- [39] H. Hakkinen and U. Landman, “Superheating, melting, and annealing of copper surfaces,” *Phys. Rev. Lett.*, vol. 71, pp. 1023–1026, 7 Aug. 1993. DOI: [10.1103/PhysRevLett.71.1023](https://doi.org/10.1103/PhysRevLett.71.1023). [Online]. Available: <https://link.aps.org/doi/10.1103/PhysRevLett.71.1023>.
- [40] C. Schäfer, H. M. Urbassek, and L. V. Zhigilei, “Metal ablation by picosecond laser pulses: A hybrid simulation,” *Phys. Rev. B*, vol. 66, p. 115404, 11 Sep. 2002. DOI: [10.1103/PhysRevB.66.115404](https://doi.org/10.1103/PhysRevB.66.115404). [Online]. Available: <https://link.aps.org/doi/10.1103/PhysRevB.66.115404>.

- [41] L. V. Zhigilei, Z. Lin, and D. S. Ivanov, “Atomistic modeling of short pulse laser ablation of metals: Connections between melting, spallation, and phase explosion,” *The Journal of Physical Chemistry C*, vol. 113, no. 27, pp. 11 892–11 906, 2009. DOI: [10.1021/jp902294m](https://doi.org/10.1021/jp902294m). [Online]. Available: <https://doi.org/10.1021/jp902294m>.
- [42] C. Wu and L. V. Zhigilei, “Microscopic mechanisms of laser spallation and ablation of metal targets from large-scale molecular dynamics simulations,” *Applied Physics A*, vol. 114, no. 1, pp. 11–32, Jan. 2014, ISSN: 0947-8396, 1432-0630. DOI: [10.1007/s00339-013-8086-4](https://doi.org/10.1007/s00339-013-8086-4).
- [43] G. E. Norman, S. V. Starikov, and V. V. Stegailov, “Atomistic simulation of laser ablation of gold: Effect of pressure relaxation,” *Journal of Experimental and Theoretical Physics*, vol. 114, pp. 792–800, 5 May 2012, ISSN: 1090-6509. DOI: [10.1134/S1063776112040115](https://doi.org/10.1134/S1063776112040115).
- [44] C. Schäfer, H. M. Urbassek, L. V. Zhigilei, and B. J. Garrison, “Pressure-transmitting boundary conditions for molecular-dynamics simulations,” *Computational Materials Science*, vol. 24, no. 4, pp. 421–429, 2002, ISSN: 0927-0256. DOI: [https://doi.org/10.1016/S0927-0256\(01\)00263-4](https://doi.org/10.1016/S0927-0256(01)00263-4). [Online]. Available: <https://www.sciencedirect.com/science/article/pii/S0927025601002634>.
- [45] W. Yuan and T. Sizyuk, “Ablation study in gold irradiated by single femtosecond laser pulse with electron temperature dependent interatomic potential and electron–phonon coupling factor,” *Laser Physics*, vol. 31, no. 3, p. 036 002, Feb. 2021. DOI: [10.1088/1555-6611/abdcb8](https://doi.org/10.1088/1555-6611/abdcb8). [Online]. Available: <https://doi.org/10.1088/1555-6611/abdcb8>.
- [46] D. M. Duffy and A. M. Rutherford, “Including the effects of electronic stopping and electron–ion interactions in radiation damage simulations,” *Journal of Physics: Condensed Matter*, vol. 19, no. 1, p. 016 207, Dec. 2006. DOI: [10.1088/0953-8984/19/1/016207](https://doi.org/10.1088/0953-8984/19/1/016207). [Online]. Available: <https://doi.org/10.1088/0953-8984/19/1/016207>.
- [47] A. M. Rutherford and D. M. Duffy, “The effect of electron–ion interactions on radiation damage simulations,” *Journal of Physics: Condensed Matter*, vol. 19, no. 49, p. 496 201, Nov. 2007. DOI: [10.1088/0953-8984/19/49/496201](https://doi.org/10.1088/0953-8984/19/49/496201). [Online]. Available: <https://doi.org/10.1088/0953-8984/19/49/496201>.
- [48] L. A. Falkovsky and E. G. Mishchenko, “Electron-lattice kinetics of metals heated by ultrashort laser pulses,” *Journal of Experimental and Theoretical Physics*, vol. 88, no. 1, pp. 84–88, Jan. 1999, ISSN: 1090-6509. DOI: [10.1134/1.558768](https://doi.org/10.1134/1.558768).

- [49] J. Chen, J. Beraun, L. Grimes, and D. Tzou, “Modeling of femtosecond laser-induced non-equilibrium deformation in metal films,” *International Journal of Solids and Structures*, vol. 39, no. 12, pp. 3199–3216, 2002, ISSN: 0020-7683. DOI: [https://doi.org/10.1016/S0020-7683\(02\)00242-1](https://doi.org/10.1016/S0020-7683(02)00242-1). [Online]. Available: <https://www.sciencedirect.com/science/article/pii/S0020768302002421>.
- [50] J. Chen, D. Tzou, and J. Beraun, “A semiclassical two-temperature model for ultrafast laser heating,” *International Journal of Heat and Mass Transfer*, vol. 49, no. 1, pp. 307–316, 2006, ISSN: 0017-9310. DOI: <https://doi.org/10.1016/j.ijheatmasstransfer.2005.06.022>. [Online]. Available: <https://www.sciencedirect.com/science/article/pii/S001793100500445X>.
- [51] V. Stegailov and P. Zhilyaev, “Pressure in electronically excited warm dense metals,” *Contributions to Plasma Physics*, vol. 55, no. 2-3, pp. 164–171, 2015. DOI: <https://doi.org/10.1002/ctpp.201400103>. [Online]. Available: <https://onlinelibrary.wiley.com/doi/abs/10.1002/ctpp.201400103>.
- [52] R. C. Malone, R. L. McCrory, and R. L. Morse, “Indications of strongly flux-limited electron thermal conduction in laser-target experiments,” *Phys. Rev. Lett.*, vol. 34, pp. 721–724, 12 Mar. 1975. DOI: [10.1103/PhysRevLett.34.721](https://doi.org/10.1103/PhysRevLett.34.721). [Online]. Available: <https://link.aps.org/doi/10.1103/PhysRevLett.34.721>.
- [53] A. Suslova and A. Hassanein, “Numerical simulation of ballistic electron dynamics and heat transport in metallic targets exposed to ultrashort laser pulse,” *Journal of Applied Physics*, vol. 124, no. 6, p. 065 108, 2018. DOI: [10.1063/1.5027401](https://doi.org/10.1063/1.5027401). eprint: <https://doi.org/10.1063/1.5027401>. [Online]. Available: <https://doi.org/10.1063/1.5027401>.
- [54] V. Schmidt, W. Husinsky, and G. Betz, “Dynamics of laser desorption and ablation of metals at the threshold on the femtosecond time scale,” *Phys. Rev. Lett.*, vol. 85, pp. 3516–3519, 16 Oct. 2000. DOI: [10.1103/PhysRevLett.85.3516](https://doi.org/10.1103/PhysRevLett.85.3516). [Online]. Available: <https://link.aps.org/doi/10.1103/PhysRevLett.85.3516>.
- [55] N. M. Bulgakova, R. Stoian, A. Rosenfeld, I. V. Hertel, and E. E. B. Campbell, “Electronic transport and consequences for material removal in ultrafast pulsed laser ablation of materials,” *Phys. Rev. B*, vol. 69, p. 054 102, 5 Feb. 2004. DOI: [10.1103/PhysRevB.69.054102](https://doi.org/10.1103/PhysRevB.69.054102). [Online]. Available: <https://link.aps.org/doi/10.1103/PhysRevB.69.054102>.
- [56] A. A. Ionin, S. I. Kudryashov, S. V. Makarov, P. N. Saltuganov, L. V. Seleznev, and D. V. Sinitsyn, “Ultrafast electron dynamics of material surfaces under the action of femtosecond laser pulses,” *Bulletin of the Russian Academy of Sciences: Physics*, vol. 80, no. 4, pp. 450–454, Apr. 2016, ISSN: 1062-8738, 1934-9432. DOI: [10.3103/S1062873816040158](https://doi.org/10.3103/S1062873816040158).

- [57] S. V. Starikov and V. V. Pisarev, “Atomistic simulation of laser-pulse surface modification: Predictions of models with various length and time scales,” *Journal of Applied Physics*, vol. 117, no. 13, p. 135 901, 2015. DOI: [10.1063/1.4916600](https://doi.org/10.1063/1.4916600). [Online]. Available: <https://doi.org/10.1063/1.4916600>.
- [58] M. P. Polek, “Effects of femtosecond laser irradiation of metallic and dielectric materials in the low-to-high fluence regimes,” Ph.D. dissertation, Purdue University, 2015. [Online]. Available: <http://search.proquest.com/openview/4b9694093f08d78c948850aff1c12c00/1?pq-origsite=gscholar&cbl=18750&diss=y>.
- [59] Z. Lin and L. V. Zhigilei, “Thermal excitation of d band electrons in Au: implications for laser-induced phase transformations,” in *High-Power Laser Ablation VI*, C. R. Phipps, Ed., International Society for Optics and Photonics, vol. 6261, SPIE, 2006, pp. 248–261. DOI: [10.1117/12.674636](https://doi.org/10.1117/12.674636). [Online]. Available: <https://doi.org/10.1117/12.674636>.
- [60] N. W. Ashcroft and N. D. Mermin, *Solid State Physics*, ser. HRW international editions. Holt, Rinehart and Winston, 1976, ISBN: 9780030839931. [Online]. Available: <https://books.google.com/books?id=1C9HAQAIAAJ>.
- [61] A. Bar-Shalom, M. Klapisch, and J. Oreg, “Hullac, an integrated computer package for atomic processes in plasmas,” *Journal of Quantitative Spectroscopy and Radiative Transfer*, vol. 71, no. 2, pp. 169–188, 2001, Radiative Properties of Hot Dense Matter, ISSN: 0022-4073. DOI: [https://doi.org/10.1016/S0022-4073\(01\)00066-8](https://doi.org/10.1016/S0022-4073(01)00066-8). [Online]. Available: <https://www.sciencedirect.com/science/article/pii/S0022407301000668>.
- [62] C. Fourment, F. Deneuville, D. Descamps, F. Dorchies, S. Petit, O. Peyrusse, B. Holst, and V. Recoules, “Experimental determination of temperature-dependent electron-electron collision frequency in isochorically heated warm dense gold,” *Phys. Rev. B*, vol. 89, p. 161 110, 16 Apr. 2014. DOI: [10.1103/PhysRevB.89.161110](https://doi.org/10.1103/PhysRevB.89.161110). [Online]. Available: <https://link.aps.org/doi/10.1103/PhysRevB.89.161110>.
- [63] A. D. Rakić, A. B. Djurišić, J. M. Elazar, and M. L. Majewski, “Optical properties of metallic films for vertical-cavity optoelectronic devices,” *Appl. Opt.*, vol. 37, no. 22, pp. 5271–5283, Aug. 1998. DOI: [10.1364/AO.37.005271](https://doi.org/10.1364/AO.37.005271). [Online]. Available: <http://ao.osa.org/abstract.cfm?URI=ao-37-22-5271>.
- [64] J. Callen, *Fundamentals of Plasma Physics*. CRC Press, 2006. [Online]. Available: <http://homepages.cae.wisc.edu/~callen/book.html>.
- [65] E. G. Gamaly, *Femtosecond laser-matter interaction: theory, experiments and applications*. CRC Press, 2011.

- [66] J. Robinson, J. McMurry, and R. Fay, *Chemistry*. Pearson Education, Incorporated, 2019, ISBN: 9780134856230. [Online]. Available: <https://books.google.com/books?id=ISdBuQEACAAJ>.
- [67] L. A. N. Laboratory. (2021). “Phase diagram for warm dense matter,” [Online]. Available: <https://www.lanl.gov/projects/dense-plasma-theory/background/warm-dense-matter.php>.
- [68] S. E. Kirkwood, Y. Y. Tsui, R. Fedosejevs, A. V. Brantov, and V. Y. Bychenkov, “Experimental and theoretical study of absorption of femtosecond laser pulses in interaction with solid copper targets,” *Phys. Rev. B*, vol. 79, p. 144 120, 14 Apr. 2009. DOI: [10.1103/PhysRevB.79.144120](https://doi.org/10.1103/PhysRevB.79.144120). [Online]. Available: <https://link.aps.org/doi/10.1103/PhysRevB.79.144120>.
- [69] A. Suslova and A. Hassanein, “Femtosecond laser absorption, heat propagation, and damage threshold analysis for au coating on metallic substrates,” *Applied Surface Science*, vol. 422, pp. 295–303, 2017, ISSN: 0169-4332. DOI: <https://doi.org/10.1016/j.apsusc.2017.05.230>. [Online]. Available: <https://www.sciencedirect.com/science/article/pii/S0169433217316070>.
- [70] J. R. Rumble, *CRC Handbook of Chemistry and Physics*, 101st ed. CRC Press, 2021. [Online]. Available: <http://hbcponline.com/faces/contents/ContentsSearch.xhtml>.
- [71] C. Kittel, P. McEuen, and P. McEuen, *Introduction to solid state physics*, 8th ed. Wiley New York, 2005.
- [72] D. G. Yakovlev and V. A. Urpin, “Thermal and Electrical Conductivity in White Dwarfs and Neutron Stars,” vol. 24, p. 303, Jun. 1980. [Online]. Available: <https://ui.adsabs.harvard.edu/abs/1980SvA....24..303Y>.
- [73] Y. V. Martynenko and Y. N. Yavlinskii, “Cooling of electron gas of a metal at high temperature,” in *Doklady Akademii Nauk*, Russian Academy of Sciences, vol. 270, 1983, pp. 88–91.
- [74] N. A. Inogamov and Y. V. Petrov, “Thermal conductivity of metals with hot electrons,” *Journal of Experimental and Theoretical Physics*, vol. 110, no. 3, pp. 446–468, Mar. 2010, ISSN: 1063-7761, 1090-6509. DOI: [10.1134/S1063776110030088](https://doi.org/10.1134/S1063776110030088).
- [75] Y. V. Petrov, N. A. Inogamov, and K. P. Migdal, “Thermal conductivity and the electron-ion heat transfer coefficient in condensed media with a strongly excited electron subsystem,” *JETP Letters*, vol. 97, no. 1, pp. 20–27, Mar. 2013, ISSN: 0021-3640, 1090-6487. DOI: [10.1134/S0021364013010098](https://doi.org/10.1134/S0021364013010098).

- [76] G. Kresse and J. Furthmüller, “Efficiency of ab-initio total energy calculations for metals and semiconductors using a plane-wave basis set,” *Computational Materials Science*, vol. 6, no. 1, pp. 15–50, 1996, ISSN: 0927-0256. DOI: [https://doi.org/10.1016/0927-0256\(96\)00008-0](https://doi.org/10.1016/0927-0256(96)00008-0). [Online]. Available: <https://www.sciencedirect.com/science/article/pii/0927025696000080>.
- [77] A. M. Komashko, *Laser-material interaction of powerful ultrashort laser pulses*. 2003.
- [78] S. L. Daraszewicz, Y. Giret, N. Naruse, Y. Murooka, J. Yang, D. M. Duffy, A. L. Shluger, and K. Tanimura, “Structural dynamics of laser-irradiated gold nanofilms,” *Phys. Rev. B*, vol. 88, p. 184 101, 18 Nov. 2013. DOI: [10.1103/PhysRevB.88.184101](https://doi.org/10.1103/PhysRevB.88.184101). [Online]. Available: <https://link.aps.org/doi/10.1103/PhysRevB.88.184101>.
- [79] V. V. Stegailov and P. A. Zhilyaev, “Warm dense gold: Effective ion–ion interaction and ionisation,” *Molecular Physics*, vol. 114, no. 3-4, pp. 509–518, 2015. DOI: [10.1080/00268976.2015.1105390](https://doi.org/10.1080/00268976.2015.1105390). [Online]. Available: <https://doi.org/10.1080/00268976.2015.1105390>.
- [80] G. P. Pun. (2017). “Purja pun’s interatomic potential,” [Online]. Available: <https://www.ctcms.nist.gov/potentials/entry/2017--Purja-Pun-G-P--Au/>.
- [81] L. V. Zhigilei, D. S. Ivanov, E. Leveugle, B. Sadigh, and E. M. Bringa, “Computer modeling of laser melting and spallation of metal targets,” in *High-Power Laser Ablation V*, C. R. Phipps, Ed., International Society for Optics and Photonics, vol. 5448, SPIE, 2004, pp. 505–519. DOI: [10.1117/12.548821](https://doi.org/10.1117/12.548821). [Online]. Available: <https://doi.org/10.1117/12.548821>.
- [82] G. Norman, S. Starikov, V. Stegailov, V. Fortov, I. Skobelev, T. Pikuz, A. Faenov, S. Tamotsu, Y. Kato, M. Ishino, M. Tanaka, N. Hasegawa, M. Nishikino, T. Ohba, T. Kaihori, Y. Ochi, T. Imazono, Y. Fukuda, M. Kando, and T. Kawachi, “Nanomodification of gold surface by picosecond soft x-ray laser pulse,” *Journal of Applied Physics*, vol. 112, no. 1, p. 013 104, 2012. DOI: [10.1063/1.4731752](https://doi.org/10.1063/1.4731752). eprint: <https://doi.org/10.1063/1.4731752>. [Online]. Available: <https://doi.org/10.1063/1.4731752>.
- [83] B. Chimier, V. T. Tikhonchuk, and L. Hallo, “Heating model for metals irradiated by a subpicosecond laser pulse,” *Phys. Rev. B*, vol. 75, p. 195 124, 19 May 2007. DOI: [10.1103/PhysRevB.75.195124](https://doi.org/10.1103/PhysRevB.75.195124). [Online]. Available: <https://link.aps.org/doi/10.1103/PhysRevB.75.195124>.
- [84] C.-Y. Shih, C. Wu, M. V. Shugaev, and L. V. Zhigilei, “Atomistic modeling of nanoparticle generation in short pulse laser ablation of thin metal films in water,” *Journal of Colloid and Interface Science*, vol. 489, pp. 3–17, 2017, Laser Synthesis, ISSN: 0021-9797. DOI: <https://doi.org/10.1016/j.jcis.2016.10.029>. [Online]. Available: <https://www.sciencedirect.com/science/article/pii/S0021979716307846>.

- [85] J. Q. Broughton, F. F. Abraham, N. Bernstein, and E. Kaxiras, “Concurrent coupling of length scales: Methodology and application,” *Phys. Rev. B*, vol. 60, pp. 2391–2403, 4 Jul. 1999. DOI: [10.1103/PhysRevB.60.2391](https://doi.org/10.1103/PhysRevB.60.2391). [Online]. Available: <https://link.aps.org/doi/10.1103/PhysRevB.60.2391>.

A. PHYSICS

A.1 Theory of electromagnetic wave-material interaction

In our study, we considered the normally incident laser as a plane-polarized electromagnetic wave and our materials as non-magnetic medium. For simplicity, we considered the laser travels in x direction ($\vec{n} = (1, 0, 0)$), $\vec{E} = (0, E(x), 0)$, $\vec{B} = (0, 0, B(x))$, and the target surface is at $x = 0$. For plane waves, we also have

$$\frac{\partial E}{\partial t} = -i\omega E \quad (\text{A.1})$$

To study of this electromagnetic wave propagation, we first start with Maxwell's equations, given by

$$\begin{aligned} \nabla \vec{E} &= \frac{\rho}{\epsilon_1 \epsilon_0} \\ \nabla \vec{B} &= 0 \\ \nabla \times \vec{E} &= -\frac{\partial \vec{B}}{\partial t} \\ \nabla \times \vec{B} &= \mu_1 \mu_0 \sigma \vec{E} + \mu_1 \mu_0 \epsilon_1 \epsilon_0 \frac{\partial \vec{E}}{\partial t} \end{aligned} \quad (\text{A.2})$$

where ρ is charge density, which is a constant for simplicity, ϵ_0 is vacuum permittivity, μ_0 is vacuum permeability, while ϵ_1 is the real part of the relative permittivity and μ_1 is the real part of the relative permeability.

Then to obtain the expression for the electric field, we used the following transformation given by

$$\nabla \times (\nabla \times \vec{E}) = \nabla(\nabla \cdot \vec{E}) - \nabla^2 \vec{E} \quad (\text{A.3})$$

where $\nabla \cdot \vec{E} = 0$ for plain waves.

We now have

$$\begin{aligned}
\nabla^2 \vec{E} &= -\nabla \times (\nabla \times \vec{E}) \\
&= -\nabla \times \left(-\frac{\partial \vec{B}}{\partial t}\right) \\
&= \frac{\partial}{\partial t}(\nabla \times \vec{B}) \\
&= \frac{\partial}{\partial t}(\mu_1 \mu_0 \sigma \vec{E} + \mu_1 \mu_0 \epsilon_1 \epsilon_0 \frac{\partial \vec{E}}{\partial t}) \\
&= \mu_1 \mu_0 \sigma (-i\omega \vec{E}) + \mu_1 \mu_0 \epsilon_1 \epsilon_0 (-\omega^2 \vec{E}) \\
&= -\mu_1 \mu_0 \left(i\frac{\sigma}{\omega} + \epsilon_1 \epsilon_0\right) \omega^2 \vec{E} \\
&= -\mu_1 \mu_0 (i\epsilon_2 \epsilon_0 + \epsilon_1 \epsilon_0) \omega^2 \vec{E} \\
&= -\mu_1 \mu_0 \epsilon_r \epsilon_0 \omega^2 \vec{E}
\end{aligned} \tag{A.4}$$

where we define $\sigma/\omega = \epsilon_2 \epsilon_0$ and the relative permittivity $\epsilon_r = \epsilon_1 + i\epsilon_2$. $\mu_1 = 1$ for most metals and $\mu_0 \epsilon_0 = 1/c_0^2$ where c_0 is the speed of light in vacuum. Therefore, the solution to E in equation A.4 is given by

$$E = E_0 e^{i(n_1 + in_2)\omega x/c_0} = E_0 e^{in_1 \omega x/c_0} e^{-n_2 \omega x/c_0} \tag{A.5}$$

where E_0 is the electric field at the surface and $\sqrt{\epsilon_r} = n_1 + in_2$.

According to equation A.5, the electric field attenuation length l_s is $c_0/(n_2 \omega) = \lambda/(2\pi n_2)$. Knowing that the laser intensity is proportional to the second power of the electric field, the intensity attenuation length (penetration depth) l_p is half of the electric field attenuation length l_s , given by

$$l_p = \frac{l_s}{2} = \frac{\lambda}{4\pi n_2} \tag{A.6}$$

As for the calculation of surface reflection, we need to consider the boundary condition at the surface. Normally, at an interface, we will have

$$\vec{n} \times (\vec{E}_1 - \vec{E}_2) = 0 \quad (\text{A.7})$$

$$\vec{n} \cdot (\vec{D}_1 - \vec{D}_2) = \rho_s$$

$$\vec{n} \times (\vec{H}_1 - \vec{H}_2) = \vec{J}_s$$

$$\vec{n} \cdot (\vec{B}_1 - \vec{B}_2) = 0$$

For normal incidents, equation A.7 can be simplified as

$$E_i + E_r = E_t \quad (\text{A.8})$$

$$B_i + B_r = B_t$$

where the subscripts i , r , and t represent incident, reflection, and transmission. The incident laser propagation direction $\vec{n} = (1, 0, 0)$, so is the transmitted wave, while the reflected direction $\vec{n}_r = (-1, 0, 0)$. For plane waves, the relationship between the electric field and the magnetic field is given by $\vec{B} = \sqrt{\mu\epsilon}\vec{n} \times \vec{E}$, which can transform $B_i + B_r = B_t$ into $E_i - E_r = \sqrt{\epsilon_r}E_t$. Therefore, the Fresnel formula of reflectivity for normally incident light is

$$R = \left\| \frac{E_r}{E_i} \right\|^2 = \left\| \frac{1 - \sqrt{\epsilon_r}}{1 + \sqrt{\epsilon_r}} \right\|^2 = \left\| \frac{1 - n_1 - in_2}{1 + n_1 + in_2} \right\|^2 \quad (\text{A.9})$$

where $\sqrt{\epsilon_r} = n_1 + in_2$.

A.2 Drude Model for relative permittivity

In order to calculate the penetration depth and reflectivity at the surface, we need to know the value of the relative permittivity ϵ_r . In an electric field, the force on electrons has two parts. One is the electric force and the other is a friction force due to collision, showing as

$$m_e \frac{d\vec{v}}{dt} = e\vec{E} - \nu_{eff}\vec{v} \quad (\text{A.10})$$

As mentioned above for plane waves, the time dependent term of the electric field is the oscillation term $e^{-i\omega t}$, the velocity will also inherit the same term and $d\vec{v}/dt = -i\omega\vec{v}$. Therefore, the solution to equation A.10 is given by

$$\vec{v} = \frac{e\vec{E}}{m_e(\nu_{eff} - i\omega)} \quad (\text{A.11})$$

Using the definition of current density ($\mathbf{j} = en_e\mathbf{v}$) and Ohm's law ($\mathbf{j} = \sigma\mathbf{E}$), the conductivity σ of the material can be obtained as

$$\sigma = \frac{en_e v}{E} = \frac{e^2 n_e}{m_e(\nu_{eff} - i\omega)} \quad (\text{A.12})$$

and the imaginary part of the relative permittivity ϵ_2 is

$$\epsilon_2 = \frac{\sigma}{\omega\epsilon_0} = \frac{e^2 n_e}{m_e(\nu_{eff} - i\omega)\omega\epsilon_0} \quad (\text{A.13})$$

Therefore, the relative permittivity is

$$\epsilon_r = \epsilon_1 + i\epsilon_2 = \epsilon_1 + i \frac{e^2 n_e}{m_e(\nu_{eff} - i\omega)\omega\epsilon_0} \quad (\text{A.14})$$

or

$$\epsilon_r = \epsilon_1 - \frac{\omega_p^2}{\nu_{eff}^2 + \omega^2} + i \frac{\omega_p^2 \nu_{eff}}{\omega(\nu_{eff}^2 + \omega^2)} \quad (\text{A.15})$$

where the plasma frequency $\omega_p = \sqrt{n_e e^2 / (\epsilon_0 m_e)}$ and laser angular frequency $\omega = 2\pi c_0 / \lambda$. In our studies, we assumed $\epsilon_1 = 1$ for metals.

B. CODES

All the codes mentioned below can be found at <https://github.com/DestinyOne/Femto-Research>.

B.1 Femto3D LAMMPS function

This is the modified LAMMPS function based on its two-temperature function. The corresponding files include 'fix_femto3D.cpp' and 'fix_femto3D.h' in the '[Femto3D](#)' folder.

B.2 Preheating LAMMPS codes

These files are in the '[Preheating](#)' folder. A target generated in MD is preheated to a wanted temperature and then relaxes to equilibrium. The output file for further use is a LAMMPS restart file for further simulation.

B.3 Running LAMMPS codes

These files are in the '[Common Runs](#)' folder. The LAMMPS input file requires a restart file which would be generated from the Preheating LAMMPS codes.

B.4 Analysis codes

These files are in the '[Analysis](#)' folder. The 'read.cpp' and 'read2.cpp' are to process the dump files from LAMMPS outputs and they should run in order. The rest MATLAB files are to generate figures using the temperature files from LAMMPS and the output files from 'read.cpp' and 'read2.cpp'.

VITA

Education

- **Purdue University** West Lafayette, IN
PhD in Nuclear Engineering, MS in Computer Engineering 2015 – 2021
- **University of Science and Technology in China** Anhui, China
BS in Nuclear Engineering 2011 – 2015

Research Experience

- **Graduate Research Assistant** 2015 – 2021
Purdue University West Lafayette, IN
 - Calculated Lithium energy level and photon emission and absorption coefficient using HULLAC code in EUV study
 - Modified and extended LAMMPS code to receive temperature dependent hydrodynamic parameters, add non-reflecting boundary, account for nonequilibrium electron effects for simulations on femtosecond laser and metal interactions
 - Found and summarized three unique ablation mechanisms for gold by a femtosecond laser pulse
 - Studied the effects of dual pulse irradiation, and found its improvement on nanoparticle production
- **Undergraduate Research Assistant** 2014 – 2015
University of Science and Technology in China China
 - Tested and found an improved production of hydrophobic catalyst by lyophilization
 - Improved on the sphericity of Li_3TiO_3 tritium breeder microspheres in dehydrating fabrication

Other Experience

- **61st annual meeting of the APS division of plasma physics** 2019
 - Gave an oral presentation on "Essential parameters in comprehensive hybrid modeling of metals irradiated by femtosecond laser"

- **IEEE Software Saturdays workshop at Purdue** 2018, 2019
 - Learned and practiced developing website and android app
- **Purdue University Chapter of Society for Applied Spectroscopy** 2017
 - Organized the 1st Purdue Symposium on Applied Spectroscopy and Photonics as vice president

Class Projects

- **Deep Reinforcement Learning Exploration** | *Python, Pytorch* 2020
 - Reproduced two state-of-the-art algorithms in deep reinforcement learning
 - Developed and tested a new algorithm by combining the two algorithms
- **Optimization Problems with Spherical Constraints** | *Julia* 2020
 - Explored various optimization methods to solve problems with spherical constraint
 - Summarized and compared the methods under different circumstances
 - Extended Augmented Lagrangian method with a reset feature and obtained higher accuracy
- **Fuzzy Tungsten Nanostructure Formation** | *Python, LAMMPS* 2018
 - Developed codes using Molecular Dynamics and Monte Carlo hybrid simulation
 - Reproduced the results in a paper

Honors and Awards

- **Ross Fellowship** 2015
- **Aegon-Industrial Global Responsibility Scholarship** 2014
- **Outstanding Undergraduate Scholarship (gold prize)** 2013

Publications

- **W. Yuan** and T. Sizyuk, 2021, “Ablation study in gold irradiated by single femtosecond laser pulse with electron temperature dependent interatomic potential and electron–phonon coupling factor”, *Laser Physics* **31** 036002

- T. Sizyuk, J. Oliver, and **W. Yuan**, 2018, “Effects of chamber conditions on EUV source efficiency and optical system performance during high-frequency operation”, *Extreme Ultraviolet (EUV) Lithography IX*, San Jose, United States, p. 63.

Technical Skills

- **Languages:** Python, C/C++, Julia, Fortran, MATLAB, SQL, JavaScript, HTML/CSS, Java
- **Scientific softwares:** LAMMPS, HULLAC, Gem5
- **Developer Tools:** Git, Google Cloud Platform, VS Code, Visual Studio
- **Libraries:** pandas, NumPy, Matplotlib, Pytorch, Keras, Scikit-Learn

Relevant Coursework

- **Graduate Level(Purdue):** Computational Physics (NUCL 597), Fuzzy Approach (NUCL 570), Computing for Engineering (CS 501), Optimization (AAE 550, CS 520), Parallel Computing (ECE 563), Computer Graphics (CS 535), Computer Architecture (ECE 565), Random Variables (ECE 600), Matrix Computations (CS 515), Deep Learning (ECE 595), Artificial Intelligence (ECE 570), Numerical Methods (ECE 608)

Publications

Journal Articles

- **W. Yuan**, T. Sizyuk, "Ablation study in gold irradiated by single femtosecond laser pulse with electron temperature dependent interatomic potential and electron-phonon coupling factor", *Laser Physics* **31**, 036002 (2021)

Conference Papers

- T. Sizyuk, J. Oliver, **W. Yuan**, "Effects of chamber conditions on EUV source efficiency and optical system performance during high-frequency operation", *Proc. SPIE 10583, Extreme Ultraviolet (EUV) Lithography IX*, 105831D (2018)

Conference Presentations

- **W. Yuan**, T. Sizyuk, "Essential parameters in comprehensive hybrid modeling of metals irradiated by femtosecond laser", *American Physical Society Division of Plasma Physics*, Fort Lauderdale, Florida (Oct 2019)